

110981  
1N-14

NASA Technical Memorandum 88844

# Optical Alignment of Centaur's Inertial Guidance System

(NASA-TM-88844) OPTICAL ALIGNMENT OF  
CENTAUR'S INERTIAL GUIDANCE SYSTEM (NASA)  
108 p CSCL 14B

N88-12515

Unclas  
G3/14 0110981

Andrew L. Gordan  
*Lewis Research Center*  
*Cleveland, Ohio*

December 1987

**NASA**

# OPTICAL ALIGNMENT OF CENTAUR'S INERTIAL GUIDANCE SYSTEM

Andrew L. Gordan  
National Aeronautics and Space Administration  
Lewis Research Center  
Cleveland, Ohio 44135

## SUMMARY

During Centaur launch operations the launch azimuth of the inertial platform's U-accelerometer input axis must be accurately established and maintained. This is accomplished by using an optically closed loop system with a long-range autotheodolite whose line of sight has been established by a first-order survey. A collimated light beam from the autotheodolite intercepts a reflecting Porro prism mounted on the platform azimuth gimbal. Thus, any deviation of the Porro prism from its predetermined heading is optically detected by the autotheodolite. The error signal produced is used to torque the azimuth gimbal back to its required launch azimuth. The heading of the U-accelerometer input axis is therefore maintained automatically.

Previously, the autotheodolite system could not distinguish between vehicle sway (translatory motion) and rotational motion of the inertial platform unless at least three prisms were used. One prism was mounted on the inertial platform to maintain azimuth alignment, and two prisms were mounted externally on the vehicle to track sway. For example, the automatic azimuth-laying theodolite (AALT-SV-M2) on the Saturn vehicle used three prisms.

This report documents and describes the results of testing and modifying the AALT-SV-M2 autotheodolite to simultaneously monitor and maintain alignment of the inertial platform and track the sway of the vehicle from a single Porro prism.

## INTRODUCTION

This report documents the results of testing and modifying the Perkin-Elmer automatic azimuth-laying theodolite (AALT-SV-M2) to verify the feasibility of operating this system from a single D-1A Centaur Porro prism at Complex 41, Eastern Test Range (ETR), Florida. The testing and modifications were performed at the Perkin-Elmer Corporation in Norwalk, Connecticut. The goal was to simultaneously monitor and align Centaur's inertial guidance platform from a single roof prism while tracking the sway of the vehicle (i.e., to distinguish the difference between translatory motion (sway) and rotational motion of the guidance platform). Previously three prisms were required - one mounted on the guidance platform and two located externally on the vehicle's skin to track sway. The results of these tests are discussed as well as the recommended modification to the equipment to meet the requirements of a single Porro prism monitoring system.

The autocollimator, the penta mirror assembly, the motor, and the sway servo chassis were installed on a base assembly located in a building at Complex 41, ETR. The site layout of this system is shown in figure 1. This

guidance optical alignment system (GOAS) was used during Centaur launch operations. Before launch, the U-accelerometer input axis of the Centaur platform Porro prism normal is offset nominally  $15^\circ$  in the azimuth plane from the U-accelerometer input axis, the autotheodolite's line-of-sight azimuth (established by a first-order survey) must be aligned as shown in figure 1. The autotheodolite is a closed-loop system which utilizes a collimated light to intercept the reflecting Porro prism mounted on the platform azimuth gimbal. Any deviation of the Porro prism from its predetermined heading is optically detected by the autotheodolite. The error signal produced is, in turn, used by the guidance system to torque the azimuth gimbal back to its required launch azimuth.

The original configuration, which was designed to monitor three prisms simultaneously and independently (carryover from the Saturn-Apollo Program), was tested initially and was found to be functioning properly in all channels. The autocollimator and chassis were then modified for single-prism operation in the error and acquisition channels. The results of these tests and modifications are discussed in the following pages. Appendix A is a symbols list included to aid the reader and appendixes B, C, and D contain data recorded by the author during the testing phase.

## TEST RESULTS

### Preamplifier Saturation

Operation of the autotheodolite system at line-of-sight distances closer than 425 ft caused preamplifier saturation because of excessive energy return from the uncoated Porro prism mounted on the guidance platform. Saturation, however, occurred only in the error preamplifier, which required at least a one-half reduction in energy before saturation was eliminated. The reduction was made by masking the prism to 1 by 0.375 in. When the source lamp voltage was lowered to eliminate saturation of the preamplifiers, the energy available for the sway and acquisition gain control (AQGC) channels was correspondingly reduced and the signal levels on these channels were insufficient for proper operation of the system. After reviewing this information, we decided to optically attenuate the energy falling on the error detector instead of reducing the gain of the error preamplifier. This was accomplished by inserting a dichroic filter (synchro error) between the sensing prism and the error detector as well as in front of the acquisition detector.

These tests were made using old detectors with reduced output; if new detectors were used, saturation might occur in other channels. Therefore, later in the program, checks were made for saturation using new sway and AQGC detectors. Although gain increased approximately threefold (appendix D, p. 79), saturation still did not occur in the sway and AQGC channel.

### Acquisition Detector

The acquisition detector used on the Centaur theodolites are single-area detectors located off axis so that at error prism null, where the error signal is zero, the acquisition detector provides an acquisition signal. Tests run

on an earlier program indicated that a split detector would give improved acquisition performance because the detector would be centered. This positioning would double the detector output since both phases of light would fall on it.

The nominal acquisition detector was replaced by an AQGC detector modified as shown in figure 2. In this way, the nominal AQGC detector and a modified AQGC detector could be tested simultaneously. The results of tests using the modified AQGC detector are indicated on figure 2.

### Theodolite Output Characteristics

For the operating range of 425 to 850 ft, the theodolite output signal characteristics for all channels have already been determined. In this study, signal characteristics at distances closer than 425 ft were measured to properly evaluate system operation at closer distances.

Since the sway and AGC channels were originally designed for use with a retroreflector, and the optical parameters of a Porro roof prism (as used on Centaur) are different from those of a retroreflector, the sway and AQGC error output characteristics were measured to determine whether the azimuth error components would interact with the sway and AQGC outputs. This interaction was evaluated during the test program, and further tests were performed to reduce or minimize this interaction.

The results of these tests are as follows:

Error channel - 250 ft (fig. 3)

Acquisition channel - 250 ft (fig. 4)

Sway channel - 250 ft (figs. 5 and 6)

[Note: Contrary to the configuration plan, it was not necessary to reverse detector bias to the sway detector because the sway detector uses a large-area single detector and the output signal is the algebraic difference signal.]

AQGC channel - 250 ft (figs. 7 and 8)

Error channel - 345 ft (figs. 9 and 10)

Acquisition channel - 345 ft (figs. 11 and 12)

[Note: Inasmuch as the acquisition detector must operate properly in both rotation and translation when operating from a single prism, data were recorded and plotted for both rotation and translation.]

Sway channel - 345 ft (figs. 13 and 14)

AQGC channel - 345 ft (figs. 15 and 16)

## Azimuth Compensation for Sway Channel at 345 ft

Analysis of the sway error output versus prism rotation (fig. 13) shows no similarity to the error channel output (fig. 10), thus eliminating the feasibility of azimuth error compensation. The data indicate, however, that the sway output was relatively insensitive to prism rotation for a short distance around null. The basic geometry of the sway detector - a large rectangular area on which a magnified image ( $2.5 \times$  prime focal plane) is formed - indicates that this relative insensitivity around null could be extended by increasing the size of the detector or, conversely, by reducing the image magnification without affecting the sway error translation characteristics. Reducing the magnification also reduces image motion across the detector, thus allowing a larger rotation to occur before the image begins to fall off of the detector. Tests were implemented by using another reimaging lens (magnification,  $\sim 2$ ) and relocating this lens to give a 1:1 image (fig. 17). In each configuration, sway translation outputs were also taken (fig. 18). These outputs, as predicted, were essentially identical. Figure 19 shows the sway outputs at various prism offsets at a 1:1 magnification.

## Azimuth Compensation for AQGC Channel at 345 Ft

The ideal AQGC channel output would remain constant over the entire theodolite acquisition range in both rotation and translation. Realistically, the AQGC output signal should remain essentially constant over the important operating range of at least  $\pm 15$  arc-sec of rotation and  $\pm 1$  in. of translation around null.

The AQGC detector is a large-area split detector. Each half of the detector is electrically biased in opposite polarity and at null each phase input signal falls on a separate half; thus, the AQGC signal is derived by summing the energy falling on the detector. When rotation occurs (inertial platform), the image moves across the detector and the output goes through zero to a maximum opposite phase before again going to zero (fig. 11).

The results show that the nominal AQGC detector is satisfactory in translation (fig. 16) but unsatisfactory in rotation (fig. 15). The modified AQGC detector improved rotation insensitivity around null (fig. 11). The results of the tests with the final configuration are shown in figures 20 to 23.

## Acquisition Channel

The acquisition channels of the theodolite were not controlled by the AQGC signal. Instead, the 5:1 change in gain level (nominally controlled in the other channels by the amplifier gain control (AMGC) was achieved by setting the acquisition amplifier level (fig. 24) high enough so that the acquisition relay  $K_1$  (fig. 24), would remain energized throughout a 5:1 signal attenuation. At this high gain level, however, the operational amplifier was overdriven and the phase was shifting. This problem was manifested by the acquisition light remaining on even when the opposite phase signal was used.

The same problem occurred during tests of the acquisition channel outputs using the split detector. With the acquisition amplifier gain level set so that, at null, the acquisition light would remain on at the low signal level (low end of the 5:1 range), a full signal (high end of the 5:1 range) caused saturation and phase shifting; thus, the positive phases at approximately  $\pm 75$  arc-sec looked negative. Consequently, the acquisition light remained on beyond the error range. This overdriving was eliminated by inserting two Zener limiting diodes across the  $R_5$  resistor (fig. 24) and by reducing resistor  $R_6$  to 3.9 k $\Omega$ .

Tests were run using the modified acquisition amplifier card. The aperture of the prism (Centaur) was masked down to 0.2 in. (one-half the full aperture), and the amplifier gain of the card was set so the acquisition light remained on. The full aperture was restored and the prism rotated throughout the acquisition output rotation range. The system performed as designed; that is, the acquisition light went out and stayed out beyond  $\pm 50$  arc-sec. During this test, the error channel was shorted so that only the acquisition signal was controlling the acquisition light.

#### Sway Servo Open-Loop Response

The penta open-loop response was measured by injecting electrical signals at the servo chassis. The output of the penta potentiometer was fed back to a frequency analyzer to represent the output of the system. The results are summarized in appendix D (pp. 87 and 88).

Two runs were taken because the data of the first run did not check with the computed values for system gain. The second run results were slightly higher, but not high enough to account for the difference. The two runs were averaged to compute system gain (appendix D, p. 86) and to plot the curve shown in figure 25.

The computed gain for the open-loop system is shown in appendix D (p. 86). The computed gain was compared with the experimental data. This gain, of course, includes the penta potentiometer scale factor which does not appear in the normal system loop gain. However, since the penta potentiometer scale factor was measured, the discrepancy was attributable to the amplifier-motor combination. The data indicate that the actual scale factor was 70 percent of the computed value. This factor of 0.7 was used in correcting the computed gains. Therefore, the previous amplifier-motor gain of 2.28 ( $18.5 \times 0.123$ ) was reduced to 1.60 ( $2.28 \times 0.70$ ).

The system open-loop equation (appendix D, eq. (D1)) was then revised to include the following changes:

- (1) A revised mechanical time constant of 0.083 sec (appendix D, p. 78)
- (2) A revised scale factor of 0.75 V/0.5 in. displacement instead of 0.50 V/0.5 in.
- (3) A revised amplifier-motor scale factor that was reduced by 70 percent
- (4) A noise suppression network (appendix D, p. 83)

As derived from appendix D (eq. (D2)),

$$\left. \begin{aligned} \frac{d^*}{x} &= 18 \frac{V}{ft} \frac{1}{(1 + 0.00934S)} \frac{1.6}{S(1 + 0.0835)} \frac{(1 + 0.0022S)}{(1 + 0.0050S)} \\ \frac{d^*}{x} &= \frac{29(1 + 0.022S)}{S(1 + 0.0835)(1 + 0.00934S)(1 + 0.0050S)} \end{aligned} \right\} \quad (1)$$

This is approximately twice the scale factor of the open-loop penta runs - a 6-dB increase. Therefore, raising the gain curve in figure 26 by 6 dB indicates that a gain margin of 9 dB will result in a phase margin of approximately 30°.

The computer printout of the system open-loop equation is given in figure 27. The computed phase margin is 10 dB and the gain margin is 24°, which is in fairly close agreement with the empirical data.

The mechanical time constant for the original system was 0.153 sec. Preliminary testing indicated that a large discrepancy existed. Experimental determination of the amplifier output impedance and motor armature resistance indicated this value should be revised to 0.083 sec. While it is difficult to establish the break frequency from figure 25, it appears to be in the 10- to 12- rad region, which is in good agreement with the computed value of 12.05 rad (0.083 sec) based on the new circuit impedances.

#### Sway Servo Closed-Loop Frequency Response

The penta closed-loop response for a 2.5-in. displacement is shown in figure 26. The frequency response test was extended to 2.6 Hz, but this did not extend far enough to indicate the magnitude of the resonance peak. Consequently, no experimental confirmation of the computed results was obtained in this case. However, the results do indicate that the penta system is capable of tracking small displacements beyond the required frequency of 0.75 Hz. Power saturation error for this low amplitude occurred between 1.6 and 1.8 Hz.

These tests were run with the fixed automatic gain control (AGC) to measure the servo performance independently of the AGC variable. The tests were run at three different scale factors - 0.50 V/0.50 in., 0.75 V/0.50 in., and 1.0 V/0.50 in. - as measured at the sway demodulator. Only the 0.75-V data were plotted since they represented a reasonable compromise in achieving the desired stability, 1-in. tracking accuracy, and sensitivity to shimmer. At a scale factor of 1 V/0.50 in., the system response was highly underdamped and very sensitive to shimmer. At 0.7 Hz the phase difference between the 1.0 V/0.5 in. and 0.75 V/0.50 in. volt scale factors was less than 2°.

The 12-in. displacement tests were run at these three scale factors with a fixed AGC at 0.70 Hz. The 0.5-V system lost lock but could track 0.6 Hz; the 0.75 V system could track 0.70 Hz but lost lock at 0.8 Hz; and the 1-V system could track 0.8 Hz but lost lock at 0.9 Hz. At these displacements the system approaches saturation, which occurs at about 0.8 Hz.

The 12-in. displacement tests were then conducted with the variable AGC implemented as in the normal mode of operation. With the 0.5-V scale factor, the system could track 0.7 Hz but lost lock at 0.8 Hz. The 0.75-V scale factor could track 0.8 Hz but lost lock at 0.85 Hz. No tests were made with the variable AGC of the 1.0-V scale factor. The following lags were recorded:

Scale Factor, V/1/2 in.	Fixed AGC		Variable AGC	
	Frequency, Hz	Displacement, in.	Frequency, Hz	Displacement, in.
0.5	0.6	1.33	0.75	1.38
.75	.75	.82	.6	.84
---	---	---	.8	1.0
1.00	.8	.92	.75	.65

As a check, the unmodified sway card was run but with a scale factor of 0.75 V/0.5 in. The system did track 12 in. peak to peak at 0.70 Hz but with a lag of 1.5 in. The unit was also checked at 0.8 Hz and 8.5 in. peak to peak. It lagged by 0.875 in. compared with a lag of 0.375 in. for the modified system. These tests were run with the variable AGC.

#### Sway Servo Transient Response

A step input to the penta was simulated by displacing the penta carriage various distances with the aperture blocked. The aperture was then unblocked while the penta position was recorded. This was done both manually and with an electromechanical shutter having a shutter speed of 5 msec to compare the difference in results, if any. The difference in overshoot was negligible. However, there were slight variations in the rise time because of experimental errors. We decided to manually control the aperture because overshoot was the most important factor and manual control was simpler.

The scale factor settings were measured at the sway demodulator and set at 0.75 V/0.5 in. Various displacements - 0.5, 1, 2, and 3 in. - were recorded. The data from these runs are summarized as follows:

Step displacement, in.	Overshoot, percent	
	Fixed AGC	Variable AGC
0.5	55	53
1	53	56
2	42	50
3	32	39

The data indicate that the AGC system maintained an increased system gain; that is, the system was not optically saturated (fig. 28). With the fixed AGC (i.e., no AGC effect), the system gain was set to 0.75 V/0.5 in. This gave a peak (optical limit) of 1.20 V, which occurred approximately 1.5 in. from null. A voltage level of 1.4 V drove the silicon-controlled rectifier (SCR) into its saturated condition. The variable AGC system would provide increased gain such that the 1.20-V level would be reached at a 0.75- to 0.85-in. displacement.

The AGC system now appears linear over a larger input displacement as noted in the previous table.

The computed system response based on the system equation (discussed on p. 71) predicts an overshoot of 50 percent. This is 4 percent lower than the measured overshoot, but within measurement and instrumentation tolerances.

#### Azimuth and Sway Errors

10 arc-sec wedge. - A rotating  $\pm 10$  arc-sec wedge was used to provide a continually varying azimuth error in the sway channel. The sway input was an 8.5-in. peak-to-peak displacement. The wedge frequency was varied from 0.1 to 2.0 Hz, and the sway frequency was varied from 0.2 to 1.0 Hz.

The lag at 1.0 Hz and at an 8.5-in. peak-to-peak displacement was 1.1 in. The  $\pm 10$  arc-sec wedge initially caused the system to lose lock, but a subsequent investigation indicated that the sway detector had moved as a result of the temporary support structure motion. After alignment, the system did not lose lock. This was checked by statically displacing the system 1.0 in. to the left and 1.0 in. to the right after realignment. The effect of the 10 arc-sec wedge on the system was extremely small. The recorder gain had to be increased 20 times before the azimuth effect was observed.

The system performance with the variable AGC was the same as that with the fixed AGC. This correlates with the graphical data since, with a 1-in. lag at 1.0 Hz, a 10 arc-sec rotation causes the AGC to decrease by approximately 10 percent (fig. 28). This small change permits the sway channel to be operated at reduced lag, thereby decreasing the azimuth effect. Experimentally, no significant difference between the fixed and variable AGC was observed.

180 arc-sec wedge. - The original intent in using the 180 arc-sec wedge was to simulate the acquisition mode of the theodolite. However, the simulation did not include the important cross-coupling effect of azimuth and sway. To include cross coupling, one would have to simulate the control loop of the guidance platform.

The wedge rotates at a constant speed producing a sinusoidal azimuth error. This introduces a further departure from a linear azimuth error rotation. However, if a slew rate of 36 arc-sec per sec is assumed, a 180 arc-sec wedge must complete a half revolution in 5 sec:

$$\frac{180}{36} = 5 \text{ sec} \quad (2)$$

This is only a half revolution since the scan goes from 180 to 0 to -180. The total wedge rotation time is therefore 10 sec at 0.1 Hz.

This rate was used for simulating the slew mode. In addition, the motor drive was automatically disconnected when the wedge reached the null position as determined by the wedge potentiometer. This cutoff action was independent of the theodolite output and thus did not exhibit any cross coupling.

The sway servo was never able to acquire system at the first signal appearance in the sway channel. It invariably passed through the active region three to four times before it acquired the Porro prism and nulled itself, but by this time the wedge rotation had stopped and the azimuth error was zero. The system was, however, able to acquire the Porro prism after the azimuth cycle; that is, during the combined sway-azimuth cycle it would always reacquire the Porro prism.

System simulation tests. - Tests were run using the 180 arc-sec wedge to simulate as closely as possible closed-loop sway operation. The first test was run with both sway systems disabled and with the wedge continuously rotating, displacing the penta mirror. The next test was run with the penta mirror sway servo operating and the wedge cycling and then stopping at the error null. The final series of tests were made with the sway simulator operating at an 8.5-in. peak-to-peak displacement and a 0.8-Hz frequency, the penta mirror servo operating, and the wedge rotating through one cycle to null. Data indicated that the penta mirror finally locks on after three cycles of the simulator.

Shimmer effects. - Two data runs were taken to indicate the effect of shimmer on a fairly typical bad day: that is, a bright, sunny day. One run was taken to indicate the effect of changes in gain (gains of 0.5 V/0.5 in. and 0.75 V/0.5 in.). Data indicated that the higher gain contained higher frequency components and larger peak displacements of up to 0.25 in. Data from a second run indicated that compensation networks reduce the bandwidth of the servo system (which is set by the network), not the mechanical system.

### System Limitation

Saturation. - The original sway servo system was able to track a 12-in. peak-to-peak displacement at 0.75 Hz with less than a 1-in. lag. However, the system was not able to track beyond 0.85 Hz without losing lock.

For smaller displacements (2.5 in.) the sway servo was able to track the target beyond 4.0 Hz. This indicated that the original system was power limited when tracking a 12-in. displacement at frequencies beyond 0.7 Hz. The simulator servo consisted of a similar SCR drive and motor but used a higher voltage power transformer for the SCR's. The simulator was tested up to 1.4 Hz at a 12-in. peak-to-peak displacement. It is probably capable of a higher power output, but it is limited by the voltage drop due to the long power line from the voltage source. The voltage at the simulator dropped by 20 V under the full load conditions of a 12-in. displacement and a 1.0- to 1.4-Hz frequency.

Thermal limitations. - The thermal limitation was set by the SCR power transformer, which has a 300-V-A rating. During tests of the sway servo, the transformer underwent a higher temperature rise than the motor. The simulator servo, however, had a 500-V-A transformer which replaced the 300-V-A transformer. The motor and transformer in the simulator had approximately equivalent temperature rises. In addition, the motor was not capable of dissipating the heat generated under a 12-in., 0.75-Hz condition for an extended period. Pages 73 to 75 of appendix D contain a discussion of these limitations.

The present motor and 500-V-A transformer under full-load conditions and without forced cooling should not be operated for a period exceeding 10 min. This has not been checked empirically, but is based on data obtained from the vendor for a similar motor.

## DESIGN MODIFICATIONS

The results of the study and test programs proved the feasibility of modifying the AALT-SV-M2 long-range theodolite to operate from a single D-1 Centaur Porro roof prism at a line-of-sight distance of 345 ft in accordance with Centaur operating parameters. The recommended modifications to the equipment were based on the evaluation of the test results.

### Channel Separation

The theodolite was originally designed to monitor three prisms located on the launch vehicle. The available energy spectrum was divided into four separate channels - one in the visible and three in the infrared region (shown crosshatched in fig. 29). In the early stages of the Centaur study, we felt that dividing the available energy into three instead of four channels would be the most practical way of correcting this imbalance: visible, error and acquisition, and sway and AQGC. However, further testing and evaluation indicated that it would be most advantageous to retain the original four channels and reassign these channels as follows: visible, error and acquisition, AQGC, and sway. This is the configuration presently being used for Centaur (fig. 29).

During the design phase of this theodolite, the spectral radiant flux density available in the sway and AQGC channels was found to be low compared to the two error channels (fig. 30). This imbalance was corrected by designing the retroreflector prism with an area three times that of the Porro prism. Since the Centaur configuration was designed to operate from a single, uncoated prism, the imbalance in the sway channel could not be corrected in the same way; therefore, an alternate method of increasing the available energy had to be devised.

One method of increasing the available energy on the sway and AQGC detectors requires moving the AQGC detector to the inertial prism acquisition location and removing the beamsplitter from in front of the sway detector (fig. 31). As shown, there is a 50-percent energy increase on the sway detector (4 to 6 percent) and approximately a 300-percent increase on the AGC detector (2 to 6.5 percent). This is the present configuration being used for Centaur.

To further correct the sway channel imbalance (fig. 31), the original uncoated beamsplitter was replaced with a 30:70 dichroic beamsplitter with the approximate percentage of energy available at each of the detectors shown in figure 31.

## Autocollimator

The modifications to the autocollimator were located mainly in the source and detector assembly. These changes were the results of rearranging the spectral separation scheme as shown in figure 29. Transmission plots of the various filters and beamsplitter are shown in figures 32 to 37. A simplified optical schematic of the source and detector assembly is shown in figure 39. Other modifications were as follows:

(1) The sway detector remained unchanged with the exception of adding a  $\times 1$  reimaging lens.

(2) The AQGC detector configuration was changed by increasing the central dead zone from 0.1 to 1.27 mm.

(3) The uncoated beamsplitter was replaced with a 30:70 dichroic beamsplitter as noted previously.

(4) The acquisition detector was redesigned as a split detector that was identical to the AQGC detector.

(5) The AGC detector was relocated (fig. 39) to retain the original  $\times 2.5$  magnification configuration.

(6) The electronic components were reworked; that is, those components that were no longer needed were removed.

(7) An external turn mirror reset was incorporated. The original design was such that, when switching back to the primary lamp from the redundant lamp, the outer cover and then a small cover on the source and the detector cover had to be removed to allow a screwdriver to be inserted into the turn mirror shaft to rotate this shaft. This method was not only time consuming but made it possible for the screwdriver to slip and damage the mirror coating.

(8) Lamp voltage was reduced to 4.7 V, thus allowing the lamp to operate at 2400-K color temperature and extending its life (9000 hr of life compared to the original 6.7 V which gave 120 hr of life).

## Display Panel

The changes to the display panel were as follows:

(1) The sway signal input to the sway logic control unit was disconnected, thus changing the sway acquisition function to AQGC acquisition.

(2) The DC amplifier was modified to increase the system scale factor from 100 to 200 mV/arc-sec, thus reducing the output signal impedance.

(3) The acquisition amplifier was modified in accordance with figure 24. The diodes were needed to prevent the operational amplifier from being overdriven.

(4) The acquisition relay driver was modified as in figure 24. Since the system operating scale factor was changed (item (2)), the error signal input to this card also increased. This error signal is used to actuate the acquisition relay and turn on the acquisition light.

#### Sway Servo Assembly

The changes to the sway servo assembly were as follows:

(1) The sway servo drive card was modified so the system could track prism sway of 12-in. peak-to-peak displacement at 0.75 Hz.

(2) The 300-V-A transformer was replaced with a higher wattage (500 V-A) unit.

(3) The sway servo covers were modified to incorporate a fan and ducts for cooling the transformer and motor.

An electronic block diagram of the Centaur system is shown in figure 40.

#### CONCLUDING REMARKS

The AALT-M2 long-range theodolite was designed and built by Perkin-Elmer Corporation to simultaneously but separately monitor the alignment of an inertial platform prism and track the sway prisms located on the skin of the launch vehicles at line-of-sight distances up to 850 ft.

One of these units (GFE) was tested at Perkin-Elmer to determine the feasibility of modifying the system to enable it to operate from a single D-1 Centaur roof prism at a shorter line-of-sight range of 325 ft. The tests performed and the results documented in the report show that the system can be modified, as specifically described in this report, and meet the Centaur system requirements.

For reuse on Complex 41 (Titan/Centaur DOD usage), the autotheodolite will require modification and prism adjustments because of the short line of sight available (~325 ft) and will require a new elevation height for the theodolite. Shimmer and amplifier saturation will in all probability be the major problem area because of the short line of sight.

Also, in the event that to DOD decides to eliminate the need for the autotheodolite at Complex 41 and to utilize gyrocompassing (as that proposed for Shuttle/Centaur) for azimuth alignment of Centaur's inertial platform, a word of caution is in order. With gyrocompassing, azimuth alignment errors are on the order of arc-minutes, whereas with the autotheodolite system, azimuth errors are on the order of arc-seconds. Depending on the mission accuracy requirement, gyrocompassing error sensitivity will affect the injection accuracy of the mission.

APPENDIX A  
SYMBOLS

A	area
$A(\lambda)$	atmospheric transmission with respect to wavelength
$A_{er}$	projected area of source for error channel
$A_i$	projected area of source at $i^{\text{th}}$ detector plane
$A_{pr,i}$	area of $i^{\text{th}}$ prism
$A_s$	area of sway detector
$A_{\text{sway, AQGC}}$	projected area of source for sway and acquisition gain control (AQGC) channels
$\underline{A}$	autocollimator matrix
$A^*$	attenuation ratio
$\underline{A}'$	return image matrix
a, b, c	direction cosines of unit directed outward from reflecting surface
c	capacitor
$B^*$	Boltzmann's constant
D	density of water vapor
$D^*$	detectivity
$D_{\text{norm}}^*(\lambda)$	normalized detectivity of detectors with respect to wavelength
$d_A$	autocollimator aperture
$d_{\text{lens}}$	autocollimator objective lens diameter
$d_o$	operating distance
$d_{\text{pen}}$	penta position
$d^*$	feedback at penta mirror position
E	voltage drop
$E_{\text{AMGC}}$	amplifier gain control (AMGC) control voltage
$E_a$	voltage applied to motor armature
$E_B$	bias voltage applied across cell and load resistor

$E^*$	elevation angle
$E'(\lambda)$	tungsten emissivity with respect to wavelength
$e_{in}$	input signal
$e_{out}$	dc output signal
$e_{sig}$	voltage of signal
$e_t$	output of theodolite
$e_l$	signal output voltage in rms
$F_B$	viscous friction load
$F_i^*(\lambda)$	dichroic filter transmission factors between source and $i$ th detector plane, with respect to wavelength
$F_T$	motor constant
$f$	theodolite focal length
$f/no$	$f$ -number of objective lens; focal length divided by average diameter
$f'$	frequency
$\Delta f'$	system electrical bandwidth
$G(S)$	motor and load transfer function
$\underline{G}$	geometric ray vector square matrix
$\underline{G}'$	reflected ray
$g$	gain
$H$	height
$H_{eff}^*(\lambda, T_0)$	effective spectral radiant flux density with respect to wavelength and color temperature
$H_i^*(\lambda)$	spectral radiant flux density with respect to wavelength
$h$	image height
$hum$	humidity
$I$	current
$I_{sig}$	maximum signal with an amplifier gain control voltage of 10 V
$I^*$	light intensity

$i_{dy}$	dynamic impedance
$J$	specific brightness of detector, $W/cm^2$
$J_T$	constant inertia of motor
$K$	constant
$K_B$	motor back electromotive force (EMF) constant
$K_g$	gain reduction factor
$K_r$	motor constant
$K_T$	torque constant
$K_v$	velocity gain
$L_i^*(\lambda)$	system component transmission factors between source and $i^{th}$ detector plane
$l, m, n,$	direction cosine of ray
$\underline{M}$	plane mirror square matrix
$n_{air}$	index of refraction of air
$n_{quartz}$	index of refraction of quartz
$P$	radiant power
$P_{AQGC}$	effective radiant power of acquisition gain control (AQGC) channel
$P_{dc}$	total dc radiant power at 0 in.
$P_i$	incident power at $i^{th}$ detector plane
$P_{sway}$	effective sway radiant power
$\underline{P}_Z$	matrix of penta mirror with its principle axis parallel to the Z-axis
$p$	pressure
$q$	electron charge
$R$	resistance, resistor
$RH$	relative humidity
$R_a$	resistance of armature circuit
$R_s$	series ohmic resistance

$R_{tot}$	total resistance of armature circuit
$R_x$	roof prism matrix with its roof
S	Laplace transform
SCR	silicon-controlled rectifier
S/N	signal-to-noise ratio
$S^*$	specific responsivity of detector
s	sway or displacement
$s_{ref}$	displacement or sway of 3 in.
sw	switch
$T_{ab}$	absolute temperature
$T_{am}$	ambient temperature
$T_0$	source color temperature
$T^*$	total transmittance
t	time
$t_D$	time domain
$\underline{U}$	desired orthogonal rotation matrix
V	voltage
v	precipitable water vapor
W	width
$W_{eff}^*(\lambda)$	effective spectral radiance of tungsten filament source
$W^*(\lambda, T_0)$	spectral radiance of source
$W_b^*(\lambda, T_0)$	black body brightness
w	width of image
$w_{aca}$	equivalent width of acquisition return image
$w_0$	limiting width
$w_{vig}$	width at which vignetting begins
X, Y, Z	coordinates

$x$	input error signal (displacement, in.)
$Y_{12A,12B,12C}$	short circuit transfer admittance of input networks A,B, and C
$y_n$	CCLS output on the $n^{\text{th}}$ cycle
ZOH	zero-order hold
$\alpha$	angle between direction of radiation and normal to surface
$\beta$	angular rotation of roof prism
$\epsilon$	log of constant
$\theta$	penta lead screw displacement, rad
$\theta_{\text{crit}}$	critical angle
$\theta_e$	azimuth misalignment reference error
$\theta_{\text{max}}$	maximum mirror angular travel that will return light to the autocollimator
$\theta_p$	guidance platform attitude, arc-sec
$\theta_p^{\circ}$	guidance platform drift, arc-sec/sec
$\theta_{\text{total}}$	angular acquisition range
$\theta_{\text{ref}}$	reference azimuth
$\lambda$	wavelength
$\lambda_{\text{cut}}$	long wavelength cutoff
$\xi$	damping ratio
$\rho$	angular position of Porro prism
$\sigma$	angle of rotation of the autocollimator return image about its center
$\sigma'$	return image rotation angle
$\tau$	response time constant
$\tau_{\text{elec}}$	motor electrical time constant
$\tau_{\text{mech}}$	mechanical time constant
$\tau^*$	thermal time constant
$\gamma$	demodular time constant

$\phi$	autocollimator azimuth reading
$\psi$	autocollimator elevator reading
$\Omega$	solid angle
$\Omega_i$	effective field angle of system for $i^{\text{th}}$ detector plane
$\omega$	frequency in radians
$\omega_B$	frequency response of motor

Subscripts:

A	autocollimator aperture
AGC	automatic gain control
AMGC	amplifier gain control
AQGC	acquisition gain control
A'	theodolite aperture
a	armature
ab	absolute
ac	alternating current
aca	acquisition return image
acq	acquisition channel
a-c	armature to case
am	ambient
amp	amplifier
avg	average
B	bias
b	black body
c	case
c-a	case to armature
D	diode
dc	direct current

dy	dynamic
e	response
eff	effective
elec	electrical
er	error channel
error	error
f	control
g	gain
I	current
i	$i^{\text{th}}$ prism; $i^{\text{th}}$ detector plane
in	input
L	load
ℓ	limiting
m	motor
max	maximum
mech	mechanical
n	$n^{\text{th}}$
nose	nose of prism
norm	normalized
o	operating
oc	open circuit
out	output
p	platform
pen	penta
pr	Porro prism
R	resistor
ref	reference

rfl	reflector
S	series
s	sway detector
sig	signal
sway	sway channel
sys	system
T	torque
t	theodolite
tot	total
tri	triangular prism
v	velocity
vig	vignetting
X,Y,Z	coordinates
0	source

In appendixes B, C, and D are the engineering data and notes taken from the author's notebook. This information was recorded by the author during the testing phase.

APPENDIX B  
LONG-RANGE, AUTOMATIC AZIMUTH-LAYING THEODOLITE

SYSTEM DESIGN STUDY AND CONSIDERATIONS - FIGURES OF MERIT (FOM)

The predicted performance of the automatic azimuth-laying theodolite (AALT) is determined by calculating the figures of merit (FOM's) listed for the various channels as

(1) Error Channels

- (a) Angular sensitivity, W/arc-sec
- (b) Signal-to-noise ratio (S/N) per arc-sec
- (c) Angular resolution (for unity S/N)

(2) Acquisition channels

- (a) Radiant flux at error channel null
- (b) S/N at error channel null

(3) Sway channel

- (a) Effective radiant flux at 1/16-in. sway
- (b) S/N for 1/16-in. sway
- (c) Sway resolution (for unity S/N), in.

(4) Automatic gain control (AGC) channel

- (a) Radiant flux

To calculate these quantities, one must evaluate the following equation:

$$P_i = \int_{\lambda_{\min}}^{\lambda_{\max}} A(\lambda) [L_i^*(\lambda)] F_i^*(\lambda) [W_{\text{eff}}^*(\lambda)] D_{\text{norm}}^*(\lambda) \int_{A_i} dA \int_{\Omega_i} d\Omega \quad (B1)$$

where

- $P_i$  incident power at  $i^{\text{th}}$  detector plane ( $i^{\text{th}}$  channel), W
- $A(\lambda)$  atmospheric transmission
- $L_i^*(\lambda)$  system component transmission factor (reflection losses, etc.) for  $i^{\text{th}}$  channel
- $F_i^*(\lambda)$  dichroic filter transmission factors between source and  $i^{\text{th}}$  detector plane

- $W_{\text{eff}}^*(\lambda)$  effective spectral radiance of tungsten filament source,  $W/cm^2-\mu m-sr$   
(watts/centimeters squared-micrometers-steradians)
- $D_{\text{norm}}^*(\lambda)$  normalized detectivity of detectors
- $A_i$  projected area of source at  $i^{\text{th}}$  detector plane
- $\Omega_i$  effective field angle of system for  $i^{\text{th}}$  detector plane

Since the AALT generates six outputs simultaneously, equation (B1) must be evaluated six times, with each calculation including the particular loss factors and dichroic filters for the channel being calculated. In addition, the results are nonlinear functions for four important operating parameters - source color temperature, operating distance, ambient temperature, and ambient humidity. Thus equation (B1) must be reevaluated in its entirety, six times, for any change in these parameters.

Because the calculation for each channel and choice of operating parameters involves the integration of the product of approximately eight wavelength terms, Perkin-Elmer designed a digital computer program to perform these lengthy computations.

#### EVALUATION OF EFFECTIVE RADIANT FLUX INCIDENT ON DETECTOR PLANES

The following discusses the nature of the terms used to evaluate the integral in equation (B1).

##### Atmospheric Transmission $[A(\lambda)]$

The transmission of the atmosphere, exhibits two absorption bands within the 0.7 to 2.6  $\mu m$  region - one at 1.3  $\mu m$  and one at 1.8  $\mu m$ . It is these two absorption bands, resulting from water vapor absorption, that are used to effect spectral separation of the three spectral regions of the AALT.

The amount of absorption present is determined by the amount of precipitable water vapor in the path, multiplied by two to account for the two-way transmission of the theodolite beam. The amount of precipitable water vapor can be found from the path length, the ambient temperature, and the ambient humidity, as follows: For the temperature range  $0^\circ < T_{\text{am}} < 30^\circ \text{C}$ , the density of the water vapor  $D$  can be closely approximated by

$$D(T_{\text{am}}) = 0.00034 \exp(0.00574T) \text{ lb/ft}^3$$

where

$T$  ambient temperature,  $^\circ \text{C}$

The precipitable water vapor,  $v$  (in centimeters), is found as

$$v(T_{\text{am}}, d_o, \text{hum}) = 2 \frac{D(T_{\text{am}})}{62.4} d_o \frac{\text{RH}}{100} \quad (\text{B2})$$

where

$d_0$  path length, cm

RH relative humidity, percent

For Florida use an RH of 90 percent, a  $T_{am}$  of 90 °F (32.2 °C), and  $d_0$ 's of 450 and 833 were elected.

### Dichroic Filter Transmission [ $F_i^*(\lambda)$ ]

To take advantage of the natural separation of the 0.7- to 2.6- $\mu$ m region into three separate regions because of water vapor absorption, various dichroic filters were designed to split the three regions apart by selective reflection of one or two regions and by transmission of the remaining regions. Thus, combinations of different filters permit the isolation, at the various detector planes, of a single spectral region.

### System Component Transmission [ $L_i^*(\lambda)$ ]

The system component transmission factor, evaluated for each channel, must take into account the following losses: (1) attenuation in glass elements, (2) losses at reflecting surfaces, (3) losses at air-glass surfaces, and (4) filament reimaging system losses

Glass transmittance. - The relative transmittance of various optical glasses is a function of wavelength. Of the glasses considered (BK-7, Homosil, Flint, Infrasil I, and soda lime), Infrasil I was selected for all transmitting elements of the system because of its superior long-wavelength-transmission characteristics. The following table gives the total glass thicknesses traversed by the energy contained in the various channels as well as other system component transmission factor parameters.

	Glass path length, in.		Number of air-glass surfaces	Number of gold reflections	Filament reimaging system transmittance			
	Soda lime	Infrasil I						
Synchro error	0.50	4.20	21	10	0.5			
Inertial error	↓	4.20		↓	↓	↓		
Synchro acquisition		3.95						
Inertial acquisition		3.95						
Sway		4.70					11	1.0
AGC		4.70					11	1.0

Reflecting Element Reflectance. - Availability of high-reflectivity metallic coatings is very limited; only three coatings - aluminum, gold, and silver - appeared to be feasible. Silver has the highest reflectivity over the

bandwidth used in the system, but it is very sensitive to sulfurization. Aluminum is very efficient and durable, but it is very inefficient at 0.825  $\mu\text{m}$ , especially for the number of reflections. Gold was chosen because of its high reflectivity in the infrared range and its resistance to oxidation.

Air-glass surface transmittance. - Because of the broad spectral band used (0.7 to 2.6  $\mu\text{m}$ ), antireflection coatings would not be effective in reducing the reflection losses at air-glass surfaces. For  $n$  surfaces, the total transmittance is given by  $T^* = (0.966)^n$ .

Filament reimaging system losses. - The theodolite image projected out to the target prism assembly is composed of two filament images formed by the system of condensing lenses and the transfer prism. The transfer prism splits the image of the filament into two equal images, which are in turn focused by the transfer mirrors onto the theodolite image plane. Thus two images of the single lamp filament are formed, with each image having half the width of the original filament.

These two filament images are alternately chopped with a mechanical chopper having a duty cycle of 50 percent. The two filaments are chopped 180° out of phase, causing the total energy transmitted to the target prism to be equal to the dc energy of one phase, or 50 percent of the energy radiated by the filament. The error and acquisition channel detectors are illuminated by the image of one phase only, and thus receive 50 percent of the total transmitted energy. The sway and AQGC channel detectors are illuminated by both phases and thus receive 100 percent of the transmitted energy.

Therefore, the filament reimaging system transmittances are 0.5 for the error and acquisition channels and 1.0 for sway and AQGC channels.

#### EFFECTIVE SPECTRAL RADIANCE OF TUNGSTEN SOURCE [ $W_{\text{eff}}^*(\lambda)$ ]

The effective spectral radiance flux density  $H^*(\lambda, T_0)$  (given in  $\text{W}/\text{cm}^2\text{-}\mu\text{m}$ ) of the tungsten ribbon filament source is given by Planck's law, modified by the emissivity of tungsten:

$$H^*(\lambda, T_0) = [E'(\lambda)] C_1 \lambda^{-5} [\exp(C_2/\lambda T) - 1]^{-1} \quad (\text{B3})$$

where

$\lambda$  wavelength, cm

$T_0$  source temperature, K

$E'(\lambda)$  tungsten emissivity

$C_1$   $3.74 \times 10^4$   $\text{W}/\text{cm}^2\text{-}\mu\text{m}$

$C_2$  1438  $\mu\text{m}\text{-deg}$

If  $W^*(\lambda, T_0)$  is the spectral radiance of the source, then using the  $\cos\alpha$  relationship for a Lambertian source,

$$H^*(\lambda, T_0) = \int_0^{2\pi} W^*(\lambda, T_0) \cos\alpha \, d\Omega \quad (B4)$$

where

$\alpha$  angle between direction of radiation and normal to surface

$\Omega$  solid angle

and integrating over a hemisphere, with

$$d\Omega = 2\pi \sin\alpha \, d\alpha \quad (B5)$$

yields

$$H^*(\lambda, T_0) = W^*(\lambda, T_0) \int_0^{2\pi} 2\pi \sin\alpha (\cos\alpha) \, d\alpha = \pi W^*(\lambda, T_0) \quad (B6)$$

Thus,

$$W^*(\lambda, T_0) = \left(\frac{1}{\pi}\right) H^*(\lambda, T_0) \quad (B7)$$

The emissivity of tungsten can be approximated for the range  $0.6 < \lambda < 2.6 \, \mu\text{m}$ ,

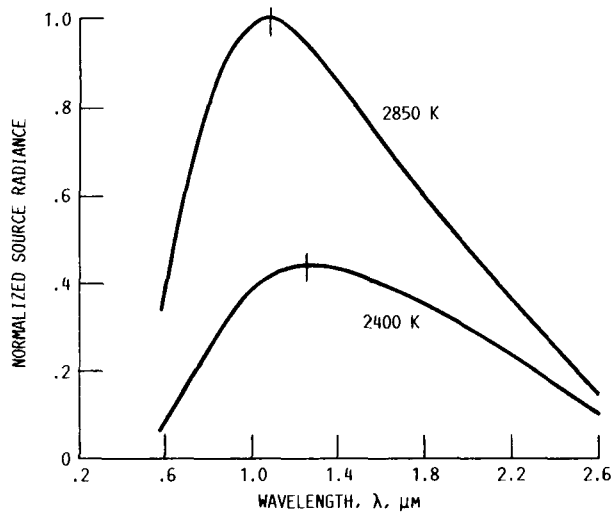
$$E'(\lambda) = 3.5 \times 10^{-1} \lambda^{-1/2} \quad (B8)$$

Thus, using equations (7) and (8),

$$W^*(\lambda, T_0) = 4.17 \times 10^3 \lambda^{-1/2} \left[ \exp(1.4384/\lambda T_0) \right]^{-1} \quad (B9)$$

#### NORMALIZED LEAD SULFIDE DETECTIVITY [ $D_{\text{norm}}^*(\lambda)$ ]

The normalized detectivity  $D_{\text{norm}}^*(\lambda)$  of the lead sulfide (PbS) detectors is for black body tungsten emissivity shown in the following sketch, which describes the relative sensitivity of the detectors as a function of wavelength (i.e., effective source radiance).



The effective radiant power measured by the detectors is given by

$$W_{\text{eff}}^*(\lambda, T_0) = D_{\text{norm}}^*(\lambda) [W^*(\lambda, T_0)] \quad (\text{B10})$$

A second figure of merit (FOM) of lead sulfide detectors, the average detectivity  $D_{\text{avg}}^*$ , is related to the normalized detectivity and will be covered later.

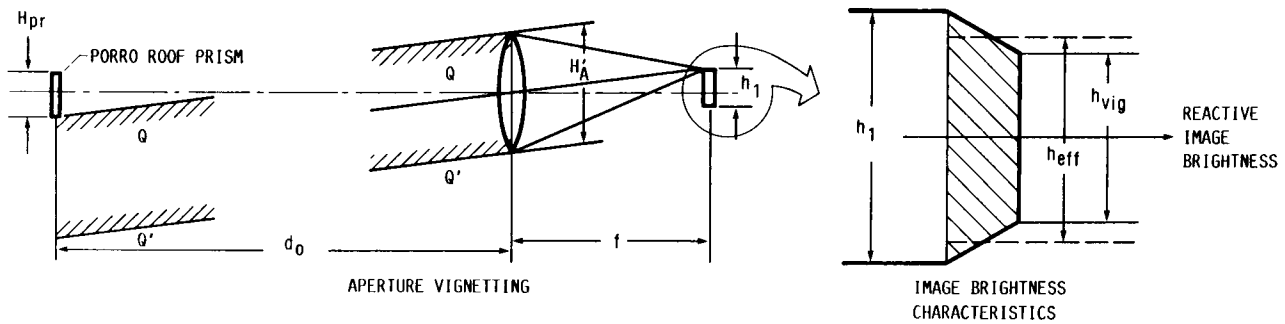
#### PROJECTED AREA OF SOURCE ( $A_j$ )

The projected area of the source for each channel is the effective area of the ribbon filament reimaged at the corresponding detector plane. This area is different for each of the following three cases, each of which will be considered separately: (1) error channels, (2) acquisition channels, (3) sway-AQGC channels.

#### Error channels

The height of the reimaged source for each channel is limited by vignetting at the target Porro prism.

From the following sketches, the beam marked QQ' represents a point in the source for which the brightness of the reimaged filament is zero.



Since the target Porro prism will return any beam having a deviation in elevation back along the direction of incidence, any point closer to the axis will be reimaged with a brightness greater than zero. This limiting image height  $h_{\ell}$  is thus found as

$$h_{\ell} = \frac{(H_{A'} + H_{pr})f}{d_o} \quad (B11)$$

where

$H_{A'}$  theodolite aperture height

$H_{pr}$  prism height

$f$  theodolite focal length

$d_o$  operating distance

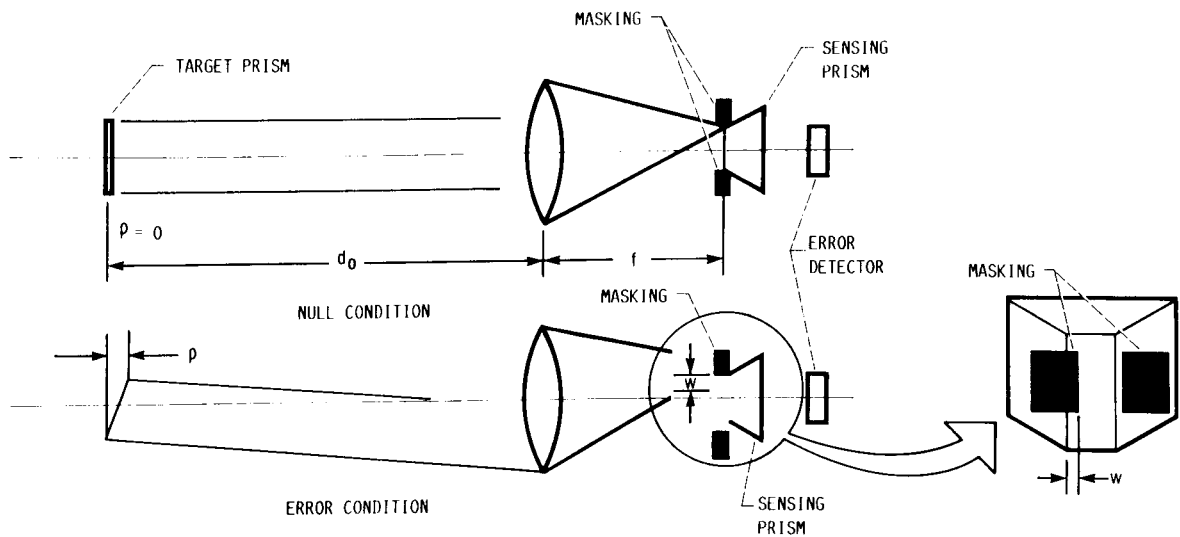
The height  $h_{vig}$  at which vignetting begins is given by

$$h_{vig} = \frac{(H_{A'} - H_{pr})f}{d_o} \quad (B12)$$

Thus, the effective height  $h_{eff}$  of the image shown above is equal to

$$h_{eff} = h_{vig} + \frac{1}{2}(h_{\ell} - h_{vig}) = \frac{fH_{A'}}{d_o} \quad (B13)$$

The width of the image projected onto the error detectors is not limited by aperture vignetting but is determined by the angular deviation  $\rho$  of the target Porro prism. At zero deviation, no energy reaches the error detectors through the sensing prism. (See the following sketch.)



When the target Porro prism is rotated through an angle  $\rho$  the image is rotated through an angle  $2\rho$ , causing a strip of the image of width  $w$  to fall on the clear nose of the sensing prism. Thus,

$$w = 2\rho f \quad (B14)$$

Combining this with  $h_{eff}$ , the projected area of the source for the error channels is

$$A_{er} = \frac{2f^2 H_A \rho}{d_o} \quad (B15)$$

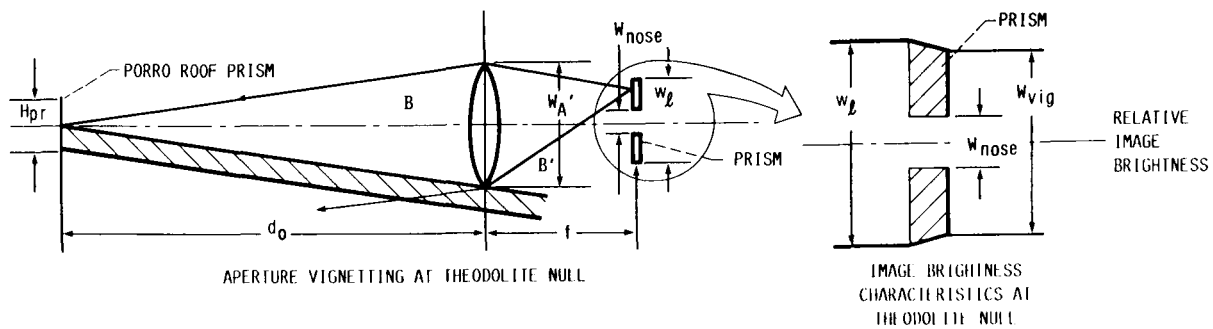
where

$\rho$  angular deviation of target Porro prism, rad

### Acquisition Channels

Since the same prisms are used for the error and acquisition channels, the effective height of the reimaged source for the acquisition channels is given by equation (B13).

However, the width,  $w$ , of the reimaged source is determined by vignetting at the theodolite aperture for the case shown in the following sketches.



From the sketch noted as "Image Brightness Characteristics at Theodolite Null" we obtain

$$w_l = \frac{W_{A'} f}{d_0} \quad (B16)$$

where

$W_{A'}$  theodolite aperture width

The width at which vignetting begins  $w_{vig}$  is approximately given by

$$w_{vig} = \frac{f(2W_{A'} - H_{pr})}{2d_0} \quad (B17)$$

The equivalent width  $w_{aca}$  of the acquisition return image is equal to

$$w_{aca} = w_{vig} + \frac{(w_l - w_{vig})}{2} - W_{nose} \quad (B18)$$

where

$W_{nose}$  width of clear nose of prism

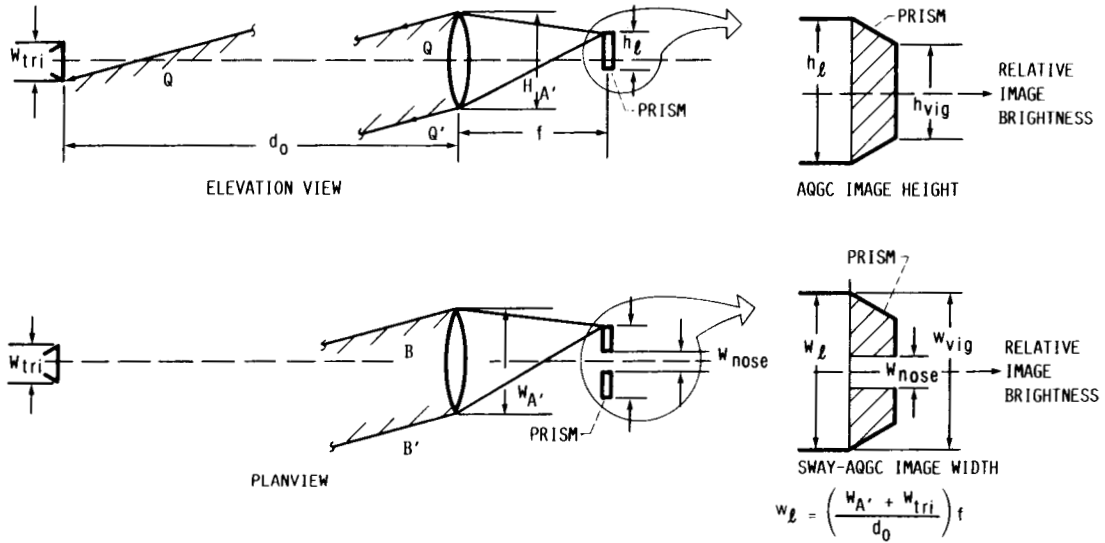
$$w_{aca} = \frac{f(4W_{A'} - H_{pr})}{4d_0} - W_{nose} \quad (B19)$$

Combining equation (B19) with equation (B13) yields the projected area of the source of the acquisition channels:

$$A_{acq} = \frac{H_{A'} f}{d_0} \left[ \frac{f(4W_{A'} - H_{pr})}{4d_0} - W_{nose} \right] \quad (B20)$$

## Sway-AQGC Channels

The effective height of the reimaged source for the sway-AQGC channel is governed by vignetting at the aperture of the target prism (retroreflector) since all energy intercepted by the prism will be reflected back along the direction of incidence into the theodolite aperture. From the geometry given in the following sketches,



the effective image height is

$$h_{\text{eff}} = \frac{f H_{A'}}{d_0} \quad (\text{B21})$$

and the effective image width  $w_{\text{eff}}$  is given by

$$w_{\text{eff}} = \left[ w_{\text{vig}} + \frac{1}{2}(w_l - w_{\text{vig}}) - w_{\text{nose}} \right] \quad (\text{22})$$

where

$$w_l = \frac{W_{A'} + w_{\text{tri}}}{d_0} \quad (\text{B23})$$

and

$$w_{\text{vig}} = \frac{W_{A'} - w_{\text{tri}}}{d_0} \quad (\text{B24})$$

Substituting  $w_l$  and  $w_{\text{vig}}$  into equation (B22) yields

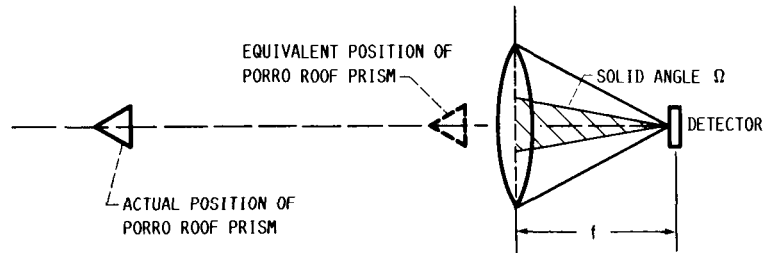
$$w_{\text{eff}} = \frac{f W_{A'}}{d_0} - w_{\text{nose}} \quad (\text{B25})$$

Thus the projected area of the source for the sway and AGC channels is

$$A_{\text{sway,AQGC}} = \left( \frac{fH_{A'}}{d_o} \right) \left( \frac{fW_{A'} - W_{\text{nose}}}{d_o} \right) \quad (\text{B26})$$

### Effective Field Angle for $i^{\text{th}}$ Detector

The solid field angle  $\Omega$  of the system for each channel is determined by the aperture areas of the corresponding target prism. As shown in the following sketch, the actual position of the target prism anywhere within the region of collimated beams is equivalent to a position at the theodolite aperture.



Thus, the solid angle presented to the source is given by

$$\Omega_1 = \frac{A_{\text{pr},i}}{f^2} \quad (\text{in steradians}) \quad (\text{B27})$$

where

$A_{\text{pr},i}$  prism area of  $i^{\text{th}}$  prism

### SPECTRAL RADIANT FLUX DENSITY AT DETECTOR PLANES

The measure of relative energy available to the channels of the theodolite is the spectral radiant flux density  $H_i^*(\lambda)$  (given in  $\text{W}/\text{cm}^2\text{-}\mu\text{m}$ ) at the various detector planes. This quantity is found by integrating the integrand of equation (B1) with respect to  $\Omega$  as follows:

$$H_i^*(\lambda) = \int A(\lambda) \left[ L_i^*(\lambda) \right] F_i^*(\lambda) \left[ W_{\text{eff}}^*(\lambda) \right] D_{\text{norm}}^*(\lambda) d\Omega \quad (\text{B28})$$

### Error Channel Performance

Three FOM's are applicable to the performance of the theodolite error channels: (1) angular sensitivity (given in  $\text{W}/\text{arc-sec}$ ), (2) signal-to-noise (S/N) ratio per arc-sec, and (3) angular resolution.

Angular sensitivity. - Angular sensitivity of each error channel is found by evaluating equation (B1), using the projected source data from equation (B15) corresponding to 1 arc-sec deviation of the target prism.

Signal-to-noise ratio per arc-sec. - Before finding the system S/N ratio per arc-sec of error for the error channels, the average detectivity  $D_{avg}^*$  of the PbS detectors must be used to obtain the detector S/N ratio.

Detectivity. - Average detectivity  $D_{avg}^*$  of PbS detectors is specified for a specific optical chopping frequency and a specific color temperature  $T_0$ , and has the units

$$S/N \left( \frac{cm\sqrt{Hz}}{W} \right) \quad (B29)$$

Using  $D_{avg}^*$ , the S/N ratio is found as

$$S/N = D_{avg}^* (A_s \Delta f')^{-1/2} (P) \quad (B30)$$

where

$A_s$  sway detector area,  $cm^2$

$\Delta f'$  system electrical bandwidth, Hz

$P$  radiant power, W

The detectivity  $D_{avg}^*$  is obtained by measuring the S/N ratio obtained with a blackbody source at a specified color temperature. Since the radiant energy actually detected by the detector is the integral of the brightness of the source weighted by the normalized detectivity  $D_{norm}^*(\lambda)$  (i/e.,  $W_{eff}^*(\lambda, T_0) = D_{norm}^*(\lambda) [W^*(\lambda, T_0)]$ ) the average detectivity  $D_{avg}^*$  is valid only when used with a source having the specified color temperature.

Using the normalized detectivity  $D_{norm}^*(\lambda)$ , one can obtain a quantity  $D_{max}^*$ , independent of color temperature, as

$$D_{avg}^*(T_0) \int_{\lambda_1}^{\lambda_2} W_b^*(\lambda, T_0) d\lambda = D_{max}^* \int_{\lambda_1}^{\lambda_2} W^*(\lambda, T_0) D_{norm}^*(\lambda) d\lambda \quad (B31)$$

where

$W_b^*(\lambda, T_0)$  black body brightness

$T_0$  source color temperature for  $D_{avg}^*(T_0)$

Once  $D_{\max}^*$  is found by evaluating the above equation for  $T_0$ , the S/N ratio for a source of any color temperature can be found by evaluating the right hand side of the above equation. The integral or the right hand side is, for the theodolite system, the integral in equation (B1), which represents the total effective radiant power incident on the detector. Thus, for any color temperature, equation (B30) becomes

$$S/N = \left[ \frac{D_{\max}^*}{(A_s \Delta f')^{1/2}} \right] \left[ \int_{\lambda_1}^{\lambda_2} W_b^*(\lambda, T_0) D_{\text{norm}}^*(\lambda) d\lambda \right] \quad (B32)$$

For the angular sensitivities calculated previously, predicted values of S/N for 1-arc-sec prism motion are shown in the following table along with other indicators of error channel performance.

	Distance, 833 ft; color temperature, 2850 K		Distance, 450 ft; color temperature, 2400 K	
	Synchro error	Inertial error	Synchro error	Inertial error
Wavelength, $\mu\text{m}$	0.7 to 1.3	0.33 to 1.8	1.3 to 1.8	0.7 to 1.3
Angular sensitivity, W/arc-sec	$1.54 \times 10^{-8}$	$6.49 \times 10^{-9}$	$1.25 \times 10^{-8}$	$6.63 \times 10^{-9}$
<sup>a</sup> Detector S/N ratio for 1 arc-sec	354	148	288	152
Angular resolution arc-sec	0.0028	0.0067	0.0035	0.0065

<sup>a</sup>Overall system S/N ratio could be approximately 3 dB less than values listed because of noise in the electronics.

Angular resolution. - The angular resolution of each error channel can be found by setting the detector S/N ratio to unity and solving for the angular error position of the target prisms. Then equation (B31) becomes

$$1 = \left[ \frac{D_{\max}^*}{(A_s \Delta f')^{1/2}} \right] P_{\text{er}} \quad (B33)$$

Acquisition Channel Performance. - There are two FOM's applicable to the performance of the theodolite acquisition channels: (1) radiant flux and (2) S/N ratio. For the acquisition channels, radiant flux is found by evaluating equation (B1) using equations (B20) and (B27). S/N ratios for the acquisition channels were found by evaluating equation (B32) using the radiant flux values in the following table. Predicted values for the radiant flux are also shown in the following table of performance for the acquisition, sway, and AQGC channels.

	Synchro acquisition	Inertial acquisition	Synchro acquisition	Inertial acquisition
Wavelength, $\lambda$ , $\mu\text{m}$ ,	0.7 to 1.3	0.33 to 1.8	0.7 to 1.3	1.3 to 1.8
Radiant flux, W	$8.41 \times 10^{-8}$	$3.53 \times 10^{-8}$	$1.42 \times 10^{-7}$	$7.54 \times 10^{-8}$
S/N ratio	$7.72 \times 10^3$	$3.24 \times 10^3$	$1.31 \times 10^4$	$6.92 \times 10^3$

	Sway	AQGC	Sway	AQGC
Wavelength, $\lambda$ , $\mu\text{m}$	1.8 to 2.6	1.8 to 2.6	1.8 to 2.6	1.8 to 2.6
Radiant flux, W	$9.46 \times 10^{-10}$	$6.16 \times 10^{-8}$	$2.41 \times 10^{-9}$	$1.56 \times 10^{-7}$
S/N ratio	43		110	
Operating distance, ft	833		450	
Color temperature, K	2850		2400	

<sup>a</sup>Sway radiant flux and S/N ratio were calculated for 1/16-in. sway.

### Sway Channel Performance

At the sway channel detector plane, both images of the filament (one for each phase) fall on a single detector. Sway results in a difference between the total incident power of each phase giving rise to a small ac signal whose magnitude is proportional to the magnitudes of the sway of the target prism, and whose phase indicates the direction of sway. Thus the desired sway signal is only a small fraction of the total incident power contained in the image for small sway displacements.

The desired ac component of the sway channel changes from 0 to 100 percent of the total radiant power as the target prism sways from 0 to 3 in. It is assumed that the magnitude of the ac component varies linearly with sway displacement. Thus for sway  $s$ , the effective sway radiant power  $P_{\text{sway}}$  is equal to

$$P_{\text{sway}} = \frac{s}{s_{\text{ref}}} (P_{\text{dc}}) \quad (\text{B34})$$

where

$s_{\text{ref}}$  3 in.

$P_{\text{dc}}$  total dc radiant power at 0 in.

There are three FOM's that are applicable to the performance of the sway channel: (1) effective radiant power for 1/16-in. sway, (2) S/N ratio for 1/16-in. sway, and (3) sway resolution. Evaluation of equation (B34) by using equations (B26) and (B27), leads to the values shown previously for effective radiant power for 1/16-in. sway. Evaluation of equation (B32) by using equations (B1) and (B34) leads to the following S/N ratio for 1/16-in. sway:

$$S/N = \left( \frac{D_{\max}^*}{[A_s \Delta f']^{1/2}} \right) (P_{\text{sway}}) \left( \frac{s}{s_{\text{ref}}} \right) \quad (\text{B35})$$

where

$A_s$  sway detector area

$P_{\text{sway}}$  radiant power from equation (B34)

$s$  sway, in.

$s_{\text{ref}}$  sway of 3 in.

Sway resolution is found by evaluating equation (B35) for an S/N ratio of unity and solving for  $s$ . See table of error channel performance on p. 33 for the cases noted.

#### Acquisition Gain Control Channel Performance

The only meaningful FOM applicable to the performance of the acquisition gain control (AQGC) channel is the total radiant flux, which is found as follows: total radiant flux is taken as the sum of energy contained in both phases of the reimaged filament. In the AQGC detector, there is a central dead zone that vignettes the image such that only 73 percent of the energy is detected. Using equation (B7) yields an effective radiant power:

$$P_{\text{AQGC}} = 0.73P_i$$

where

$P_i$  radiant flux found from equation (B1).

Note: Predicted angular resolutions of the two error channels, as well as the predicted sway resolution are two orders of magnitude below the values observed when the autocollimator is in actual use. The discrepancy is due to the degrading effect of atmospheric turbulence, which prevents the autocollimator from approaching the theoretical performance limits predicted.

#### Light Sources

During the design study phase, a review of all available light sources was made. Although particular emphasis was placed on the evaluation of new developments, such as gas lasers and solid-state emitters, a tungsten filament lamp was selected as the source.

Evaluation of each source was based on the following criteria:

- (1) Spectral characteristics (brightness)
- (2) Uniformity of brightness over the effective source area
- (3) Lifetime
- (4) Stability
- (5) Complexity of the associated electronics

The following table summarizes the light source characteristics:

	Tungsten		Quartz-line lamp	Glow discharge	Gas laser	Solid state	Arc lamps
	Ribbon	Coil					
Brightness in 0.7- to 2.6- $\mu\text{m}$ band	a~50	a~25	b55	~23	~125	~10 <sup>-3</sup>	>50
Spectral characteristics	Continuous	Continuous	Continuous	Emission lines	Narrow band	Narrow band at 0.9 $\mu\text{m}$	Continuous with lines
Uniformity of brightness	Excellent	Good	Good	Good	Insufficient area	Insufficient area	Poor
Number of sources needed	1	1	1	3	3	3	1
Stability	Good	Good	Excellent	Good	Poor	Poor	Poor
Lifetime, hr	>10 000	>10 000	<1000		10 to 100	<10 000	<10
Complexity of associated electronics	Very simple	Very simple	Very simple	Modest	High	Modest	High

<sup>a</sup>At 2500-K color temperature with 50-percent coil filling factor.

<sup>b</sup>At minimum color temperature of 2900 K with 50-percent coil filling factor.

Results of the sources considered are summarized in the following table:

Detector	Peak $D_{\text{avg}}^*$ , $\lambda$	Wavelength of peak <sup>a</sup> , $\mu\text{m}$	Long wavelength cutoff, $\lambda_{\text{cut}}$ , $\mu\text{m}$	Response time, $t$ , $\mu\text{sec}$
Gallium arsenide	10 <sup>13</sup>	0.85	0.95	>400*
Silicon	2 $\times$ 10 <sup>12</sup>	.9	1.1	>500*
Germanium	2 $\times$ 10 <sup>10</sup>	1.6	1.8	<100
Lead sulfide	10 <sup>11</sup>	2.4	2.8	<300
Lead selenide	3 $\times$ 10 <sup>8</sup>	3.5	4.3	<4
Indium arsenide	3 $\times$ 10 <sup>9</sup>	3.4	3.7	<1
Indium antimonide	5 $\times$ 10 <sup>7</sup>	6.6	7.4	<.2

<sup>a</sup>The wavelength depends on the mode of operation: it is much shorter for the photoconductive mode of operation.

Spectral characteristics. - A tungsten lamp is essentially a blackbody whose brightness is given by Planck's law modified by the emissivity of tungsten. Tungsten lamps are operated in the 2500- to 3000-K color-temperature region where approximately 80 percent of all radiant energy falls within the 0.7- to 2.6- $\mu\text{m}$  band as shown in the following table:

Color temperature, K	Total brightness, W/cm <sup>2</sup>	Wavelength range of channel, $\mu\text{m}$		
		0.6 to 1.3	1.3 to 1.8	1.8 to 2.7
		<sup>a</sup> Radiated energy in each channel, percent		
2500	75	0.32	0.23	0.24
3000	150	.42	.22	.18

<sup>a</sup>The relatively even distribution of energy between the three spectral channels permits the use of a single source, rather than the three sources that would be needed if monochromatic sources were used. This is a distinct advantage, as a multiple source system would result in a considerably more complicated and costly autocollimator.

Uniform brightness over the effective source area. - Use of ribbon filaments provides uniform source areas and negligible shifts in color temperature across the ribbon; whereas, coil filaments cause small-scale nonlinearities in the error signal and nonuniform color temperatures across the filament image due to cooling effects at the outside of the coils - causing degradation in the overall linearity.

Lifetime. - Requirements are for a lifetime in excess of 10 000 hr, a figure easily achievable by reducing the lamp voltage. For the ribbon filament lamp used, lifetime is proportional to the eighth power of the voltage. For example, the following table shows lifetimes attainable as a function of operation voltage and temperature:

Voltage, V	Color temperature, K	Lifetime, hr
5.0	2850	1 250
3.9	2400	10 000

Stability. - Output of the lamp should not drop more than 20 percent because of bulb blackening only. Bulb blackening occurs when tungsten is deposited on the interior of the glass envelope. The autocollimator AGC can easily adapt to this gradual change. Short-term stability is excellent since tungsten filaments do not suffer instantaneous changes in output.

Complexity of associated electronics. - With the tungsten lamp, the electronics are very simple and straightforward because of the modest power requirements and low operating voltage.

## Sources Considered

Halogen cycle (quartz-line) tungsten lamp. - This lamp was considered because of its broad spectral bandwidth and high-output tungsten characteristics, coupled with its unique quartz-line characteristic of no bulb blackening (bulb blackening is avoided by filling the bulb envelope with a halogen gas). However, several disadvantages do exist - coil filament, limited lifetime, necessity for a combination lamp mount and heat sink, and minimum operating color temperature.

Glow discharge lamp. - Glow discharge lamps (neon, glow tube, etc.) have two fundamental disadvantages - low output and a spectral output composed of emission lines distributed over a small portion of the 0.7- to 2.0- $\mu\text{m}$  spectral operating range. One would need three glow lamps to satisfy the requirements.

Arc lamps. - These lamps suffer from several serious disadvantages - poor stability, small non-uniform source area, very short lifetimes, and very high power demand.

Gas laser. - The continuous wave (CW) gas laser has three attractive and familiar characteristics - very high brightness and directionality and highly monochromatic plane-polarized output. Of these, the first two characteristics lend themselves to theodolite application, especially for long-range operation and for applications where high power is needed to penetrate fog or clouds. Gas lasers are available in a wide range of wavelengths and in a range of output power (1 mW to 100 W).

The third characteristic, monochromaticity, would dictate the use of three lasers as the source in the present theodolite design. This is highly undesirable, since it would substantially increase the complexity of the optics, as well as the electronics.

Another problem involved in the use of lasers in the present design arises from the small effective source area of the laser. If the beam were focused into an  $f/4$  beam (necessary to fill the autocollimator aperture), the effective source area would be a diffraction-limited spot size several orders of magnitude smaller than the required source area. To correct this problem, the source optics would have to de-focus the beam in some way or use fiber optics to fill the required source area while maintaining the  $f/4$  angle. Such de-focusing or scrambling would effectively reduce the original laser brightness and, thus, reduce or eliminate its primary advantage over a tungsten source.

Although the laser has great potential for autocollimated systems in general (particularly star-tracker systems not requiring a finite source-radiating area), their application to the present class of instruments does not appear feasible at this time.

Solid state diodes. - These devices suffer from a number of disadvantages for our application, including (1) low output, (2) narrow spectral bandwidth - on the order of 0.1  $\mu\text{m}$ , (3) small source area, and (4) poor stability.

While there may be future developments of stable, high-output diodes that have emitting areas large enough to use in the present design, the narrow

spectral bandwidth of high-output diodes would still require the use of three separate sources. Thus, the diode is eliminated as an autocollimator source.

## MODULATION

The method of source modulation is dependent to a large extent on the type of source being utilized. Since a ribbon strip tungsten filament was selected as the source, our attention is restricted to means of modulating this type of source.

Direct electrical modulation, either by using pulses or half-wave rectified sine waves, is practicable only at very low frequencies. The thermal inertia of the large filament precludes direct modulation of the source at frequencies above 30 Hz. At 30 Hz, the percentage modulation would be very small, on the order of 3 to 5 percent. It is possible to operate a system at 30 Hz, but the signal-to-noise ratio would be very poor because of the low percentage modulation.

In addition, detector and transistor noise increase significantly at low frequencies as both devices are operating in the  $1/f$  noise region. The size of electrical components required, such as inductors and capacitors, increase significantly at this low frequency. An amplifier required to pass 30 Hz without significant phase distortion would require a low-frequency cutoff of less than 2 Hz.

The primary advantage of direct modulation is the absence of moving mechanical parts. Since this is an important consideration in establishing the reliability of the instrument, other static modulators were investigated. Among those are Kerr, Pockels, and Faraday cells. These static optical modulators have a number of advantages such as (1) no moving parts, (2) low power consumption, and (3) operation over a wide frequency range.

Kerr and Pockels cells are electro-optical devices which utilize an electrostatic field. This field is applied to certain materials to produce changes in the optical properties which cause an intensity modulation of the source.

In the Pockels cells, electric fields are applied to certain crystals such as ammonium dihydrogen phosphate (ADP) or potassium dihydrogen phosphate (KDP). These crystals, on application of the field, change from uniaxial to biaxial. Amplitude modulation is accomplished by passing a linearly polarized light beam through the modulator and then through another crossed polarizer. The application of a voltage will change the linearly polarized light to elliptically polarized light. The amplitude of the light passing through the crossed polarizer will be a function of its ellipticity and, therefore, of the voltage on the crystal. Kerr cells function in much the same manner except that the material used is a liquid (nitrobenzene) instead of a crystal.

However, these modulators suffer from a number of serious disadvantages, particularly the low long-wavelength-transmission cutoff  $\lambda_{cut}$ , which is  $1.8 \mu\text{m}$ . Nitrobenzene and bromobenzene do exhibit increases in transmission, but they are beyond  $3.0 \mu\text{m}$ . Thus, these devices cannot be used - especially for the sway-AQGC channel ( $1.8$  to  $2.8 \mu\text{m}$ ). Other disadvantages of these modulators are that (1) high voltages are required for effective modulation (2000

to 20 000 V), and that the (2) light is polarized - the dichroic filters used for spectral separation react differently to polarized light. Changes in the light angle of incidence cause the cutoff points of the filters to shift drastically.

The Faraday cell also utilizes the rotation of a polarized light beam to cause extinction of the source, but with one difference. The Faraday cell utilizes a magneto-optical effect where the magnetic field causes the change in the optical properties of the material - usually bromobenzene. This cell has the same advantages and disadvantages mentioned before, except that high voltage is not required but high currents are required to provide a sufficiently intense magnetic field.

Consideration was also given to the use of a "tuning fork light chopper," (eg., American Time Division). However, the main disadvantage of the tuning fork modulator is the limited amplitude of its blade. The maximum displacement of the chopper blade is 0.080 in., hence chopping must be done when the light beam width is small (i.e., near the focal point of the system) resulting in degradation of the signal shapes.

Consideration was now given to a motor-driven chopper. The disadvantage of a well-balanced motor is its limited bearing life. However, since the motor in a chopper application essentially experiences no axial and very small radial forces, bearing life is greatly extended.

The main advantage of the motor-driven chopper is the great flexibility in positioning the chopper blades in the optical system. The synchronous motor provides a high-reliability device with flexibility in the design and, therefore, was maintained for our design.

## DETECTORS

Infrared detectors can be classified by their mechanism of detection. There are two broad classes of detectors (1) thermal, or phonon detectors, and (2) photon detectors.

Thermal detectors utilize some temperature-dependent property, such as resistivity of thermoelectric effect, to produce an electrical output when exposed to radiation. These detectors have a number of advantages to recommend them, but their primary disadvantage - a long time constant - precludes their use in our design, (time constants vary from 30 msec to several seconds). The chopping frequency we are to employ requires detectors with time constants no greater than 300  $\mu$ sec.

Photon detectors, which include both photoemissive and solid-state devices, depend on the interaction of incident photons which are absorbed in the material to produce excess charge carriers. These detectors respond to the rate at which the photons are absorbed, hence, their spectral response is dependent on the energy of the photons. This means that the detector sensitivity is a function of the wavelength of the radiation. Photon devices have two advantages over thermal detectors, their response time is much shorter (on the order of 1  $\mu$ sec to 1 msec), and, since their spectral response is limited, their response to background noise is less.

In photoemissive devices, such as photodiodes and photomultipliers, electrons are physically ejected from the photosensitive surface and accelerated by an electrostatic field. Photomultiplier tubes provide high sensitivity, frequency response up to the megahertz range, and low noise, but their primary disadvantage is their limited spectral sensitivity. In our region of interest, 0.7 to 1.35  $\mu\text{m}$ , the quantum efficiency is very low, below 0.5 percent. The inherent gain of the photomultiplier is thus negated by the low efficiency of the photocathode. Because of their low quantum efficiency and their need for high-voltage supplies, photoemissive devices are not considered for our design.

The remaining class of photon detectors, solid-state devices, includes materials such as gallium arsenide and selenium. These detectors may operate in the photoconductive mode or photovoltaic mode. Some devices, such as silicon photodiodes, can be operated in either mode. Other materials, such as lead sulfide (PbS,) can be operated only in the photoconductive mode.

From the table on p. 36, the factors of primary importance are (1) the detectivity  $D_{\text{avg}}^*$  or FOM for the detector and (2) the long-wavelength cutoff  $\lambda_{\text{cut}}$ .

Detectivity is a measure of the S/N ratio of the detector

$$D_{\text{avg}}^* = \frac{1/\text{noise equivalent power}}{[(\text{area})(\text{bandwidth})]^{1/2}}$$

(Average detectivity is expressed in  $\text{cm-Hz}^{1/2}/\text{W}$ ). Since detectivity is wavelength dependent, the S/N ratio is a function of the source temperature. It is also a function of the chopping frequency: it decreases for frequencies above the upper limit determined by the time constant  $\tau$  and for frequencies below approximately 300 Hz - the region of  $1/f$  noise. Over the frequency range determined by these upper and lower limits,  $D_{\text{avg}}^*$  is independent of frequency. The detectivity is also a function of temperature: it increases as temperature decreases.

The table on p. 36 shows that for the wavelength of interest (0.7 to 3.0  $\mu\text{m}$ ) lead sulfide (PbS) is most superior because it has a higher  $D_{\text{avg}}^*$  at all wavelengths of interest.

The use of different detectors for each channel - silicon in the synchro prism, PbS in the remaining channels - was considered but dropped because different preamplifiers would have to be supplied for each type of detector. The only justification for the use of silicon was its higher  $D_{\text{avg}}^*$ , but since a very good S/N ratio can be obtained with PbS in the synchro channel, it was decided to maintain the PbS detectors in all of the channels.

#### AUTOMATIC GAIN CONTROL

Experience gained with the Saturn AALT, pointed out the desirability of an automatic gain control (AGC) system (i.e., variations in atmospheric transmission, lamp voltage fluctuations, and lamp aging are the primary factors in producing scale factor variations). An AGC system can compensate for these changes and maintain a constant scale factor.

An AGC system has two important system parameters that determine the method of operation. One concerns the means of sensing the intensity variations and the other concerns the control method for varying the gain.

### Sensing Element

The first problem is primarily a function of the type of optical return element to be used. The ideal optical device would be an element whose return beam would be insensitive to either angular or translatory motion. Of the possible devices, Porro prisms are relatively insensitive to pitch motions about their apex but are sensitive to angular motions about the axis perpendicular to the apex. Plane mirrors would be even more unsuitable because they are sensitive to pitch as well as roll motions. The device that best approaches these requirements is a retroreflector prism.

Another factor to consider is lamp voltage deviations. Variations in lamp voltage will produce energy changes with their associated spectral shifts. A  $\pm 10$ -V change in line voltage will produce a  $\pm 100$  K variation in lamp temperature (data obtained from G.E. Bulletin No. 14). This will produce a less than 10 percent relative energy difference between the error and AGC channels.

### Control Method

The second problem is a more crucial one since there are a number of approaches that can be considered. Some of these are

- (1) Direct electrical control of lamp intensity
- (2) Mechanical control of lamp intensity (iris diaphragm device)
- (3) Control of detector bias
- (4) Control of amplifier gain
- (5) Combinations of (1) and (4)

### Lamp Control

With this method, two problems became immediately apparent:

(1) The lamp output underwent spectral shifts when the color temperature of the lamp was varied.

(2) The AGC range was limited to approximately 3 to 1.

The lamp spectral shifts were considered to be the most severe limitation on the use of this technique. Tungsten emission closely follows the Wein blackbody curve, which relates power output to temperature. As temperature rises, total power output increases; with this increase, a spectral displacement of peak power output also occurs. In other words, as the color temperature of the lamp changes, energy distribution in the theodolite channels changes. This error represented the main problem in using direct lamp control for the AGC, and direct lamp control was dropped from further consideration.

## Mechanical Control

Mechanically controlling the output energy by means of an iris diaphragm device would alleviate the spectral shift problem. This method, however, was not considered because of space limitations in the source - the detector assembly. A mechanical system would require a closed-loop servo system with a motor and gear-train assembly.

## Detector Bias Control

Detector bias control depends on the relationship between the detector signal and the bias voltage; that is,

$$e_1 = S*JE_B \quad (B36)$$

where

$e_1$  signal output voltage,

$S^*$  specific responsivity of the detector,  $\text{cm}^2/\text{W}$

$J$  specific brightness of the detector,  $\text{W}/\text{cm}^2$

$E_B$  bias voltage applied across the cell and load resistor,  $V$

From equation (B36) it can be seen that the output signal is directly proportional to the bias voltage. It is possible to operate the detectors under a varying bias voltage, thereby controlling the output and achieving an AGC system. The voltage regulator controlling the bias voltage would have to be located in the autocollimator preamp assembly. This location would create a severe packaging problem because of the limited space available in the preamp assembly. As a result, this alternative was not investigated further.

## AMPLIFIER GAIN CONTROL

The principle of the amplifier gain control (AMGC) of a signal utilizing some characteristic of the signal has been used for many years. Radio receivers, for example, use the level of the RF carrier to adjust the system gain for the audio signals. The carrier, and therefore the AMGC, is always present even when no audio information is present. If the carrier were not present, the AMGC would cease to function. The error signals in the theodolite, which represent a suppressed carrier system, have this characteristic at null. However, the AQGC channel, utilizing the sway prism, provides a carrier even when the error channels are at null.

Many control devices (such as diodes, lamps, thermistors, etc.) have utilized the carrier level. These devices depend on changes in either the gain or impedance level as the control signal is varied. Our demand for reliability and simplicity precluded the use of these elements, limiting the choice of control device to a solid-state unit (i.e., junction transistors, field-effect transistors, unjunction transistors, and diodes).

At low theodolite carrier frequency (266 Hz), these devices take advantage of the fact that the dynamic impedance  $i_{dy}$  is a function of the dc current.

At this time, the device with the best repeatability is a silicon diode. The choice of available diodes is large, but, since repeatability is important, those diodes that exhibit closely specified voltage-versus-current characteristics would be most suitable (e.g., JANIN3600) in balanced modulators and demodulators. (JANIN3600 has specified min-max limits on voltage versus current at five different current levels.)

The basic circuit, which utilizes a diode, is a resistive voltage divider composed of a static element, the resistors  $R_{ac}$  and  $R_{dc}$ , the dynamic control elements, and the diode  $CR_1$ . The dynamic resistance of a diode can be expressed as

$$R_{dy} = \frac{nB^* T_{ab}}{qI_f} + R_s$$

where

$n$  approximately 2.00

$B^*$  Boltzmanns constant =  $1.38 \times 10^{-23}$  W sec/K

$T_{ab}$  absolute temperature, K

$q$  electron charge =  $1.6 \times 10^{-19}$  C (coulombs)

$I_f$  control current level, A

$R_s$  series ohmic resistance ( $\approx 1$  to  $2 \Omega$ ; is usually neglected)

The variable  $n$  is dependent on the carrier lifetime, which in turn is dependent on the doping. The value of  $n$  could be as low as 1 for other diodes with different levels of doping and with different doping materials.

At 25 °C,

$$\frac{nB^* T_{ab}}{q} = 0.052 \text{ V}$$

Therefore,

$$R_{dy} = \frac{52 \times 10^{-3}}{I_f \times 10^{-3}} = \frac{52}{I_f}$$

where  $I_f$  is given in mA. At a current level of 1 mA,  $R_{dy} = 52/I_f = 52 \Omega$ .

The dc control current, which is a function of the AMGC voltage, flows through  $R_1$  and diode  $CR_1$ . It is prevented from appearing at the output

terminal by the blocking capacitor  $C_1$ . The capacitor does allow the ac signal voltage to pass.

The AMGC control voltage ( $E_{AMGC}$ ) ranges from 20 to 1.5 V; therefore, the control current ranges from  $I_{f1}$  to  $I_{f2}$  where

$$I_{f1} = \frac{E_{AMGC} - E_D}{R_{tot}} = \frac{20 - 0.57}{20 \text{ k}\Omega} = 0.97 \text{ mA}$$

$$I_{f2} = \frac{E_{AMGC} - E_D}{R_{tot}} = \frac{1.5 - 0.44}{20 \text{ k}\Omega} = 0.053 \text{ mA}$$

and the dynamic resistance  $R_{dy}$  is

$$R_{dy,1} = \frac{52}{I_D} = \frac{52}{0.485 \text{ mA}} = 109 \Omega$$

(B37)

$$R_{dy,2} = \frac{52}{I_D} = \frac{52}{0.026 \text{ mA}} = 2000 \Omega$$

The diode current  $I_D$  used in equation (B37) is one-half the control current  $I_f$  since in actual operation there are two diodes in shunt with each other and the control current divides equally.

The attenuation ratio  $A^*$  of the resistor diode voltage divider is given by

$$A^* = \frac{e_{out}}{e_{sig}} = \frac{R_{dy}}{R_{ac} + R_{dy}}$$

$$A_1^* = \frac{109 \Omega}{16.1 \text{ k}\Omega} = 6.64 \times 10^{-3} \approx \frac{1}{150}$$

$$A_2^* = \frac{2.0 \text{ k}\Omega}{18.1 \text{ k}\Omega} = 0.110 \approx \frac{1}{9.09}$$

and the ac range is therefore

$$\frac{A_2^*}{A_1^*} = \frac{\frac{1}{9.09}}{\frac{1}{150}} = 16.5 \text{ to } 1$$

Since the ac signal also flows through the diode, it could produce a fluctuation in the dynamic resistance. This fluctuation would result in the dynamic resistance varying as a function of signal level and would produce

nonlinear operation and some distortion. The signal current must be at least 10 times smaller than the AMGC control current to reduce this distortion. The maximum signal under normal conditions with an AMGC voltage of 10 V is approximately

$$I_{\text{sig}} = \frac{200 \times 10^{-3}}{16.1 \mu\text{m}} = 24 \text{ mA}$$

the control current is

$$I_{\text{AMGC}} = \frac{10 \text{ V} - 0.55}{20 \mu\text{m}} = \frac{9.45}{20 \mu\text{m}} = 0.472 \mu\text{A}$$

one-half of this flows through each diode; thus,

$$I_{\text{AMGC}} = \frac{472 \times 10^{-6}}{2} = 236 \mu\text{A}$$

and the criteria of  $I_{\text{AMGC}} \geq 10 (I_{\text{sig}})$  is satisfied.

Since a small amount of distortion will occur, a push-pull arrangement using a center-tapped feed transformer was adopted - but the basic operation remains as described.

#### VISUAL SYSTEM

The visual system was incorporated as designed for the AALT system. A 0.8-mm-thick, thin-plane, parallel, dichroic beamsplitter made of Infrasil I and a dichroic coating replaced the old pellicle that was used as a beam splitter. Basically, no other changes were made.

#### SENSING PRISM

An attempt was made to increase the optical efficiency of the sensing prism and its effect on the S/N ratio.

The nose of the sensing prism is located exactly at the focus of the parabolic mirror, and the images of the filaments are also focused in the same plane by the source-imaging optics. Since the energy in the images of the filament is great compared to the returned energy per arc-sec, even small imperfections in the prism coating, which can allow light to fall on the detectors, will cause relatively large bias signals.

One of the problems encountered with complex 36's existing LR2A theodolite was that stray light entered the slit and fell on the detectors. Since this light was modulated, any imbalance in the magnitude of the two phases became a fixed electronic bias. This imbalance was caused by imperfect slit edges resulting from the metallic coating flaking off the nose of the prism during

the polishing process. Only when both edges were perfect or the area of the defects in edges were exactly equal, would the electronic bias be zero.

The first approach was to attempt to eliminate the coating problem by using the principle of total internal reflection. Total internal reflection occurs when light rays are incident on a surface from the denser side and at an angle of incidence the sine of which is greater than

$$\frac{\text{index of refraction (less dense)}}{\text{index of refraction (denser)}}$$

The critical angle for fused quartz is given as

$$\sin \theta_{\text{crit}} = \frac{n_{\text{air}}}{n_{\text{quartz}}} = \frac{1}{1.45}$$

where  $\theta_{\text{crit}} = 43^{\circ}36'$  and

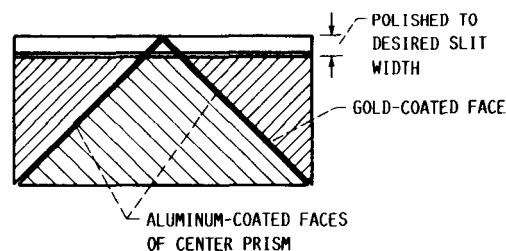
$n_{\text{air}}$  index of refraction of air

$n_{\text{quartz}}$  index of refraction of quartz

Any ray with an incidence angle greater than  $43^{\circ}36'$  will be totally reflected with essentially no loss in energy. Conversely, any ray incident at less than  $43^{\circ}36'$  will be transmitted.

One of the main problems with the internal reflection prism, excluding fabrication, is that the reflecting surface is not completely opaque except under certain conditions (when the surface is absolutely clean and the rays are incident at an angle greater than the critical angle).

The final approach to the sensing prism (for manufacturing reasons) was to fabricate a prism like that shown in the following sketch:



This prism is composed of two prisms with gold-coated surfaces cemented to a central prism with aluminum-coated faces.

#### AUTOCOLLIMATOR ACQUISITION RANGE

The autocollimator is characterized by a limitation on the acquisition range at a given operating distance defined as

$$\theta_{\max} = \frac{d_{\text{lens}} + W_{\text{rf1}}}{2d_o}$$

where

$\theta_{\max}$  maximum mirror angular travel which will return light to the autocollimator

$d_{\text{lens}}$  autocollimator objective lens diameter

$W_{\text{rf1}}$  reflector width

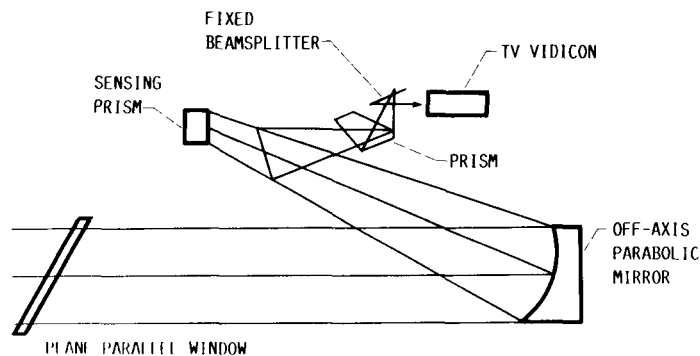
$d_o$  operating distance

No problems were expected with the acquisition range.

### Primary Mirror

The primary optical system is an off-axis Maksutov catadioptric consisting of a spherical primary mirror and a corrector shell. Fabrication of the spherical mirror is simple, but fabrication of the corrector shell is difficult, because of the steep curvature of the two surfaces and the need for one of these to be asperized.

Since the only purpose of the window is to act as a seal and to allow transmission of energy from 0.4 to 2.7  $\mu\text{m}$  without optical degradation, the window as designed, is a thin, circular, plane-parallel plate of fused silica (Infrasil number 1). This is the unit that was employed:



### Linearity Improvement

Methods for improving signal linearity and symmetry were evaluated concurrent with the investigation of light sources. Since the sensing prism slit is linear, it is obvious that either the use of a source with a uniform radiating area or methods for averaging out source irregularities should improve linearity characteristics.

The initial step was to evaluate the use of fiber optics as part of the source-lamp reimaging scheme. This could eliminate irregularities in the incandescent filament structure and make lamp-filament alignment uncritical. For infrared transmission, energy loss in the channels could be substantial - this feature makes it quite unfeasible.

A review of various types of tungsten filament lamps led to the choice of a ribbon filament as the source. Thus, the ribbon filament was chosen to achieve the linearity and symmetry based on its temperature variations. System tests conducted at 800 ft (ideal weather conditions) showed that the autocollimator was linear and symmetrical to  $\pm 15$  arc-sec.

#### AUTOCOLLIMATOR MEASURING CHARACTERISTICS

The autocollimator measuring characteristics, when monitoring a mirror, are determined basically by the autocollimator aperture, the reflector aperture, and the operating distance. The angular acquisition range  $\theta_{total}$  for an ideal autocollimator is

$$\theta_{total} = \frac{d_A + W_{rf1}}{2d_o}$$

where

$d_A$  autocollimator aperture

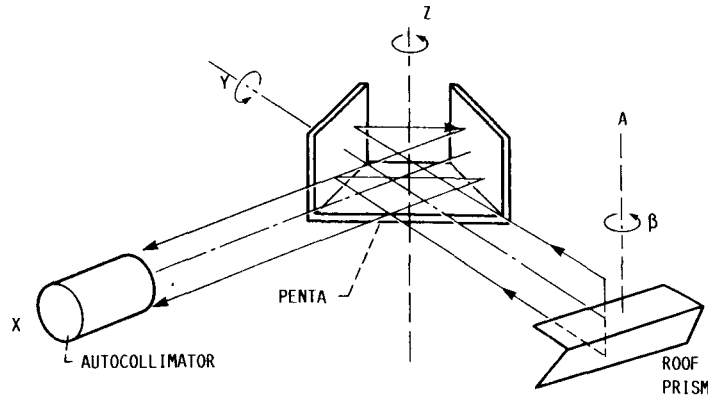
$W_{rf1}$  reflector width

$d_o$  operating distance

The autocollimator is capable of monitoring the translation of a retro-reflector and in this sense has an acquisition and monitoring range whose characteristics are controlled only by the autocollimator aperture, source configuration, target size, operating range, autocollimator vignetting, and detector configuration. There is no image motion at the focal plane when the target prism is translated, but only changes in the energy content of the image. It is the unique combination of source configuration, retroreflector, and detectors that gives the autocollimator the capability of measuring prism translation.

#### PENTA MIRROR ROTATION ERRORS IN A SINGLE-AXIS ALIGNMENT SYSTEM

Analyses of the autocollimator/penta/roof-prism single-axis alignment system indicated that readings are insensitive to penta rotations about two orthogonal axes. When the penta is rotated by the angle  $Y$  about its exit ray, the azimuth reading is only in error by  $-Y^2$ , provided the roof prism captures the center of the autocollimator beam. (See the following sketch of the optical azimuth-alignment system.)



The autocollimator measures angular rotations  $\beta$  of the roof prism about the Z-axis. The penta mirror or optical square is used to deflect the autocollimator line of sight by  $90^\circ$  or to allow parallel translation of the line of sight. The autocollimator measurements may be disturbed by rotations of the deflecting device. A penta mirror is chosen as a deflector because rotations of the penta mirror about its principal axis (the Z-axis when  $X = Y = 0$ ) will not cause error deviations of the line of sight nor introduce errors in the autocollimator readings.

Penta rotations may also occur about the X- and Y-axes, and mathematical analyses indicated that

(1) Penta rotation about the X-axis produces no significant deviation of the center of the autocollimator return image and therefore introduces no significant errors in the readings.

(2) Penta rotation about the Y-axis does produce deviations. For example, let the autocollimator monitor a roof prism rotation of angle  $A$ . Let the penta be rotated by the angle  $Y$  about the Y-axis, and by the angle  $X$  about the X-axis. Let  $\phi$  equal the autocollimator reading. Then

$$\phi = A - Y^2 \quad (B38)$$

(3) Penta rotation does cause rotation of the autocollimator return image about its center. Let the rotation angle be  $\sigma$ . Then

$$\sigma = 2(X - Y) \quad (B39)$$

(4) No matter how the penta is tilted, rotation about its principle axis Z produces no errors.

These conclusions assume that all elements are large enough to capture the center of the autocollimator beam.

The angles  $\phi$  and  $\sigma$  have been computed precisely (by Perkin Elmer) from exact formulas to twelve significant figures and have been compared with  $\phi$  and  $\sigma$  computed from simplified formulas (eqs. (B38) and (B39)) for various cases of interest. The results from the approximate formulas (eqs. (B38) and (B39)), are quite accurate for the usual small angles encountered when autocollimators are used. Percentage error is defined as one hundred times the approximate value minus the true value, then divided by the true value.

## MATRIX ALGEBRA MODEL

A matrix algebra model of the alignment system was constructed for analytical investigation and programmed for digital computation. In the model, a column matrix or vector  $\underline{G}$  represents a geometric ray,

$$\underline{G} = \begin{bmatrix} l \\ m \\ n \end{bmatrix} \quad (\text{B40})$$

where components  $l$ ,  $m$ , and  $n$  are direction cosines of the ray. The ray has a single positive direction such that the return ray along the path taken by  $\underline{G}$  is  $-\underline{G}$ .

A square matrix  $\underline{M}$  represents a plane mirror where  $a$ ,  $b$ , and  $c$  are the direction cosines of a unit normally directed outward from the reflecting surface. Then

$$\underline{M} = \begin{bmatrix} 1-2a^2 & -2ab & -2ac \\ -2ab & 1-2b^2 & -2bc \\ -2ac & -2bc & 1-2c^2 \end{bmatrix} \quad (\text{B41})$$

Reflection of a ray  $\underline{G}$  by a plane mirror  $\underline{M}$  is represented by the matrix multiplication  $\underline{G}' = \underline{M}\underline{G}$ , where  $\underline{G}'$  is the reflected ray. If the ray is first reflected by the mirror  $\underline{M}_1$  and then reflected by the mirror  $\underline{M}_2$ , we have  $\underline{G}' = \underline{M}_1\underline{G}$  and  $\underline{G}'' = \underline{M}_2\underline{G}'$ . By the associative law for matrix multiplication, we also have  $\underline{G}'' = \underline{M}_2\underline{M}_1\underline{G} = \underline{M}_{1,2}\underline{G}$ , where  $\underline{M}_{1,2} = \underline{M}_2\underline{M}_1$ . Thus if a ray undergoes consecutive reflections by the system of plane mirrors  $\underline{M}_1, \underline{M}_2, \dots, \underline{M}_n$ , the system is represented by the matrix  $\underline{M}_{1,2,\dots,n}$ .

An optical element composed of several plane reflecting surfaces is thus represented by a matrix which is the product of the matrices representing the individual plane reflecting surfaces, taken in the same order as the order of reflection.

In particular, a roof prism whose roof edge is parallel to the X-axis is represented by the matrix

$$\underline{R}_X = \begin{bmatrix} 1 & 0 & 0 \\ 0 & -1 & 0 \\ 0 & 0 & -1 \end{bmatrix} \quad (\text{B42})$$

A penta whose principal axis is parallel to the Z-axis is represented by the matrix

$$\underline{P}_Z = \begin{bmatrix} 0 & 1 & 0 \\ -1 & 0 & 0 \\ 0 & 0 & 1 \end{bmatrix} \quad (\text{B43})$$

The rotation of a plane mirror  $\underline{M}$  or optical element is represented by the similarity transformation  $\underline{U}^{-1}\underline{M}\underline{U}$ , where  $\underline{U}$  is the desired orthogonal rotation matrix. For rotations of the angles  $X$ ,  $Y$ ,  $Z$ , and  $A$ , the transformation matrices are

$$\underline{U}_X = \begin{bmatrix} 1 & 0 & 0 \\ 0 & \cos X & \sin X \\ 0 & -\sin X & \cos X \end{bmatrix} \quad (\text{B44})$$

$$\underline{U}_Y = \begin{bmatrix} \cos Y & 0 & \sin Y \\ 0 & 1 & 0 \\ \sin Y & 0 & \cos Y \end{bmatrix} \quad (\text{B45})$$

$$\underline{U}_Z = \begin{bmatrix} \cos Z & \sin Z & 0 \\ -\sin Z & \cos Z & 0 \\ 0 & 0 & 1 \end{bmatrix} \quad (\text{B46})$$

and

$$\underline{U}_A = \begin{bmatrix} \cos A & \sin A & 0 \\ -\sin A & \cos A & 0 \\ 0 & 1 & 1 \end{bmatrix} \quad (\text{B47})$$

Since the transformation matrices are orthogonal, their inverse  $\underline{U}^{-1}$  is equal to their transpose  $\underline{U}^T$ ; that is,  $\underline{U}^{-1}\underline{M}\underline{U} = \underline{U}^T\underline{M}\underline{U}$ .

To locate the autocollimator return image, two rays must be traced through the system. Let the two rays be (1) ray  $\underline{C}$  originating from the center of the autocollimator object and passing through the optical center of the autocollimator objective lens and (2) ray  $\underline{D}$  originating from the upper extreme of the autocollimator azimuth object and also passing through the optical center of the objective. The autocollimator has its line of sight directed parallel to the negative  $X$ -axis. The upper half of the autocollimator azimuth object subtends an angle  $D$  at the objective; thus,

$$\underline{C} = \begin{bmatrix} -1 \\ 0 \\ 0 \end{bmatrix} \quad \text{and} \quad \underline{D} = \begin{bmatrix} -\cos D \\ 0 \\ -\sin D \end{bmatrix} \quad (\text{B48})$$

Since both of these rays must be reflected through the alignment system, it is convenient to combine them into one autocollimator matrix  $\underline{A}$ , where

$$\underline{A} = \begin{bmatrix} \underline{C}, \underline{D} \end{bmatrix} = \begin{bmatrix} -1 & -\cos D \\ 0 & 0 \\ 0 & -\sin D \end{bmatrix} \quad (\text{B49})$$

The return image matrix  $\underline{A}'$  is then

$$\underline{A}' = \begin{bmatrix} C_X & D_X \\ C_Y & D_Y \\ C_Z & D_Z \end{bmatrix} \quad (\text{B50})$$

This return image matrix may be interpreted as follows:

(1) The autocollimator azimuth reading  $\phi$  is

$$\phi = \frac{1}{2} \tan^{-1} \left( \frac{C_Y}{C_X} \right) \quad (\text{B51})$$

(2) The autocollimator elevation reading  $\psi$  is

$$\psi = \frac{1}{2} \tan^{-1} \left( \frac{C_Z}{C_X} \right) \quad (\text{B52})$$

(3) Then the return image rotation angle  $\sigma'$  is

$$\sigma' = \tan^{-1} \left( \frac{C_X D_Y - C_Y D_X}{C_Z D_X - C_X D_Z} \right) \quad (\text{B53})$$

(4) Now the entire alignment system is represented by

$$\underline{A}' = \underline{U}_X^{-1} \underline{U}_Y^{-1} \underline{P}_Z^L \underline{U}_Y \underline{U}_X \underline{U}_A^{-1} \underline{R}_X \underline{U}_A^{-1} \underline{U}_Y^{-1} \underline{P}_Z \underline{U}_Y \underline{U}_X \underline{A} \quad (\text{B54})$$

where  $\underline{P}_Z^L$  is the similarity transform of  $\underline{P}_Z$ . Note that  $\underline{P}_Z$  and  $\underline{P}_Z^L$  are invariant under similarity transformation by the matrix  $\underline{U}_Z$  (i.e.,  $\underline{P}_Z = \underline{U}_Z^{-1} \underline{P}_Z \underline{U}_Z$ ). Also note that the penta is first laid on the X-Y plane, then rotated by the angle  $Y$  about the Y-axis, and finally rotated by the angle  $X$  about the X-axis.

#### FORMULA FOR AZIMUTH READING

Beginning with equation (B54), let  $\underline{A}$  be replaced with  $\underline{C}$ , and  $\underline{A}'$  with  $\underline{C}'$  (the return central ray). After multiplication,  $\underline{C}'$  is found to be

$$\underline{C}' = \begin{bmatrix} C_X \\ C_Y \\ C_Z \end{bmatrix} \quad (\text{B55})$$

where

$$\underline{C}_X = 1 - 2 \cos A \sin^2 Y + \sin A \cos Y (\sin X \sin Y - \cos X)^2$$

$$\begin{aligned} \underline{C}_Y = & \sin 2A \cos^2 X \cos^2 Y - 2 \cos Y (\sin A \cos X \cos Y + \cos A \sin Y) \\ & \times [\sin A \sin X \cos Y (\sin X \sin Y - \cos X)] \\ & + \cos A \sin Y (\sin X \sin Y + \cos X) \end{aligned}$$

$$\begin{aligned} C_Z = & [2 \cos 2A \sin^2 Y \cos Y (\cos X \sin Y - \sin X) - 2 \sin^2 A \cos^2 X \cos^3 Y] \\ & \times (\cos X \sin Y + \sin X) + \sin 2A (1 + 2 \sin^2 Y) \sin X \cos X \cos^2 Y \\ & - \sin Y (1 - 2 \sin^2 Y) \end{aligned}$$

The azimuth reading  $\phi$  is then given by equation (B51). In particular, if all of the angles are zero,

$$\underline{C}' = \begin{bmatrix} 1 \\ 0 \\ 0 \end{bmatrix} \quad (\text{B56})$$

which is the case of perfect alignment (null).

As a third-order approximation for the small angles normally encountered when autocollimators are used, the small angle approximations may be substituted.

$$\left. \begin{aligned} \sin \theta &\cong \frac{\theta^3}{6} \\ \cos \theta &\cong 1 - \frac{\theta^2}{2} \end{aligned} \right\} \quad (\text{B57})$$

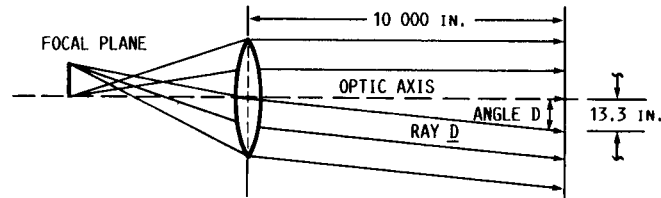
Neglecting all terms of orders greater than three, we have

$$\underline{C}' \cong \begin{bmatrix} 1 - 2A^2 + 4AY^2 \\ 2A - 2Y^2 - 2A \left( X^2 + Y^2 - \frac{2A^2}{3} \right) \\ 2(A - Y^2)(X - Y) - A^2(X + Y) \end{bmatrix} \quad (\text{B58})$$

We can now find  $\phi$  by substituting values of  $C_X$  and  $C_Y$  from equation (B58) into equation (B51) and using the third-order terms to measure the error in assuming the second-order approximation equation (B38).

## CENTER SHIFT ERRORS

Since the prism is held centered on the reticle and the penta rotation is small, the optical elements should capture the central rays of the autocollimator beam. The noncentral rays make a small angle with the optic axis, the maximum of which is angle  $D$ . For example,



Let  $D = 4$  min; let the penta be only a few feet from the autocollimator; let the roof prism be 10 000 in. from the penta; and, finally, let the front face of the penta be  $1\frac{1}{2}$  in.<sup>2</sup> The roof prism is positioned so that when  $X = Y = A = 0$  (system is nulled) the center of the roof prism captures the central ray. The ray  $\underline{D}$  is  $10^4$  in. ( $240$  in.)  $4.8 \times 10^{-6}$  rad/sec =  $11.5$  in. above the center of the roof prism and is therefore lost. If the small part of the beam that the roof prism captures consists of these rays, an azimuth error will result back at the autocollimator; the error should be very small to negligible.

For a penta rotation of angle  $X$ , the ray going into the roof prism can be found using the matrix technique. The rotated penta matrix is

$$\underline{P}_Z \text{ rotated} = \frac{U}{X}^{-1} \underline{P}_Z U_X = M_1$$

( $M_1$  is derived in equation (B59).)

$$\text{entrance ray} = \underline{D} = \begin{bmatrix} -\cos D \\ 0 \\ -\sin D \end{bmatrix}$$

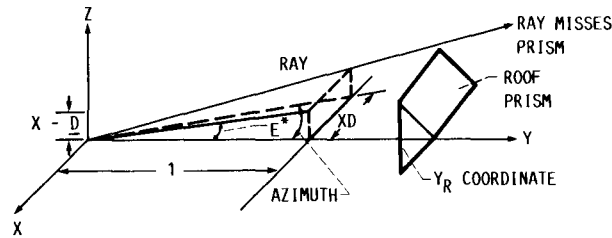
$$\begin{aligned} \text{roof prism input} = M_1 \underline{D} &= \begin{bmatrix} 0 & \cos X & \sin X \\ -\cos X & \sin^2 X & -\sin X & \cos X \\ -\sin X & -\sin X & \cos X & \cos^2 X \end{bmatrix} \begin{bmatrix} -\cos D \\ 0 \\ -\sin D \end{bmatrix} \\ &\cong \begin{bmatrix} -XD \\ 1 \\ X - \underline{D} \end{bmatrix} \quad \text{for small } X, \underline{D} \end{aligned}$$

$$E^* = \text{elevation angle} = \tan^{-1} \frac{(X - D)}{1}$$

For  $D = 0$  (central ray),

$$E^* = \tan^{-1}(X) \approx X \quad \text{for } X \text{ small}$$

Now ray  $\underline{D}$  subtends an angle  $D$  with respect to the optic axis. If the penta is rotated an angle  $X$  about the  $X$ -axis, this results in ray  $\underline{D}$  going through the roof prism, back into the penta prism and giving an output azimuth reading even though angle  $A = 0$ . (See the following sketch.)



To find its magnitude we rotate the penta through an angle  $X$  to give the penta matrix  $M^1 = \underline{U}_X^{-1} \underline{P}_Z \underline{U}_X$ . Thus,

$$\underline{D}_1 = M_1 \underline{D} = \text{input to roof prism}$$

$$\underline{D}_2 = \underline{R}_X \underline{D}_1 = \text{output of roof prism}$$

$$\underline{D}' = \underline{U}_X^{-1} \underline{P}_Z^L \underline{U}_X \underline{D}_2 = \text{output of penta desired}$$

Therefore,

$$\underline{D}' = \left( \underline{U}_X^{-1} \underline{P}_Z^L \underline{U}_X \right) \underline{R}_X \left( \underline{U}_X^{-1} \underline{P}_Z \underline{U}_X \right) = M_2 \underline{R}_X M_1 \underline{D}$$

$$\underline{P}_Z \underline{U}_X = \begin{bmatrix} 0 & \cos X & \sin X \\ -1 & 0 & 0 \\ 0 & -\sin X & \cos X \end{bmatrix}$$

$$M_1 = \underline{U}_X^{-1} \underline{P}_Z \underline{U}_X = \begin{bmatrix} 0 & \cos X & \sin X \\ -\cos X & \sin^2 X & -\sin X \cos X \\ -\sin X & -\sin X \cos X & \cos^2 X \end{bmatrix} \quad (B59)$$

$$\underline{R}_X M_1 = \begin{bmatrix} 0 & \cos X & \sin X \\ \cos X & -\sin^2 X & \sin X \cos X \\ \sin X & \sin X \cos X & -\cos^2 X \end{bmatrix}$$

$$\underline{P}_Z^L \underline{U}_X = \begin{bmatrix} 0 & -\cos X & -\sin X \\ 1 & 0 & 0 \\ 0 & -\sin X & \cos X \end{bmatrix}$$

$$M_2 = \underline{U}_X^{-1} \underline{P}_Z^L \underline{U}_X = \begin{bmatrix} 0 & -\cos X & -\sin X \\ \cos X & \sin^2 X & -\sin X \cos X \\ \sin X & -\sin X \cos X & \cos^2 X \end{bmatrix}$$

Therefore,

$$M_{2R_X} M_1 = \begin{bmatrix} -1 & 0 & 0 \\ 0 & \cos^4 X - \sin^4 X & 2 \sin X \cos X \\ 0 & 2 \sin X \cos X & \sin^4 X - \cos^4 X \end{bmatrix}$$

Finally, using

$$D = \begin{bmatrix} -\cos D \\ 0 \\ -\sin D \end{bmatrix}$$

and

$$D' = M_{2R_X} M_1 D = \begin{bmatrix} \cos D \\ -2 \sin D \sin X \cos X \\ -\sin D (\sin^4 X - \cos^4 X) \end{bmatrix}$$

for  $\underline{D}$  and  $\underline{X}$  small,

$$\cos D \cong 1$$

$$\sin D \approx D$$

$$\underline{D}' = \begin{bmatrix} 1 \\ -2DX \\ D \end{bmatrix} = \begin{bmatrix} D_X \\ D_Y \\ D_Z \end{bmatrix}$$

and using equation (B52) for azimuth error seen by the autocollimator

$$\phi = 1/2 \tan^{-1} \left( \frac{D_Y}{D_X} \right) \cong 1/2 \left( \frac{D_Y}{D_X} \right) = 1/2 \left( \frac{-2D_X}{1} \right) = -D_X$$

A simple calculation will show the maximum effect of penta X rotation coupled with the paraxial ray at D. From AALT theodolite data,  $D \cong 4$  min.

$$\begin{aligned}
 \text{Let } X &= 4 \text{ min,} \\
 \text{azimuth error} &\cong -D\chi = -X^2 \\
 &= -(1.15 \times 10^{-3} \text{ rad})^2 \\
 &= -(1.33 \times 10^{-6} \text{ rad}) \\
 &= 0.273 \text{ arc-sec}
 \end{aligned}$$

Since in practice, the prisms are kept centered in the field of view by the sway servo loop, the maximum penta rotation  $\chi$  is  $\pm 20$  arc-sec (maximum build-up of mechanical tolerances), the actual error including bearing eccentricity is

$$x_{\max} = \pm 20 \text{ sec} = 1.46 \times 10^{-4} \text{ rad}$$

$$\text{ecc} \cong 1 \text{ min} = 2.9 \times 10^{-4} \text{ rad}$$

$$\begin{aligned}
 \text{azimuth error} &= -x(\text{ecc}) = -(1.46 \times 10^{-4})(2.9 \times 10^{-4}) = 4.2 \times 10^{-8} \text{ rad} \\
 &= -0.009 \text{ arc-sec (which can be neglected)}
 \end{aligned}$$

#### SWAY SERVO ANALYSIS

The specifications to be met are

- (1) Sway displacement = 12 in. peak (sinusoidal)
- (2) Sway frequency  $\leq 0.75$  Hz
- (3) Sway error (dynamic)  $\leq 3/4$  in.
- (4) Porro prism mounted on Centaur's IMG platform
- (5) At sway null, equal amounts of both phases impinge on the sway detector

Assuming perfect square-wave chopping and balance, the ac signal from the detector is zero. There is a dc signal present resulting from the energy in the detector but this is not amplified by the ac preamplifier. When the sway prism translates, the energy from one phase increases while energy in the other phase decreases.

The amplitude of the ac component indicates how much the prism has translated. The phase (phase I or II increasing) indicates in which direction the Porro prism has moved - left or right.

As the vehicle translates, an error signal of the proper phase is generated so as to drive the penta carriage to establish a new null position. The penta carriage is driven by a motor through a Saginaw recirculating ball and lead screw unit. This unit converts the rotary motion of the motor to the linear motion required for the penta with a typical efficiency exceeding 85 percent. The lead screw has a 1:1 conversion ratio; one complete revolution of the shaft producing 1 in. of linear displacement. Drive force is provided by the dc voltage applied to the motor circuit armature.

Since the field of the motor is supplied by a permanent magnet, the only way of controlling the armature current or developed torque involves varying the dc voltage applied to the motor's armature terminals.

The requirement for large peak and transient currents utilizing this method of control has presented a problem in the past. With the availability of high-power SCR's and transistors, this is no longer a problem.

The initial investigation led to the consideration of using NASA's 28 V<sub>dc</sub> line for the primary power source. However, the large current drains, peak transient requirements of 40 A, and average requirements of 8 A during tracking would necessitate the use of heavy-duty connectors, relays, and other components. In addition, if a dc supply is used, the control of SCR elements becomes difficult because a means of commutating the SCR must be provided. Silicon power transistors could be utilized, but the large peak currents would necessitate large power transistors with the attendant requirements of heat sinks and driver amplifiers. With only a single polarity voltage available, a switching arrangement would have to be provided to reverse the motor.

For the foregoing reasons, it was decided to investigate the use of a modulated ac system for the servo amplifier. An ac system provides a number of advantages:

(1) Because of the higher line voltage, 115 V<sub>ac</sub> instead of 28 V<sub>dc</sub>, the ac line current will be less for a given power output. A transformer steps the 115-V<sub>ac</sub> voltage down to the 20 V<sub>rms</sub> required for the motor.

(2) The center-tapped transformer easily provides both voltage polarities, thus doing away with the necessity for a complex switching arrangement.

(3) Because of the reversing nature of the ac voltage, SCR's can be used without the necessity for commutating circuits.

There are two types of control devices that can be used in a modulated ac system - silicon power transistors and SCR's. The silicon power transistors have three main advantages over the SCR's.

- (1) Inherent turn-off capability
- (2) Slightly lower saturation voltage
- (3) Higher frequency capabilities

In a 400-cycle system, the first and third advantages are obviated, and it becomes necessary only to consider the saturation voltages.

Now, the SCR has three primary advantages over the power transistor:

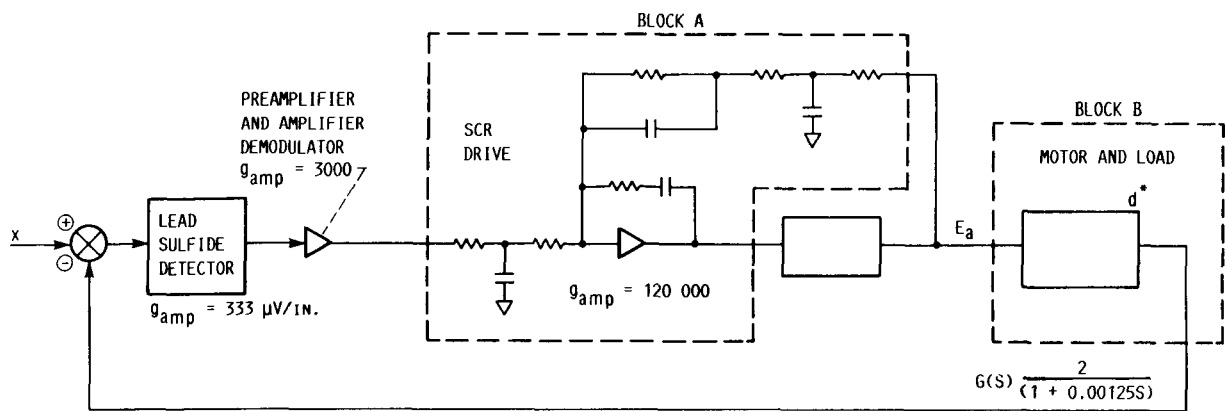
- (1) Higher voltage capability for a given power level
- (2) Higher peak transient and rms current capabilities, combined with high-voltage capability
- (3) Very sensitive gate action - small drive current required, usually no need for pre-driven stages

Since the ac voltages present are low (28 to 42 V peak), the higher voltage capability of the SCR is not a primary advantage as there are suitable silicon power transistors available. The SCR, then, possesses two main advantages: (1) the ability to withstand large transient currents and (2) the

extremely high gain low-gate-drive requirements. The advantage of low saturation voltages for transistors would be a factor to consider in extremely low voltage circuits, but for the ac voltages present, the higher voltage drop of the SCR is not a problem - thus, SCR's should be the control element for our system.

SCR's operate most efficiently when driven by pulses synchronized to the line. The pulses are provided a phase shifting saturable reactor unit manufactured by Sprague Electric and known as Silicontrol. One "Silicontrol" and its two SCR's provide full-wave operation of one voltage polarity. Another full-wave control unit is also needed to provide the opposite polarity voltage. The amount of phase shift of the gated pulse is proportional to the drive current. The average voltage developed by the SCR's is not linearly related to the phase angle, it is proportional to the sine of twice the phase angle plus the angle itself. Therefore a linear relationship does not exist between drive voltage into the gating units and SCR average output voltage. For purposes of analyses, the effect of this departure from a linear relationship is assumed to be small for small phase angles.

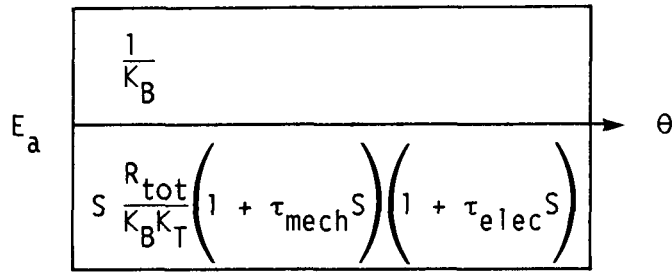
The Titan/Centaur and Atlas/Centaur Sway Servo system has one major and two minor feedback loops. (See the following sketch.)



The two minor loops serve to stabilize the operational amplifier, reduce the nonlinearity of the SCR drive, and provide a lower source impedance as seen by the motor. This last objective is necessary because SCR's appear as very high impedances when in the nonconducting state. These high impedances would allow the motor to coast inordinately unless other means were provided to damp it.

To facilitate analysis, we can reduce the elements in blocks A and B to a simplified equivalent form.

Block B, which represents the motor and its associated inertia load, can be reduced to one transfer function:



where

$K_B$  motor back electromotive force (EMF) constant; 0.108 V/rad/sec

$R_{tot}$  total armature resistance; 0.57  $\Omega$

$F_B$  viscous friction load;  $1.58 \times 10^{-3}$  lb-ft/rad/sec

$K_T$  torque constant;  $K_B/1.36 = 0.080$  lb-ft/A

$\tau_{mech}$  mechanical time constant; 0.140 sec

$\tau_{elec}$  motor electrical time constant;  $50 \times 10^{-6}$  sec

This transfer function (eq. (B60)) can now be simplified to

$$\frac{\theta}{E_a} = \frac{\frac{9.28}{0.104}}{S(1 + 0.140S)(1 + 50 \times 10^{-6}S)}$$

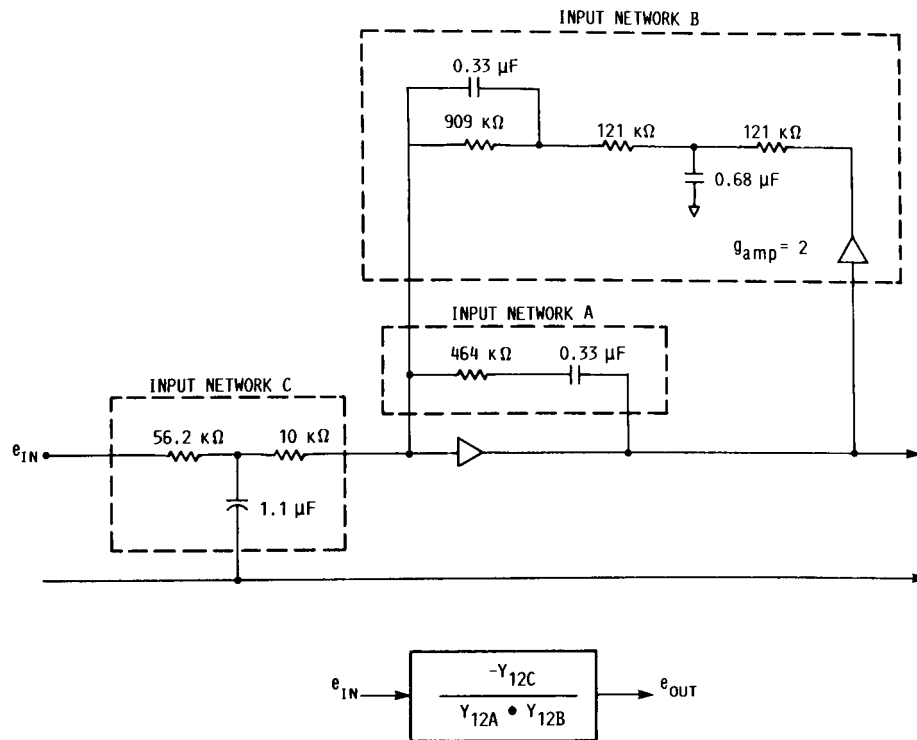
For the lead screw, the conversion factor is

$$\theta_{rad} = 24\pi d \quad (\text{for } d \text{ in feet})$$

$$\frac{d^*}{E_a} = \frac{\frac{89.3}{24\pi}}{S(1 + 0.140S)(1 + 50 \times 10^{-6}S)}$$

$$\frac{d^*}{E_a} = \frac{1.18}{S(1 + 0.140S)(1 + 50 \times 10^{-6}S)} = G(S)_{\text{Block B}}$$

Block A, which comprises the feedback and compensation loops, can be reduced to a simplified transfer function. The transfer function for an operational amplifier network, for example,



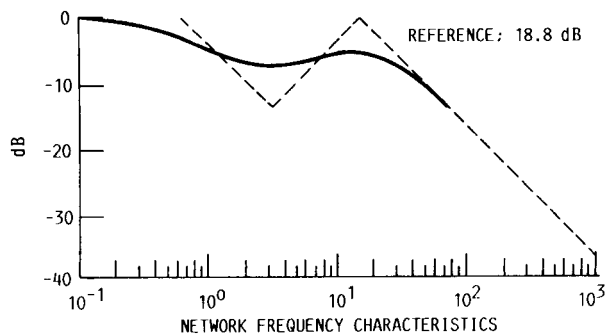
where

$Y_{12A}$  short-circuit transfer admittance of feedback network A

$Y_{12B}$  short-circuit transfer admittance of feedback network B

$Y_{12C}$  short-circuit transfer admittance of input network C

Evaluation of these networks is fairly tedious, complex, and prone to error. Perkin-Elmer utilized its Perkin-Elmer Circuit Analysis Program (PECAP) computer program to obtain the frequency characteristics of the network. The break frequencies obtained from the frequency characteristics were then converted to the system time constants.



The solid line represents the frequency data generated by the computer. The dotted lines represent the asymptotes to the frequency response curve.

When the asymptotes are used, there are 6 break frequencies. The break frequencies are

$f_1'$  lag at 0.6 Hz;  $\tau_1 = 0.265$  sec

$f_2'$  lead at 1.5 Hz;  $\tau_2 = 0.106$  sec

$f_3'$  lead at 5.8 Hz;  $\tau_3 = 0.0275$  sec

$f_4' f_5'$  double lag at 14 Hz;  $\tau_4, \tau_5 = 0.0114$  sec

The dc gain is 8.76. Therefore the overall system transfer function is

$$\frac{e_{out}}{e_{in}} = \frac{(8.76)(1 + 0.106S)(1 + 0.0275S)}{(1 + 0.265S)(1 + 0.0114S)(1 + 0.0114S)} = G(S)_{Block A}$$

The open loop transfer function is then

$$\frac{x}{d^*} = \frac{21(1 + 0.106S)(1 + 0.0275S)}{S(1 + 0.140S)(1 + 50 \times 10^{-6}S)(1 + 0.265S)(1 + 0.0114S)(1 + 0.0114S)(1 + 0.00125S)}$$

where

x input signal; Atlas/Centaur or Titan/Centaur displacement, in.

d penta position or feedback, in.

From the computer runs, the system has adequate stability and meets the requirements providing an adequate solution to the problem of automatic tracking of the Atlas and/or Titan vehicle and converting the AALT theodolite to complex 41 needs.

#### ADDITIONAL DESIGN CONSIDERATIONS

The television vidicon becomes an integral part of the theodolite optical system, and the camera mechanical design imposes constraints on the allowable vidicon location. In addition, the light energy available at the vidicon cathode through the autocollimator optics is sufficiently low to require use of the most sensitive possible vidicon along with a specially coated dichroic beamsplitter.

The vidicon cathode lies directly at the focal plane of the autocollimator objective. Thus in the absence of an intermediate focal plane, the cross-wire reticle pattern required for pointing the autocollimator must be made part of the cathode if it is to be in sharp focus. Vidicons with custom reticle patterns engraved directly on the photoconductive surfaces were obtained on special order from General Electric and were employed successfully.

## Geometrical Characteristics

The TV vidicon, whose 525-line raster size is 1/2 by 3/8 in., is located at the focus of the 30-in.-focal-length autocollimator objective lens. The viewed field size is 5.3 by 7.1 ft at 415 ft and 10.4 by 13.9 ft at 833 ft.

The 1-1/2-in.-platform prism covers 12 lines at 833 ft and 24 lines at 425 ft and will be easily seen on the TV screen (provided illumination inside the vehicle is sufficiently intense). Otherwise, it will still be possible to make initial alignment adjustments from the TV view by centering the reticle on the vehicle window.

## PHOTOMETRY

The light intensity,  $I^*$ , on the vidicon face is given by

$$I^* = \frac{I_0^* K}{4 \left(\frac{f}{no}\right)^2}$$

where

$I_0^*$  source brightness = 1000 lm/ft<sup>2</sup> from a white surface at noon

$\frac{f}{no}$  f-number of objective lens =  $\frac{\text{focal length}}{\text{average diameter}} = \frac{30}{6.7} = 4.5$

$K_g$  = gain reduction factor as follows:

- (1) Three metallic reflections at 0.62 each =  $0.62^3 = 0.24$
- (2) Eight air-glass transmission at 0.96 each =  $0.96^8 = 0.72$
- (3) Visual beamsplitter = 1.00
- (4) TV beamsplitter = 0.35
- (5) Atmospheric transmission = 0.92

$$K = (0.24)(0.72)(1.00)(0.35)(0.92) = 0.055$$

and

$$I^* = \frac{1000 \times 0.055}{4 \times (4.5)^2} = 0.7 \frac{\text{lm}}{\text{ft}^2}$$

Thus a maximum faceplate illumination of 0.7 lm/ft<sup>2</sup> is available at the vidicon. Consequently, there is ample light for a good picture late in the day or under overcast conditions.

APPENDIX C  
 AUTOMATIC AXIMUTH-LAYING THEODOLITE FEASIBILITY STUDY FOR  
 ATLAS/CENTAUR AND TITAN/CENTAUR

Specifications for the servo sway and pointing accuracy requirements follow:

- (1) Maximum time (5 min) - 12-in. peak-to-peak sway at 3/4 Hz once every 24 hr (worst possible case)
- (2) Minimum time (no time duration) - 6-in. peak-to-peak sway at 3/4 Hz

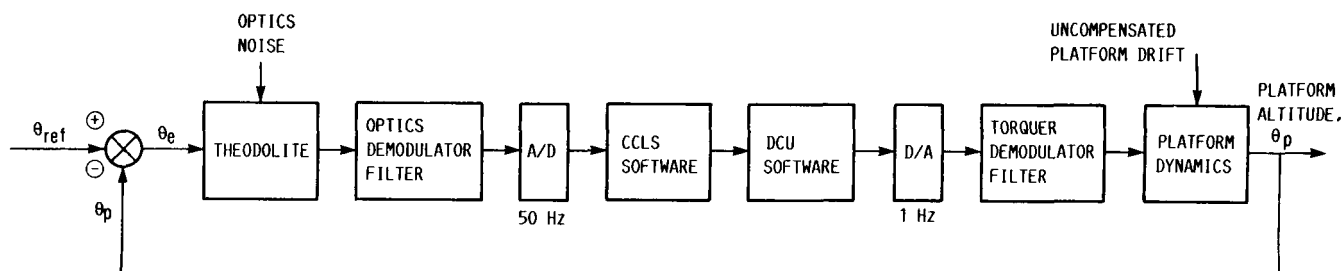
Dynamic analysis of the inertial platform azimuth optical alignment loop for Centaur.

Results of dynamic analysis shows the guidance azimuth alignment loop as planned is stable and well clamped under all conditions analyzed.

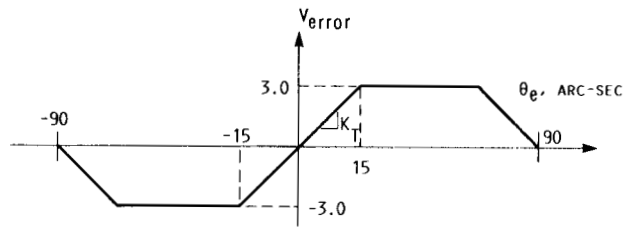
SUMMARY OF RESULTS

- (1) The nominal gain of 1.2 arc-sec/sec/V error can be increased, if desired, to achieve better loop response while retaining a satisfactory stability margin.
- (2) The break frequency of the optics demodulator filter can be reduced by up to an order of magnitude if necessary to further attenuate optics noise, with only minor degradation of loop stability.
- (3) Quantization effects of analog-to-digital (A/D) and digital-to-analog (D/A) converters are insignificant with regard to steady-state limit-cycle attitude error. Because of this effect, the terminal limit cycle is less than the least significant attitude bit, 0.39 arc-sec.
- (4) The steady-state limit-cycle attitude error for the maximum uncompensated platform drift rate (0.32 arc-sec/sec) is approximately 1.5 arc-sec.

This analysis is limited to final alignment: that is, attitude errors of less than  $\pm 15$  arc-sec. Beyond this point, the theodolite output saturates and the system behavior is nonlinear. Likewise optics noise (ground shimmer) or occultation and vehicle bending oscillations are outside the range of this study. The effects of platform drift are considered in the following limit-cycle analysis of the optics loop:



The autotheodolite is used to sense error between the platform azimuth gimbal and the established launch site reference azimuth. The autotheodolite electro-optical system converts the azimuth misalignment in a dc analog error signal. See the following example, in which it is assumed that misalignment is independent of frequency:



### Optics Demodulator/Noise Filter

The filter phase and gain characteristics were determined from manufacturer-supplied data. Data has been approximated by a fifth-order lag. The approximation is good with maximum errors of approximately 10° and 2 dB at the higher frequencies.

### Analog-to-Digital Converter

The function of the analog-to-digital (A/D) converter is to accept the filtered dc error voltage and on command produce a binary number in the computer-controlled launch set (CCLS) input register. The A/D converter has an input range of ±10 V and is an 8-bit (7 bits + sign) converter. The bit value of the least significant bit is  $10 V_{dc}/2^7 = 0.078 V_{dc}$  which is equivalent to an attitude error of 0.39 arc-sec. Note: maximum input signal is only ±3 V<sub>dc</sub> (±15 arc-sec), whereas the A/D input range is ±10 V<sub>dc</sub>.

### CCLS SOFTWARE

CCLS software attitude error signal is input at the rate of 50 Hz. CCLS communicates to the digital computer unit (DCU) at a 1-Hz rate. The CCLS output, for an attitude error less than ±15 arc-sec is given by

$$y_{n-1} = \frac{g_{sys}}{50} (x_{i-50} + x_{i-51} + \dots + x_{i-99})$$

$$y_n = \frac{g_{sys}}{50} (x_i + x_{i-1} + \dots + x_{i-49})$$

where

$y_n$  CCLS output on the  $n^{th}$  cycle (1 Hz)

$g_{sys}$  system gain

$x_i$  error signal input data on the  $i^{th}$  input cycle (50 Hz)

A maximum transport delay between receipt of the  $i^{th}$  input value and output of the  $n^{th}$  command signal has been estimated at 160 msec.

For purposes of analysis, the 50 Hz input signal averaging over 1-sec intervals is approximated by a two-sample averaging process as

$$y_n = \frac{g_{sys}}{2} (x_n + x_{n-1})$$

where it is now assumed that the input error signals  $x_n$  are at a 1-Hz rate.

#### DCU Software

Basic function of the DCU (optics loop) is to accept input commands from the CCLS and output these commands through on the ac D/A converter to the inertial measuring unit (IMU) platform gyro torquer.

Communication between CCLS and DCU can produce a transport delay of 0 to 1.0 sec depending on the phasing between the two computers. If they are not synchronized, an additional DCU delay time of 20 msec will also be present between the DCU input and output. Even though the DCU program contains additional optics-loop logic, it does not influence optics-loop operation under the conditions being analyzed. Thus, DCU software is seen to consist of transport delay only.

#### Digital-to-Analog Converter

The DCU digital-to-analog (D/A) converter is an ac-output device with an output range of  $\pm 3.5 V_{rms}$ . The converter has 12 bits (11 bits + sign) so that the bit value of the least significant bit is  $3.5 V_{rms}/2^{11} = 1.71 \times 10^{-3} V_{rms}$  which is equivalent to 0.034 arc-sec/sec rate command for the nominal loop gain (1.2 arc-sec/V). The maximum commanded rate is 3.6 arc-sec/sec, this represents a D/A output voltage of only 0.18  $V_{rms}$ .

#### Gyro Torquer Demodulator Filter

The gyro torquer demodulator filter transfer function is obtained from the demodulator and output amplifier block diagram along with the given parameter values from Honeywell. This transfer function is a single-order lag with a break frequency of 19.8 Hz ( $\tau = 0.00806$  sec) and unity steady-state gain.

#### Inertial Measurement Platform Dynamics

The transfer function of the inertial measurement unit (IMU) was obtained from Honeywell. The gain represents the gyro torquer scale factor

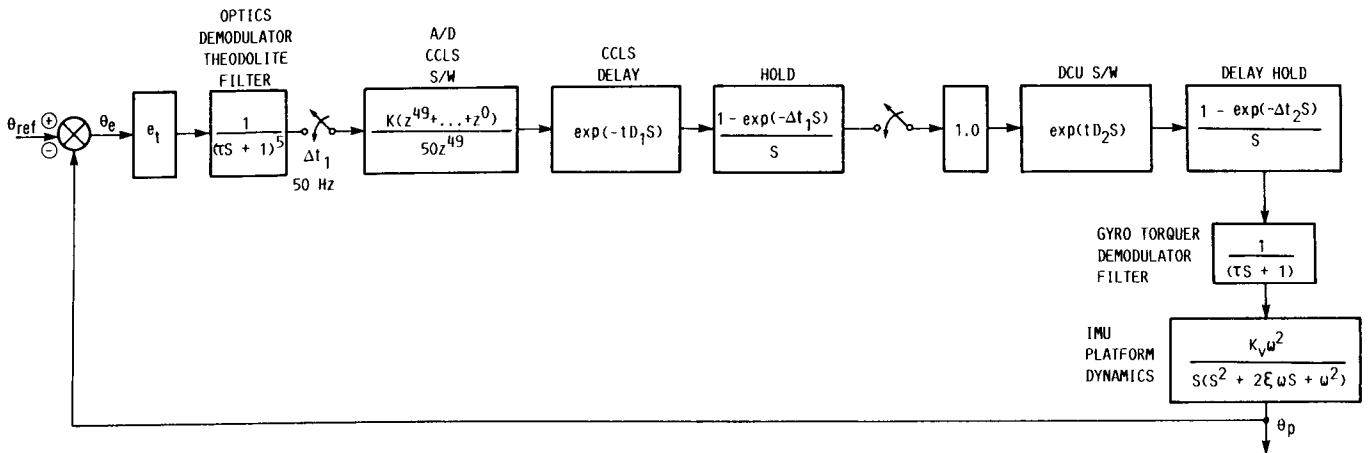
$$\frac{\theta_p}{\theta_{ref}} = \frac{g_v}{s \left[ \frac{s}{\omega^2} + \frac{2}{\omega} (\xi) s + 1 \right]}$$

where

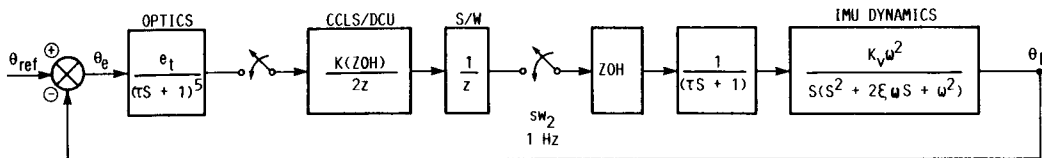
$\omega$  frequency = 255 rad/sec (40.6 Hz)

$\xi$  damping ratio = 0.65

$g_v$  velocity gain = 201/sec.



SIMPLIFIED TO -



### ROOT LOCUS ANALYSIS

Stability of the hybrid loop was analyzed using the state variable approach; that is, stability is assured if the roots of the system state-transition matrix are within the unit circle in the complex plane (using the Z-plane root locus diagrams). Roots outside the unit circle are characterized by divergent oscillations and those inside by decaying oscillations. Loop control frequency and damping ratio are summarized as follows:

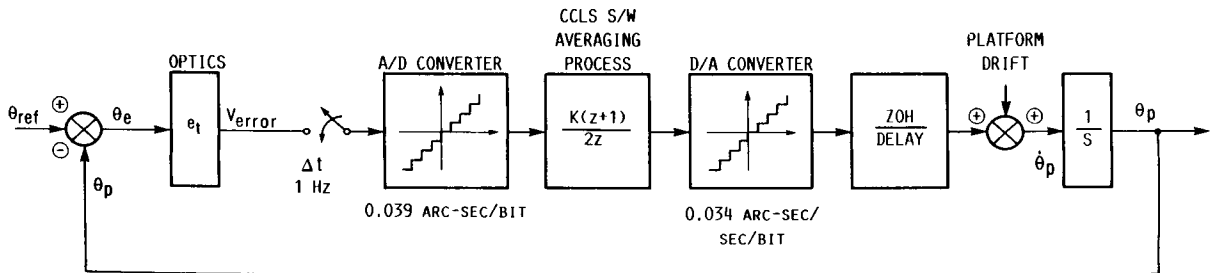
Delay time, sec	Constant gain (K = 1.2 arc-sec/sec/V error)		Constant damping a( $\xi = 0.3$ )		Constant gain (K = 2.4 arc-sec/sec/V error)	
	Control frequency, Hz	Damping	K, arc-sec/sec/V error	Control frequency, Hz	Control frequency, Hz	Damping
0	-----	1.0	5.0	0.18	0.15	0.68
.25	-----	1.0	4.0	.15	.13	.55
.30	0.093	.92	3.0	.12	.12	.43
.75	.086	.82	2.8	.11	.11	.33
1.0	.083	.73	2.2	.10	.10	.27

<sup>a</sup>For reference, the 0.3 damped condition is given as interpolated from the root loci.

Note that at nominal gain (1.2 arc-sec/sec/V error) the system is overdamped for loop delay times of less than 0.5 sec. The data in this table shows that the loop gain is too low to get the best response from the system as planned; it also includes the loop control frequency and damping ratio for the loop gain set at 2.4 arc-sec/sec/V error. This increased gain increases the loop response frequency and at the same time maintains an adequate damping ratio. For the time delay of 1.0 sec, the gain margin is 6 dB at a gain of 2.4 arc-sec/sec/V error.

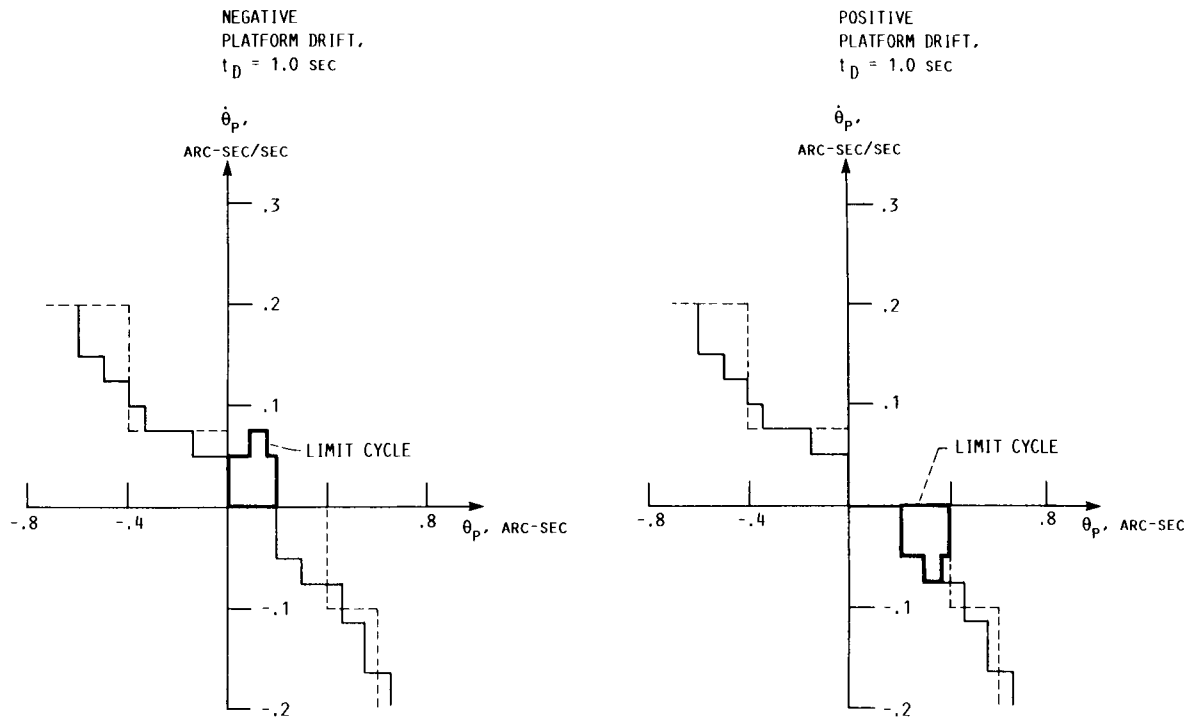
### LIMIT-CYCLE ANALYSIS

Limit cycle analysis is based on



Note that the A/D and D/A converters are quantized. A limit cycle is a self-sustaining oscillatory condition. In general, there are two classes of limit cycles, disturbed and undisturbed. Since the optics loop is a rate command system, the loop will not limit cycle in the absence of a disturbance. Limit cycles will occur in the presence of noise or platform drift.

There are two terminal limit-cycle conditions. For example, see the following phase plane plot showing platform rate and attitude:



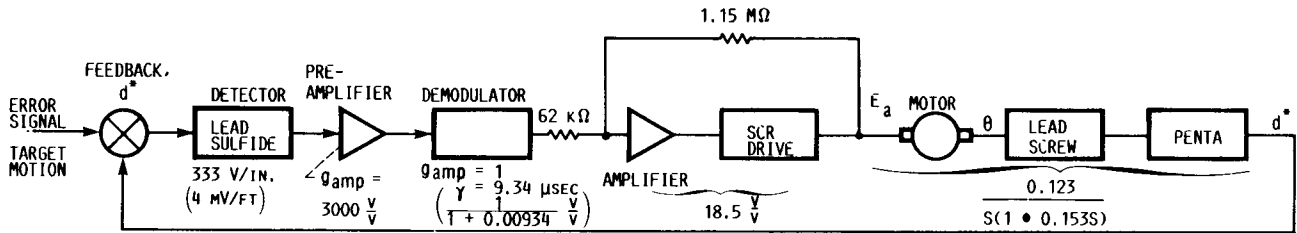
Two cases are depicted: The first condition shows negative platform drift, and the second shows positive platform drift. These limit cycles would occur whether acquisition occurs from the positive or negative directions. In both cases, it is assumed that the platform drift rate is small.

The limit-cycle frequencies are dependent on the magnitude of the drift rate. The frequency increases with an increasing drift rate. The two limit cycles shown assume drift rates of less than 0.102 arc-sec/sec and -0.068 arc-sec/sec. As the drift rates exceed these values, the platform attitude will jump to the second attitude bit level. For the higher drift rates, it will require an increasingly larger steady-state attitude error to bias out the platform drift. For a maximum uncompensated platform drift rate of 0.32 arc-sec/sec (0.32°/hr), the limit-cycle attitude becomes approximately 1.5 arc-sec.

Thus, the limit-cycle analysis shows that the limit cycle resulting from quantization of the attitude error and rate command is insignificant with regard to overall system performance. The limit-cycle attitude perturbation resulting from these effects is less than the least significant A/D bit (0.39 arc-sec). This value will increase with an increase in loop gain. However, the limit cycle would remain below the 1-bit level even with a gain increase of a factor of two. The steady-state attitude error will also increase as the platform drift rate increases.

APPENDIX D  
ENGINEERING NOTES  
SYSTEM RESPONSE (OPEN LOOP)

The original system without compensation:



$$\text{Motor} = \frac{\theta}{E_a} \frac{\frac{1}{K_B}}{\left( \frac{S(1 + J_T S)(1 + \tau_{elec} S)}{\frac{K_B K_T}{R_T} + F_B} \right)} \quad (D1)$$

where

$$\tau_{elec} = 50 \mu\text{sec} \quad (\text{negligible})$$

$$\frac{K_B K_T}{R_{tot}} = \frac{0.108 \frac{\text{V}}{\text{sec}} \left( 0.080 \frac{\text{ft-lb}}{\text{amp}} \right)}{2R} = (0.108)(0.040) = 4.32 \times 10^{-3} \frac{\text{ft-lb}}{\text{rad/sec}}$$

$$F_B = 1.94 \times 10^{-3} \frac{\text{ft-lb}}{\text{rad/sec}}$$

$$\tau_{mech} = \frac{J_T}{(4.32 + 1.94) \times 10^{-3}} = \frac{0.96 \times 10^{-3}}{6.26 \times 10^{-3}} = 0.153 \text{ sec}$$

$$\omega_B = \frac{1}{\tau_{mech}} = \frac{1}{0.153} = 6.52 \text{ rad/sec}$$

Thus,

$$F_B = \frac{6.52}{6.28} = 1.04 \text{ Hz}$$

Hence,

$$\frac{\theta}{E_a} = \frac{\frac{1}{0.108}}{S(1 + 0.153S)(1 + \tau_{elec}S)} = \frac{9.26}{S(1 + 0.153S)}$$

Drop the  $\tau_{elec}$  term since it is 50  $\mu$ sec; thus,

$$F_B \approx 3000 \text{ Hz}$$

Convert to linear displacement  $d^*$ :

$$\frac{24\pi d^*}{E_a} = \frac{9.26}{S(1 + 0.153S)}$$

or

$$\frac{d^*}{E_a} = \frac{\frac{9.26}{75.4}}{S(1 + 0.153S)} = \frac{0.123}{S(1 + 0.153S)}$$

#### SYSTEM RESPONSE WITH COMPENSATION

$$\begin{aligned} \frac{d^*}{x} &= \left( \text{Detector} \right) \left( \text{Preamplifier} \right) \left( \text{Demodulator} \right) \left( \text{Amplifier} \right) \left( \text{Motor/lead screw} \right) \\ &= \left( 4 \frac{\text{mV}}{\text{ft}} \right) \left( 3000 \frac{\text{V}}{\text{V}} \right) \left( \frac{1}{1 + 0.00934S} \frac{\text{V}}{\text{V}} \right) \left( 18.5 \frac{\text{V}}{\text{V}} \right) \left( \frac{0.123}{S(1 + 0.153S)} \right) \\ &= \left( \frac{25}{S(1 + 0.153S)(1 + 9.34 \times 10^{-3}S)} \right) \left( \frac{1}{9.34 \times 10^{-3}} \right) = 107 \text{ rad} \quad (D2) \end{aligned}$$

#### MOTOR LIMITATIONS

Two limitations were noted with this motor:

(1) Torque-power limitation

(2) Heat limitation (This limitation was determined by rms current, not dc current, since the system uses SCR drive.)

Motors are equivalent to PMI 668 (at time of this writing, a discontinued device). A close equivalent would be U16M4.

The motor characteristics are

- (1) Higher voltage (60 V compared with 36 V for the PMI 668 motor)
- (2) Higher armature resistance (0.79  $\Omega$  compared with 0.4  $\Omega$ )
- (3) Lower current capability

Because of a lack of more definitive information, the thermal characteristics were assumed to be equivalent. Conversations with Perkin-Elmer photocircuit application engineers indicate that the ratings for the U16M4 will be conservative because a different magnet structure was used than on PMI 668. It should be capable of dissipating more power than PMI 668.

Data for U16M4 motor:

- (1) Thermal resistance (uncooled)
- (2) Armature to case,  $\theta_{a-c} = 0.80 \text{ }^\circ\text{C/W}$
- (3) Case to ambient with aluminum heat sink of 196 in.<sup>2</sup> (0.375 in. thick),  $\theta_{c-a} = 0.55 \text{ }^\circ\text{C/W}$

The maximum armature disposition for PMI 668 was power input/rated power output.

#### THERMAL LIMITATIONS

The PMI 668 motor on a 14 by 14 by 0.375 in. aluminum heat sink was capable of

$$V_{dc}I_{dc} - \text{rated power output} = (36)(10) - 249 = 111 \text{ W}$$

The U16M4 is capable of a 93-W output, so using the U16M4 data was considered to be conservative:

$$p_{\max} = \frac{150 \text{ }^\circ\text{C} - \text{Temp (}^\circ\text{C)}}{\theta_{a-c} + \theta_{c-a}} = \frac{150 \text{ }^\circ\text{C} - 25 \text{ }^\circ\text{C}}{0.80 \text{ }^\circ\text{C/W} + 0.55 \text{ }^\circ\text{C/W}}$$

$$p_{\max} = \frac{125 \text{ }^\circ\text{C}}{1.35 \text{ }^\circ\text{C/W}} = 93 \text{ W}$$

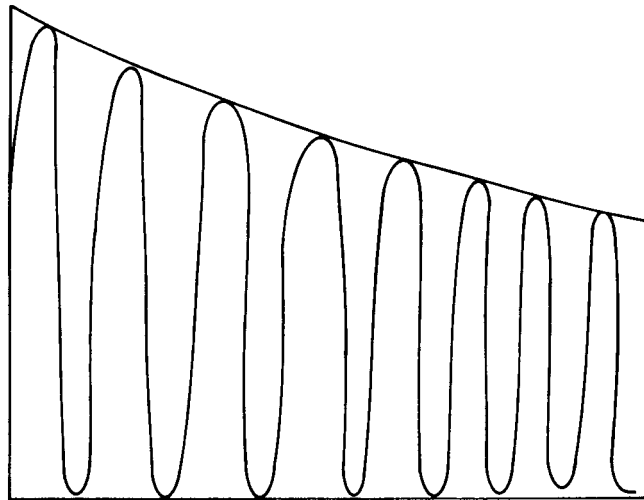
The motor plate on the theodolite measures

$$(14.38 \text{ in.} \times 11.76 \text{ in.}) - \frac{\pi}{4}(6.13)^2 = 139.6 \approx 140 \text{ in.}^2$$

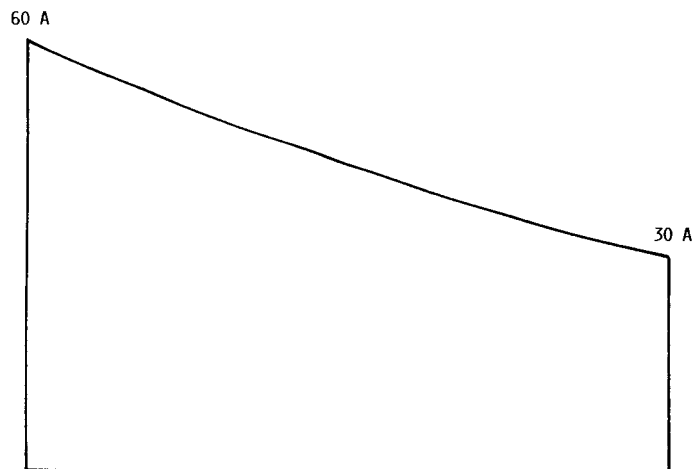
The plate is also 0.75 in. thick, which should help.

Motor current waveforms were used at 1.0 Hz and 10 in. peak-to-peak displacement. The 400-Hz current peaks approximate a triangular waveform envelope superimposed on a rectangle.

Representation of wave shapes:



Idealizing the waveform to



The average current peak is then  $30 + 15 = 45$  A peak. Using this for the rms determination yields an rms value of

$$(0.707)(45.0) = 31.82 \text{ A}$$

The armature dissipation is  $I_a^2 R_a (R_a = 0.47) = (31.8)(0.5) \approx 505.6$  W.

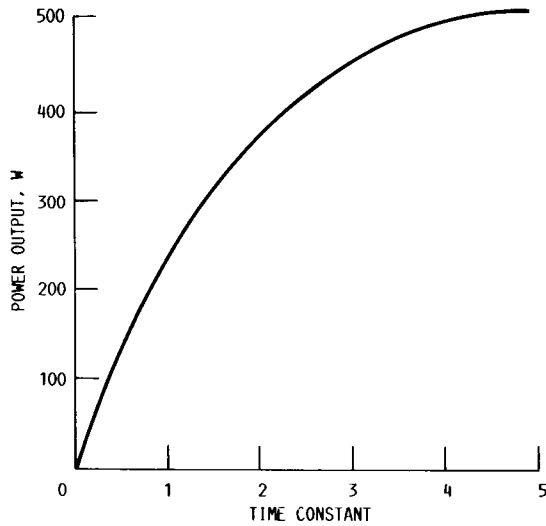
The motor dissipation is then approximately 500 W, whereas maximum continuous dissipation is about 100 W. It is questionable if the motor can handle the required displacement of 12 in. peak to peak at 0.75 Hz.

For the 016M4 motor, the thermal time constants are

(1) Armature to case  $\tau_{a-c}^* = 70$  sec (1.16 min)

(2) Case to ambient  $\tau_{c-a}^* = 3800$  sec (63.33 min)

These values apply to a motor without heat sink.



The 100-W level rises very quickly, and it represents the 20-percent level. Then,

$$100 = 500 \left[ 1 - \epsilon^{\left( \frac{-\tau^*_{a-c}}{\tau_{c-a}} \right)} \right]$$

$$0.2 - 1 = -\epsilon^{\left( \frac{-\tau^*_{a-c}}{\tau_{c-a}} \right)}$$

$$0.8 = \epsilon^{\left( \frac{-\tau^*_{a-c}}{\tau_{c-a}} \right)}$$

$$\ln 0.8 = \frac{-\tau^*_{a-c}}{\tau_{c-a}} \quad \text{or} \quad -0.233 = \frac{\tau}{3800} = \tau^*_{a-c} = 847.6 \text{ sec}$$

#### AMPLIFIER POWER LIMITATIONS

Limitations on the motor silicon-controlled rectifier (SCR) amplifier are

(1) The transformer is rated for 300 V-A  $\approx$  300 W with a 50-percent duty cycle, (i.e., 30 sec on, 30 sec off).

(2) No thermal data exist for transformer except that the manufacturer estimates the thermal time constant to be 3 to 5 min.

(3) The 300-V-A capability represents primarily a flux-carrying capability and not so much a thermal limitation.

(4) The SCR (2N683) can easily carry the level of current with the heat sinking employed.

(5) The SCR, 2N683, has a peak forward surge of 200 A. The system pulls 70-A peak at 400 Hz: peak rating is not exceeded. There are four SCR's - two for the forward direction, two for the reverse direction. Therefore, the two forward SCR's see only a 50-percent duty cycle (the same situation as for the reverse SCR's). Additionally, the two SCR's are wired in a full-wave configuration and, therefore, only carry one-half the current load. The average current flow for the 2N683 at 180° conduction angle using the 45-A peak average calculated previously is 0.637 of peak:

$$I_{avg} = (45)(0.637) = 28.7 \text{ A}$$

But each SCR only carries half the load or 14.35 A. Vendor-supplied graph data are used: 180° conduction, 15 A, and a standard temperature of 125 °C - yielding an average power of 22 W.

The suggested plate size for the heat sink (14 A average forward current) is a 6 by 6 by 0.125 in. copper plate with a 0.75 in. space between adjacent SCR's at 20 °C ambient temperature.

Theodolite SCR's are mounted to an aluminum plate 0.125 in. thick which also houses other components (e.g., transformer, radiofrequency interference (RFI) filter, SCR gate drives). The SCR gate drives do not dissipate any appreciable amount of heat as a "concern" item. The transformer is the unit that dissipates the most heat.

The 2N683 with a 0.003-in. mica insulator and shear grease has a thermal impedance of = 3.1 °C/W (vendor data). The plate to which the SCR's are mounted has a surface area of 105 in.<sup>2</sup> (one side). This is not completely usable since the components previously mentioned are also on it. The surface areas of the larger devices are

- (1) SCR gate drives, two at 3.375 by 2.25 in.  $\approx 8.86 \text{ in.}^2 = 17.72 \text{ in.}^2$
- (2) Transformer and RFI filter = 9 in.<sup>2</sup>
- (3) Other elements = 10 in.<sup>2</sup>

The total usable area (one side) = 105 in.<sup>2</sup> - 37 in.<sup>2</sup> = 68 in.<sup>2</sup> or 65 in.<sup>2</sup> by 0.125 in. of aluminum. This is very conservative.

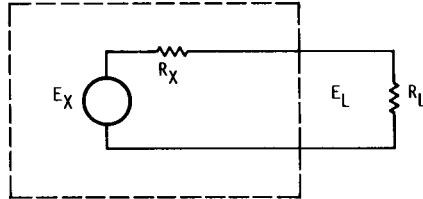
Transformer data from the vendor follows:

- (1) The unit on the sway chassis can stand 300 V-A continuously.
- (2) The thermal time constant is approximately 30 min.
- (3) The total power losses at full power including core and copper losses are about 13 to 15 W.

Thus, the limitation is thermal on the 300-V-A transformer - not flux capability.

## OUTPUT IMPEDANCE OF MOTOR AMPLIFIER

The amplifier was loaded down with resistive loads. Thus, the penta unit was displaced 1.5 in. to give full-power output.



$R_L$ $\Omega$	$E_L$ $\Omega$
2.0	20.0
4.0	21.0
6.0	21.5
9.0	22.0

$$E_{L1} = \frac{R_{L1}}{R_{L1} + R_X} E_X$$

Also,

$$E_{L2} = \frac{R_{L2}}{R_{L2} + R_X} E_X$$

Thus

$$E_X = \frac{R_{L1} + R_X}{R_{L1}} E_{L1} = \frac{R_{L2} + R_X}{R_{L2}} E_{L2}$$

or

$$\frac{E_{L1} - E_{L2}}{\left(\frac{E_{L2}}{R_{L2}} - \frac{E_{L1}}{R_{L1}}\right)}$$

or

$$R_{X,avg} = 0.31 \Omega$$

## ESTIMATED OUTPUT IMPEDANCE ON SERVO

The total resistance in the armature circuit will be affected by the amplifier output impedance. The value of  $0.31 \Omega$  is much lower than that expected ( $1.4 \Omega$ ). The new total  $R_{tot}$  will then be

$$R_{tot} = R_a + R_m = 0.31 + 0.57 = 0.88 \approx 0.9 \Omega$$

The motor frictional term  $\frac{K_B K_r}{R_{tot}}$  was based on an  $R_{tot}$  of  $2 \Omega$ .

This now becomes

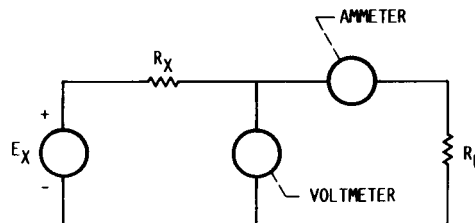
$$\frac{K_B K_r}{R_{tot}} = \frac{(0.108)(0.080)}{0.9} = \frac{8.64 \times 10^{-3}}{0.9} = 9.6 \times 10^{-3} \frac{\text{ft-lb}}{\text{rad/sec}}$$

$\tau_{mech}$  now becomes

$$\frac{J_T}{F_T} = \frac{0.96 \times 10^{-3}}{9.60 + 1.94} = \frac{0.96 \times 10^{-3}}{11.54 \times 10^{-3}}$$

$$\tau_{mech} = 0.083 \text{ sec or } 1/\tau_{mech} = 12.05 \text{ rad}$$

This is about double the original computed break frequency (0.153 sec at 6.5 rads). (It is recommended that a recheck of amplifier output impedance be made).



Results on the previous test may be in error since  $R_L$ , when rechecked, was high by  $0.4 \Omega$  in each case.

Direct current, I, A	Voltage, V <sub>dc</sub>	Load resistance R <sub>L</sub> , $\Omega$
0	23.68	$\infty$
.055	22.58	$\approx 390$
.105	22.58	$\approx 200$
.215	22.52	$\approx 100$
2.4	22.04	
2.8	21.95	
3.6	21.80	
4.15	21.60	
5.2	21.45	
6.55	21.16	
8.2	20.85	
9.4	20.60	

The open circuit voltage of 23.50 V appears to be high relative to what would be expected for a load of 55 and 105 mA. The current drain represented by these loads should not cause the output voltage to drop by more than 0.1 V, much less almost 1 V. However, the 23.68 V reading was repeated many times, so it was not a fluke. Using an  $E_{OC}$  of 23.50 yields

$$R_X = \frac{E_X - E_L}{I_L} = \frac{23.68 - 20.60}{9.4} = \frac{3.08}{9.4} \approx 0.32 \Omega$$

Using  $E_{OC}$  of 22.58 (as being more representative) yields

$$R_X = \frac{22.58 - 20.60}{9.4} \approx \frac{2.0}{9.4} = 0.21 \Omega$$

$$R_X = \frac{22.58 - 21.68}{4.15} = \frac{0.90}{4.15} = 0.22 \Omega \text{ (second check)}$$

$$R_X = \frac{22.58 - 21.95}{2.8} = \frac{0.63}{2.8} = 0.22 \Omega \text{ (third check)}$$

The original AGC detector was replaced with a new detector supplied by Sandus Associates:

Resistance of old detector  $\approx 150 \text{ k}\Omega$   
 Resistance of new detector  $\approx 900 \text{ k}\Omega$

$$\frac{900}{150} = \text{a factor of } 6$$

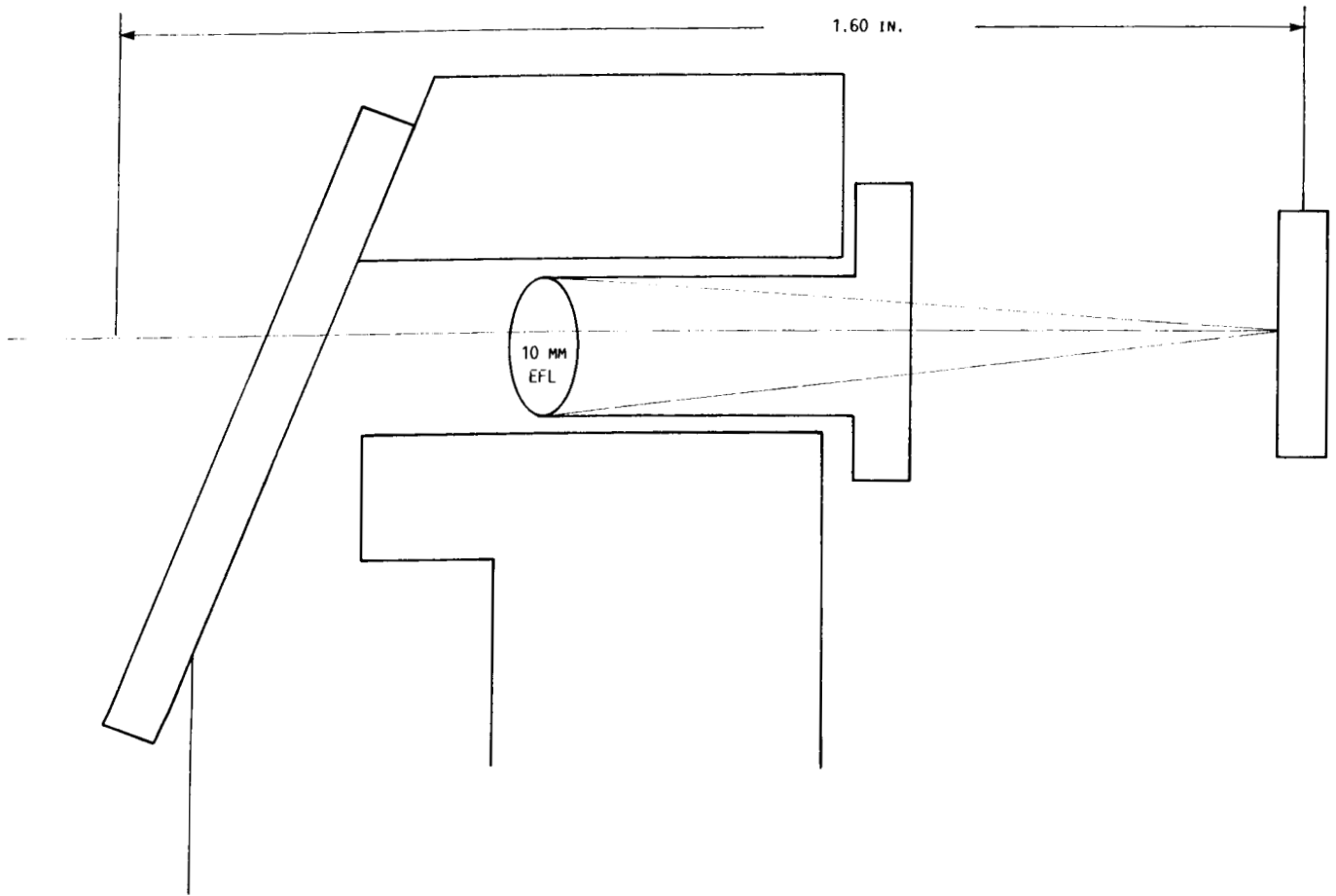
At 345 ft, after warmup the maximum output of the old Porro prism was approximately 2.45 V. At 345 ft, after warmup the maximum output of the new Porro prism was approximately 8 V.

$$\frac{8}{2.45} \approx \text{a factor of } 3$$

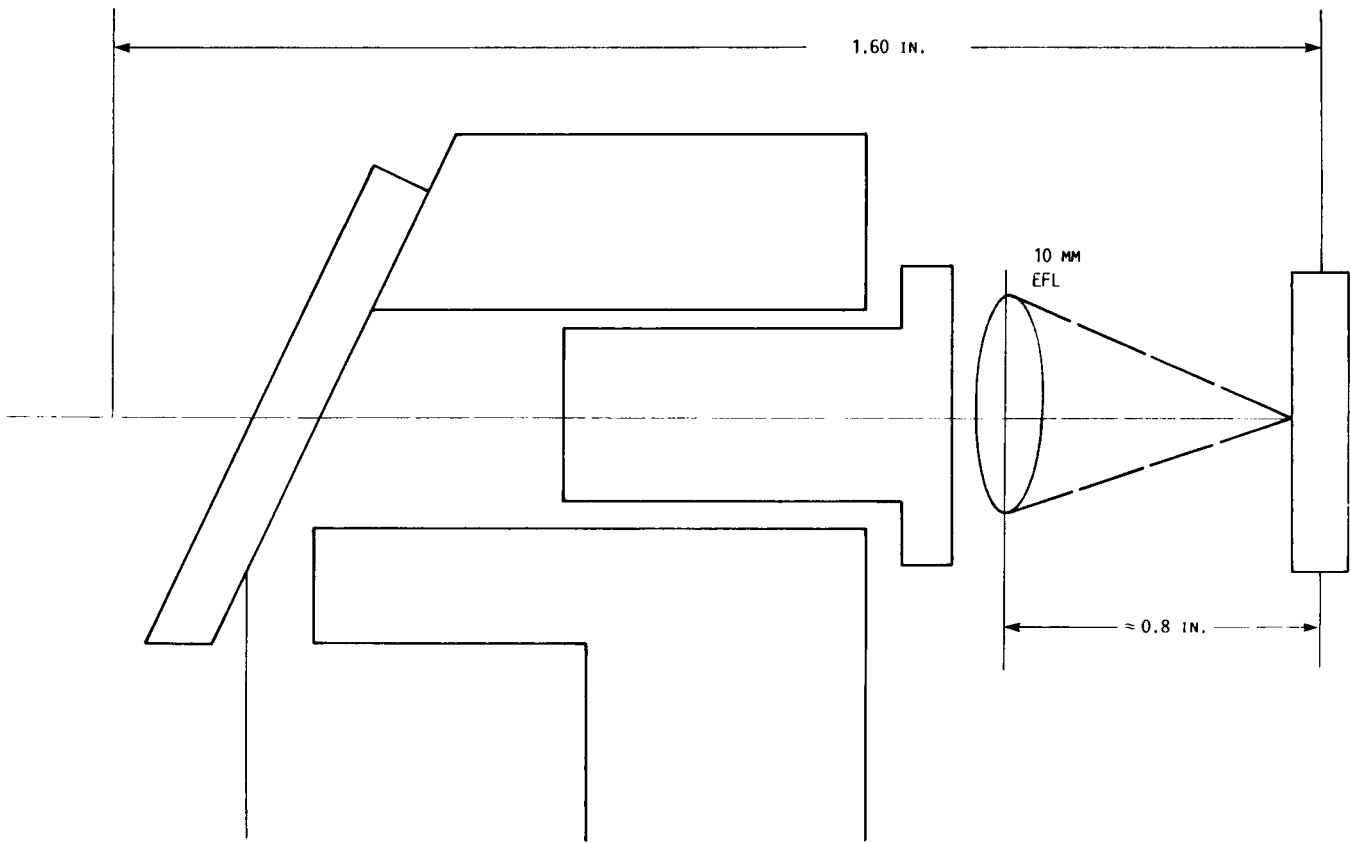
Setting the acquisition amplifier to stay on with a 5:1 change in gain level makes it marginal since, when it picks up the opposite phase ( $\pm 75$  arc-sec beyond null), the system would still keep the acquisition light on. This phenomenon was due to the operational amplifier phase shifting when overdriven - setting the gain too high for the low condition (i.e., low end of the 5:1 range). Putting in the full signal (high end of 5:1 range) causes saturation and phase shift so that negative phase changes end up looking positive (fig. 2).

A fix for this problem, (preventing the operational amplifier from saturating with overdrive), was accomplished by inserting two Zener limiting (1N752) devices across the feedback resistor.

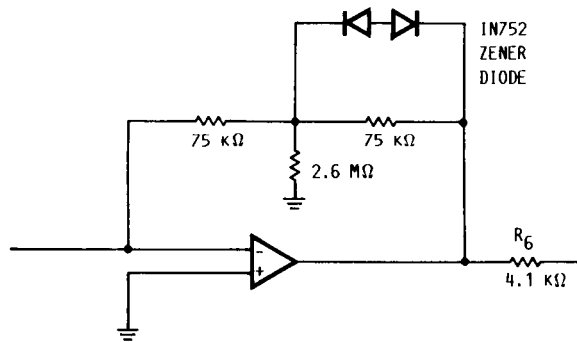
The following sketch shows the 10-mm effective focal length (EFL) double convex lens as it was installed in the sway area (magnification,  $\sim \times 2$ )



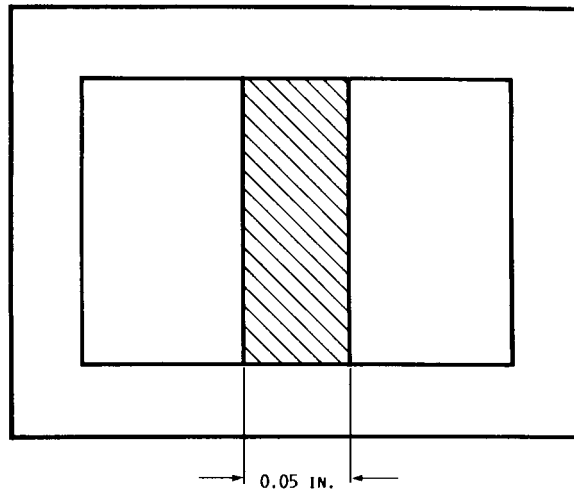
The next sketch shows the 10-mm EFL lens (magnification, 1:1) mounted on the end of the cell:



The 8.2-k $\Omega$  compensating resistor  $R_6$  was reduced to 4.1 k $\Omega$  since the function of this resistor was to reduce the amount of saturation. With Zeners it can be low in value.



The installed AQGC detector is shown with the center mashed down, in the AQGQ position but tied to the AMGC circuit.



Thus using the  $\times 2.5$  lens as designed took translation and rotation data at center,  $\pm 0.5$  in. and  $\pm 1$  in.

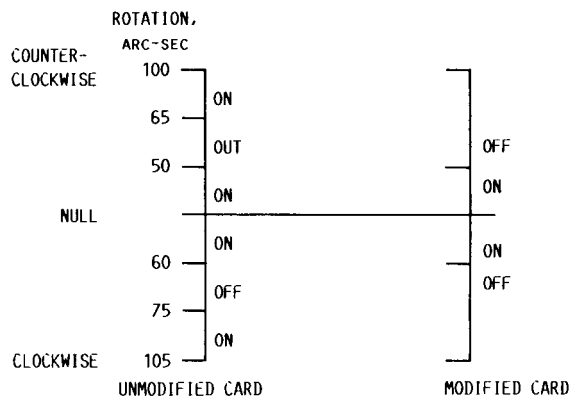
The unit looked good in both translation and rotation:

$\approx \pm 5$  percent for  $\pm 15$  arc-sec rotation  
 $\approx 15$  percent for  $\pm 1$  in. translation

Tests were performed on the acquisition amplifier card (unmodified):

- (1) The prism was masked to a 0.2-in.-wide aperture (1/5 of 1 in.) 5:1 AQC range.
- (2) The gain was adjusted until the acquisition light remained on. (It went out when the aperture was blocked.)
- (3) The prism was rotated  $\pm 50$  arc-secs before the light went out.
- (4) The prism translated  $\pm 2$  in. before the light went out.

The rotation with mask removed from the detector is shown in the following sketch:



The demodulator-amplifier scale factor check is shown in this table:

Displacement, in.	Demodulation, $V_{dc}$	Amplifier output, $V_{dc}$
0	0	0
.25	.25	4.5
.50	.52	9.0
.75	.77	14.0
1	1.00	17.0
1.5	1.15	18.5
2	1.10	17.5
3	.38	7.0

- (1) The AGC was inoperative.
- (2) The dc volts were taken with a vacuum tube voltmeter.
- (3) The amplifier load was a lamp bank drawing 6 A.

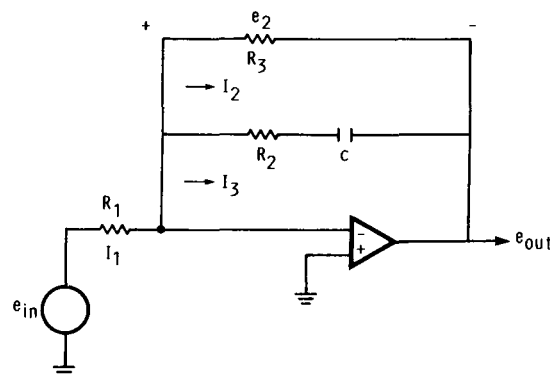
If an allowance is made for the lamp loading, the output impedance of this amplifier checks fairly well with The amplifier/SCR-driver scale factor discussed previously.

#### SWAY RESPONSE (NOISE COMPENSATION)

The sway servo system indicated that a large lag existed. The resistor-capacitor network around the operational amplifier is suspect. The operation amplifier is connected to the common emitters of the transistors which drive the SCR gate controls. The primary purpose of the RC network was to control the effect of internal noise in the system.

Removing the capacitor and leaving the network open resulted in the penta unit jittering randomly over a small amplitude (less than  $\approx 0.125$  in.); no discernible frequency components were present, but jitter was rather rapid.

The system configuration looks like this:



$$I_1 = \frac{e_{in}}{R_1} \quad I_2 + I_3 = I_1$$

$$e_2 = -e_{out}$$

$$\frac{e_2}{R_3} + \frac{e_2}{R_2 + \frac{1}{Sc}} = I_1 = \frac{e_{in}}{R_1}$$

$$\frac{e_{out}}{R_3} + \frac{e_{out}}{R_2 + \frac{1}{Sc}} = I_1 = \frac{e_{in}}{R_1}$$

$$\frac{R_1}{R_3} + \frac{R_1}{R_2 + \frac{1}{Sc}} = \frac{e_{in}}{e_{out}} = \frac{R_1}{R_3} + \frac{SCR_1}{SCR_2 + 1}$$

Then

$$\frac{-e_{out}}{e_{in}} = \frac{(SCR_2 + 1)R_1 + SCR_1 R_3}{(SCR_2 + 1)R_3} = \frac{SCR_2 R_1 + SCR_1 R_3 + R_1}{SCR_2 R_3 + R_3}$$

$$\frac{-e_{out}}{E_{in}} = \frac{SCR_2 R_3 + R_3}{SCR_1 (R_2 + R_3) + R_1}$$

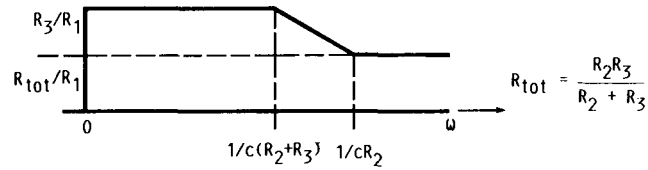
This has the form of

$$\frac{SA + B}{SD + C} = \frac{B \left( S \frac{A}{B} + 1 \right)}{C \left( S \frac{D}{C} + 1 \right)}$$

Thus,

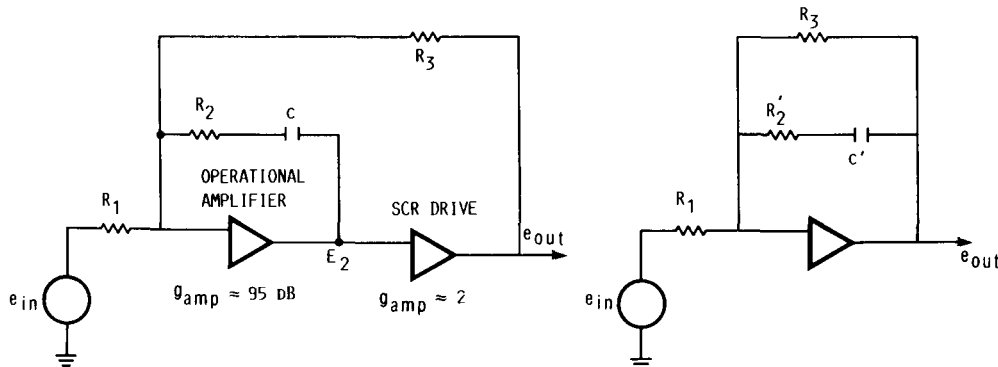
$$\frac{\left( g_{amp} \frac{R_3}{R_1} \right) \left( \frac{SCR_2 R_3}{R_3} + 1 \right)}{\left[ \frac{SCR_1 (R_2 + R_3) + R_1}{R_1} \right]} = \frac{R_3}{R_1} \frac{SCR_2 + 1}{Sc(R_2 + R_3) + 1}$$

The  $R_3/R_1$  term is the dc gain term in a system of 18.5 V/V,



In this system a capacitor of 0.0033  $\mu\text{F}$  provided adequate internal noise suppression and did not require the original design use of 0.033  $\mu\text{F}$ . (See sway servo assembly schematic on p. 87.)

Note that the system depicted on page 83 is not exactly the actual servo drive (operational amplifier drive). The SCR drive with a gain of 2.25 is between the operational amplifier output and the  $R_3$  feedback resistor;



$$R_2' = 2R_2 \quad \text{and} \quad c' = \frac{c}{2}$$

The internal loop frequency response is not affected by the external amplifier (as expected), but the overall feedback loop including the outer loop, is (in terms of the original  $c$  and  $R$ ) as follows:

$$\frac{e_{out}}{e_{in}} = \frac{R_3}{R_1} \frac{SCR_2 + 1}{\left[ \frac{Sc(R_2 + R_3)}{2} + 1 \right]}$$

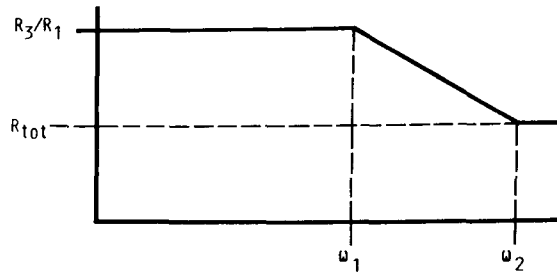
$$R_{tot} = \frac{R_2 R_3}{R_2 + \frac{R_3}{2}}$$

$$\tau_1 = 0.0050$$

$$\tau_2 = 0.0022$$

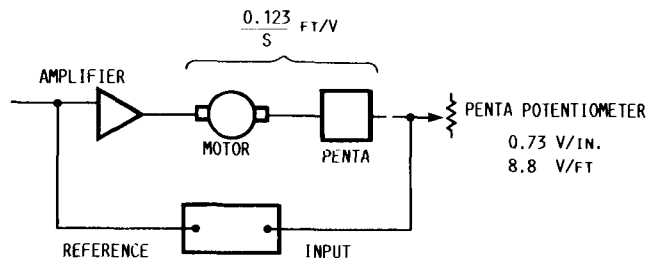
$$f'_1 = \frac{1}{cR_2 + \frac{R_3}{2}}$$

$$f'_2 = \frac{1}{cR_2}$$



The system gain is

$$\frac{e_{out}}{e_{in}} = 18.5 \frac{V}{V} \left( \frac{0.123 \text{ ft}}{S} \frac{8.8 \text{ V}}{\text{ft}} \right) = \frac{20}{S}$$



For  $f' = 0.1$  and  $\omega = 0.628$ ,

$$\frac{20}{0.628} = 31.84 \approx 30 \text{ dB}$$

The results on page 88 give 26.5 dB for  $f' = 0.1$  Hz. This is a difference of 3.5 dB, a factor of (1.5) time. System gain is then

$$26.5 \text{ dB} = 21.13$$

$$(21.13)(0.628) = 14.27 \approx 14$$

$$e_{out}/e_{in} = 14/S$$

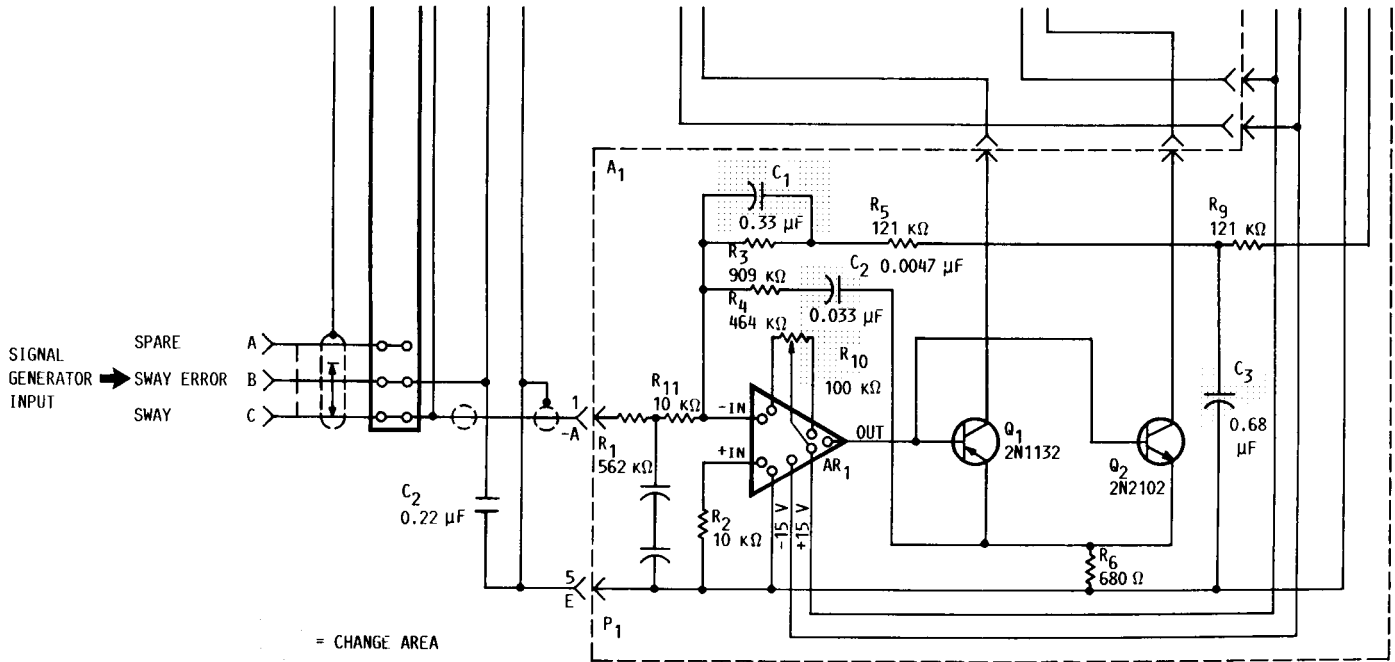
not 20 as computed.

Since the potentiometer scale factor was measured, the error must be in the amplifier-motor scale factor. The system scale factor as measured is approximately 70 percent of the completed value:

$$\frac{14}{20} = 0.70 = 70 \text{ percent}$$

### Dead Zone (Null Vicinity)

The suitability of introducing dead zone around null to reduce shimmer effect was checked. Tests were run on the sway simulator dead zone by introducing (adding) a parallel feedback resistor to the input of the operational amplifier. This resistor (20 MΩ) gives an operational amplifier gain of 2000 instead of the normal open-loop gain ( $g_{amp} > 90 \text{ dB}$ ). The dead zone is provided since the base emitter junction drop of transistors  $Q_1$  and  $Q_2$  must be exceeded. (See the following sketch.) The input signal for the tests was  $> 0.25 \text{ MV}$ .



The following table shows data for the open-loop penta:

Frequency, f, Hz	Amplitude error, dB	Phase $\phi$ , deg	Reference input, $V_{rms}$	Signal generator, $V_{rms}$	Actual amplitude, dB	Corrected amplitude, <sup>a</sup> dB	Actual amplitude - error correction, dB
0.2	-1.3	94	1.0	0.100	20	18.7	18.7
.4	-7.5	100	0	-----	20	12.5	<sup>b</sup> 13.0
.6	-1.3	103	.300	-----	9.5	8.2	<sup>b</sup> 8.7
.7	-2.0	109	0	-----	-----	7.5	<sup>b</sup> 8.2
.8	-3.9	110	-----	-----	-----	5.6	<sup>b</sup> 6.1
.9	-4.8	112	-----	-----	-----	4.7	<sup>b</sup> 5.2
1.0	-6.2	112	-----	-----	-----	3.3	<sup>b</sup> 3.8
1.2	-7.8	116	-----	-----	-----	1.7	<sup>b</sup> 2.2
1.4	-9.2	120	-----	-----	-----	.3	<sup>b</sup> 6.8
1.6	- .5	125	.100	-----	0	- .5	- .5
1.8	-1.8	127	0	-----	-----	-1.8	-1.8
2.0	-3.0	130	-----	-----	-----	3.0	-3.0
2.5	-5.2	141	-----	-----	-----	-5.2	-5.2
3.0	-7.5	150	-----	-----	-----	-7.5	-7.5
4.0	-11.5	160	-----	-----	-----	-11.5	-11.5
6.4	-16	180	-----	-----	-----	-16.0	-----

<sup>a</sup>Actual amplitude minus amplitude error.

<sup>b</sup>plus an additional error of 0.5 dB that was not compensated for.

The reference input is a signal from the penta potentiometer. The signal generator output was fed into the input of the sway servo as indicated on the sway servo assembly schematic (appendix D, p. 87).

The following table shows a rerun of the penta open-loop response. The data were rerun because the original data did not measure up to computation. This run was better but the data were still off.

Frequency, f, Hz	Meter amplitude, dB	Phase, $\phi$ , deg	Input signal, $V_{rms}$	Reference input, $V_{rms}$	Actual amplitude, dB	First run amplitude, dB	Average amplitude, dB	Average angle, $\phi$ , deg
0.05	7.5	92	10.0	0.100	40 - 7.5 = 32.5	-----	3.5	92
.1	3.5	92	3.0	-----	30 - 3.5 = 26.5	-----	26.5	92
.2	9.6	95	3.0	-----	30 - 9.6 = 20.4	18.7	19.6	94
.4	5.8	99	1.0	-----	20 - 5.8 = 14.2	13.0	13.6	100
.6	9.2	104	---	-----	20 - 9.2 = 10.8	8.7	9.8	104
.7	10.5	109	---	-----	20 - 10.5 = 9.5	8.2	8.8	109
.8	11.8	110	---	-----	20 - 11.8 = 8.2	6.1	7.2	110
.9	12.8	112	---	-----	20 - 12.8 = 7.2	5.2	6.2	112
1.0	3.8	116	.300	-----	10 - 3.8 = 6.2	3.8	5.0	114
1.2	6.5	114	---	-----	10 - 6.5 = 3.5	2.2	2.8	115
1.4	7.3	124	---	-----	10 - 7.5 = 2.5	.8	1.6	122
1.6	9.2	127	---	-----	10 - 9.2 = .8	.5	.1	126
1.8	10.0	135	---	-----	10 - 10 = 0	-1.8	-.9	131
2.0	11.0	145	---	-----	10 - 11 = -1.0	-3.0	-2.0	138
2.5	13.5	145	---	-----	10 - 13.5 = -3.5	-5.2	-4.4	143
3.0	15.5	150	---	-----	10 - 15.5 = -5.5	-7.5	-6.5	150
3.5	8.2	157	.100	-----	0 - 8.2 = -8.2	---	-8.2	157
4.0	9.5	164	.100	-----	0 - 9.5 = -9.5	-11.5	-10.5	162
2.5	1.2	145	0.300	0.316	0 - 1.2 = -1.2	---	---	---
3.0	3.6	154	---	---	0 - 3.6 = -3.6	---	---	---
3.5	6.0	158	---	---	0 - 6.0 = -6.0	---	---	---
4.0	7.9	165	---	---	0 - 7.9 = -7.9	---	---	---
---	---	---	---	---	0 - 14 = -14	-16 at 6.9	-15	---
6.0	10-14	180	---	---	-----	-----	---	---

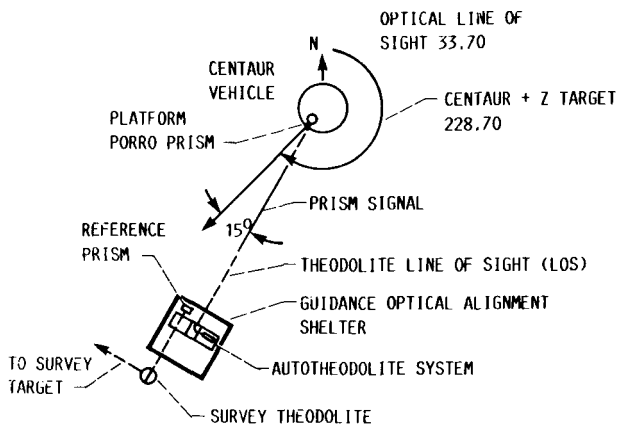
#### BIBLIOGRAPHY

Crusselle, G.M.: D-1 Centaur Unified Test Plan. General Dynamics, GDC-BNZ69-007, Rev. A, 1984.

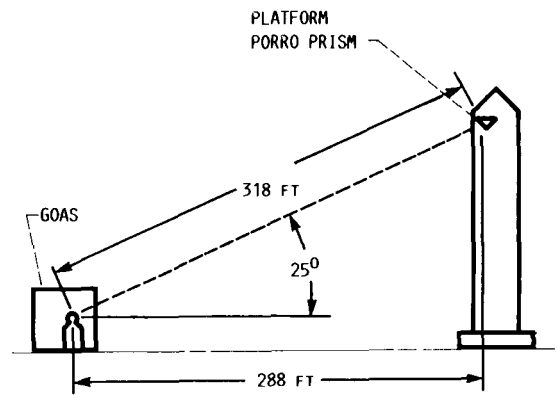
D-1A Atlas Centaur Interface Requirements Documents. General Dynamics, ICT 02-21, 1974.

Detail Specification for Product Configuration and Acceptance Test Requirements for Centaur Vehicle and Mission-Peculiar Components. General Dynamics, Specification No. 55-00534F, 1982.

Gordan, A.L.: Centaur D-1A Guidance Software System. Guidance and Control 1984, R.D. Culp and P.S. Stafford, eds., American Astronautical Society, 1984, pp. 311-326.



COMPLEX 41 SITE LAYOUT AZIMUTH



COMPLEX 41 SITE LAYOUT ELEVATION

FIGURE 1. - SITE LAYOUT AZIMUTH FOR COMPLEX 41, EASTERN TEST RANGE. (SINCE THE PLATFORM PORRO PRISM NORMAL IS OFFSET NOMINALLY  $32^{\circ}$  IN THE AZIMUTH PLANE FROM THE U-ACCELEROMETER INPUT AXIS, THE LINE-OF-SIGHT AZIMUTH MUST BE AS ILLUSTRATED HERE. WHEN THE PORRO PRISM IS ALIGNED USING THE AUTO THEODOLITE, THE CORRECT HEADING FOR THE U-ACCELEROMETER INPUT AXIS IS ESTABLISHED.) ALL DIMENSIONS ARE NOMINAL AND ARE PROVIDED FOR REFERENCE ONLY.

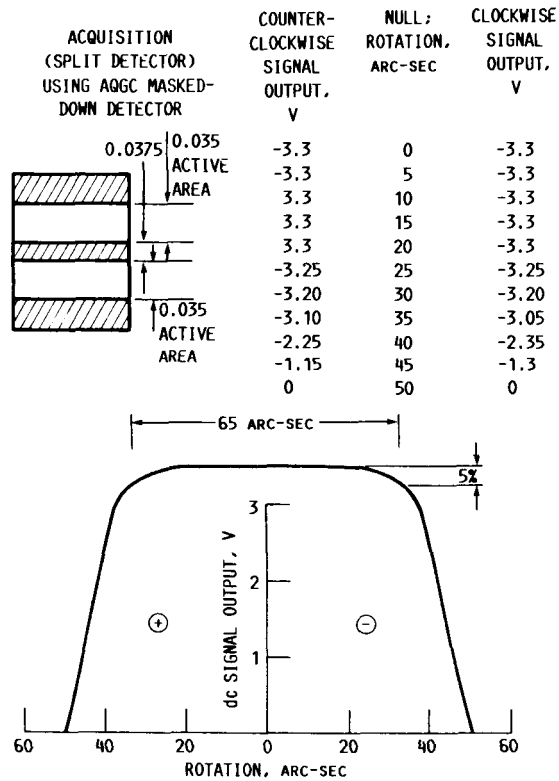


FIGURE 2. - ROTATION OF INERTIAL GUIDANCE PLATFORM; ACQUISITION CHANNEL MEASURED AT 10-FT ROTATION BY MASKED-DOWN, SPLIT ACQUISITION GAIN CONTROL (AQGC) ACQUISITION DETECTOR.

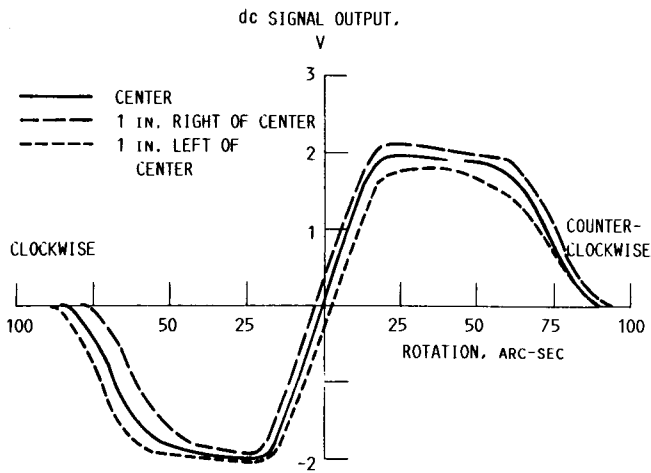


FIGURE 3. - ROTATION OF INERTIAL GUIDANCE PLATFORM; ERROR CHANNEL MEASURED 250 FT FROM PORRO PRISM.

— CENTER  
 - - - 1 IN. RIGHT OF CENTER  
 - · - 1 IN. LEFT OF CENTER

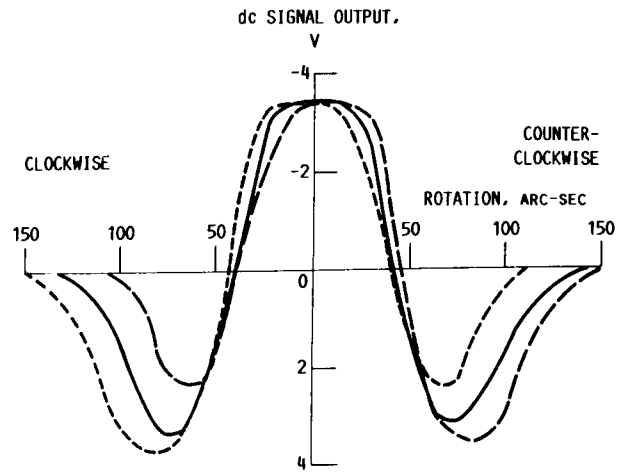


FIGURE 4. - ROTATION OF INERTIAL GUIDANCE PLATFORM; ACQUISITION CHANNEL MEASURED 250 FT FROM SPECIAL ACQUISITION GAIN CONTROL (AAGC) DETECTOR.

— CENTER  
 - - - 1 IN. RIGHT OF CENTER  
 - · - 1 IN. LEFT OF CENTER

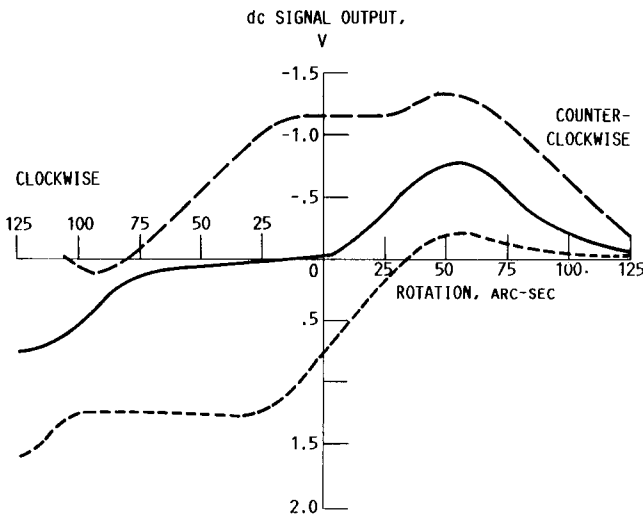


FIGURE 5. - ROTATION OF INERTIAL GUIDANCE PLATFORM; SWAY CHANNEL MEASURED 250 FT FROM PORRO PRISM. AT CENTER, SIGNAL IS ZERO AT 175 ARC-SEC; AT 1 IN. LEFT OF CENTER, SIGNAL IS ZERO AT 200 ARC-SEC.

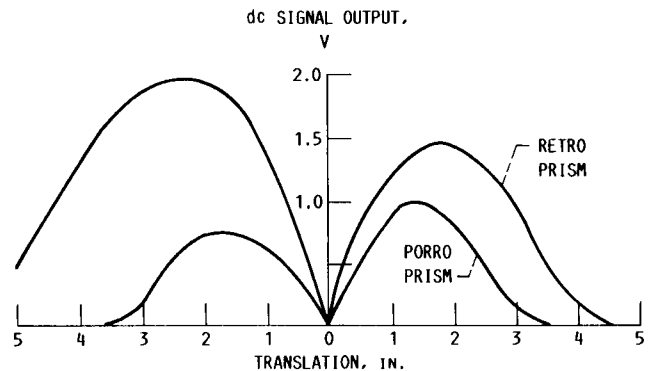


FIGURE 6. - TRANSLATION OF INERTIAL GUIDANCE PLATFORMS; SWAY CHANNEL MEASURED 250 FT FROM PORRO PRISM.

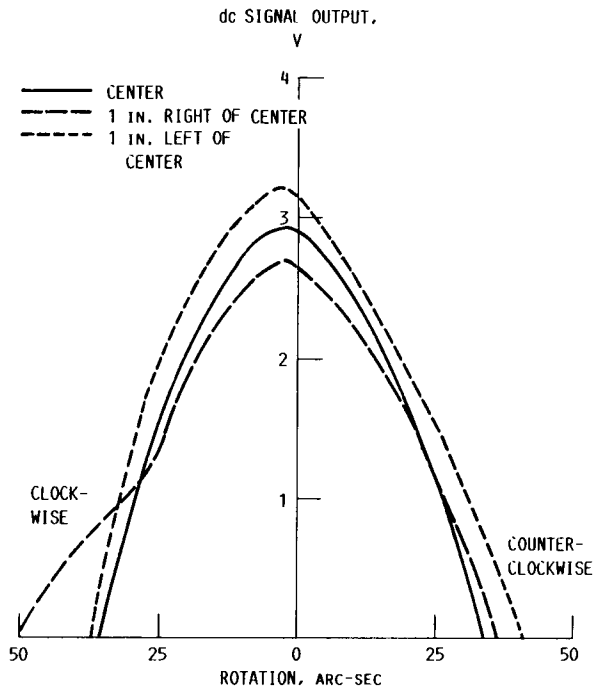


FIGURE 7. - ROTATION OF INERTIAL GUIDANCE PLATFORM; ACQUISITION GAIN CONTROL (AGGC) CHANNEL MEASURED BY NOMINAL AGGC DETECTOR 250 FT FROM PORRO PRISM.

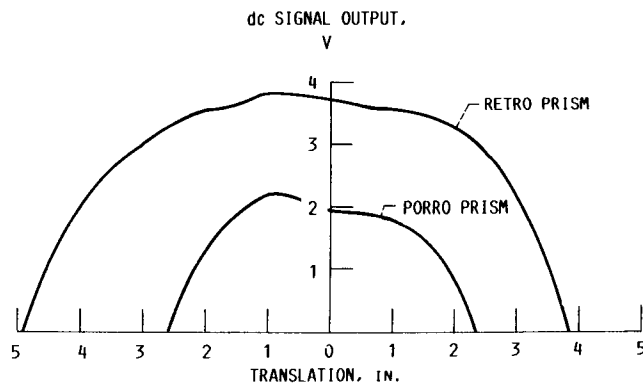


FIGURE 8. - TRANSLATION OF INERTIAL GUIDANCE PLATFORM; ACQUISITION GAIN CONTROL (AGGC) MEASURED 250 FT FROM PORRO PRISM BY AGGC DETECTOR WITH BIAS-SWITCHED PORRO PRISM.

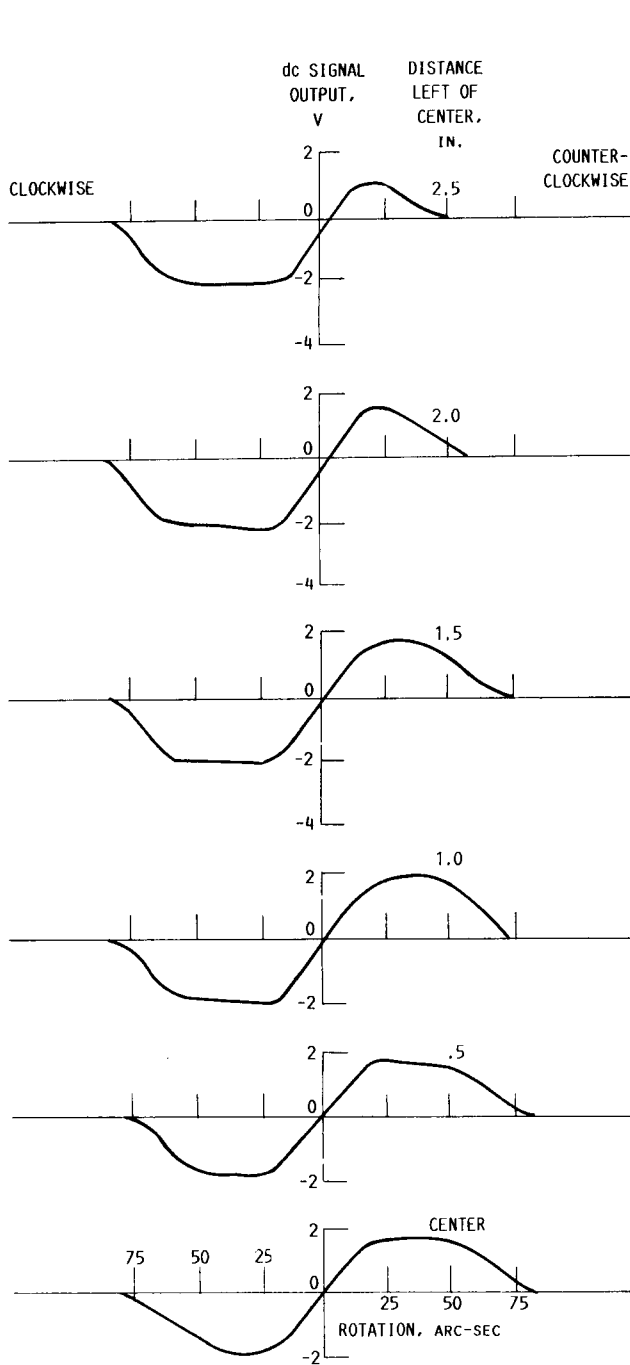


FIGURE 9. - ROTATION OF INERTIAL GUIDANCE PLATFORM, 345 FT FROM PORRO PRISM.

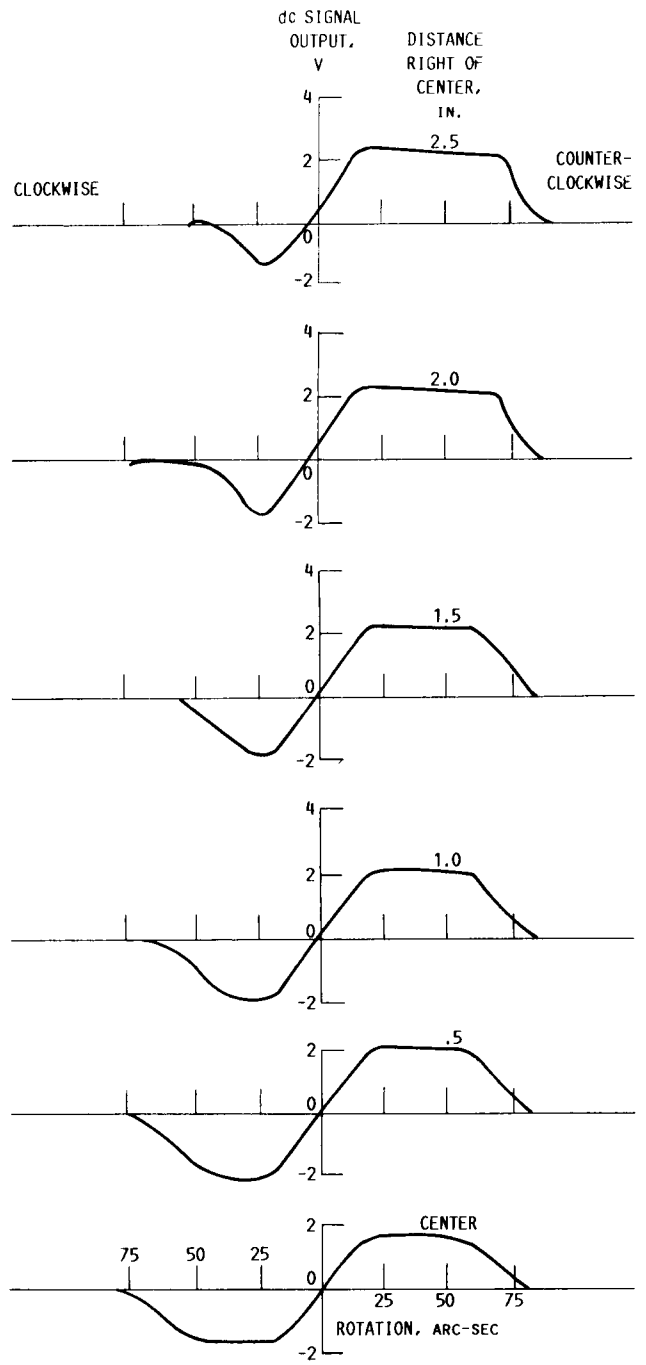


FIGURE 10. - ROTATION OF INERTIAL GUIDANCE PLATFORM ERROR CHANNEL MEASURED 345 FT FROM PORRO PRISM.

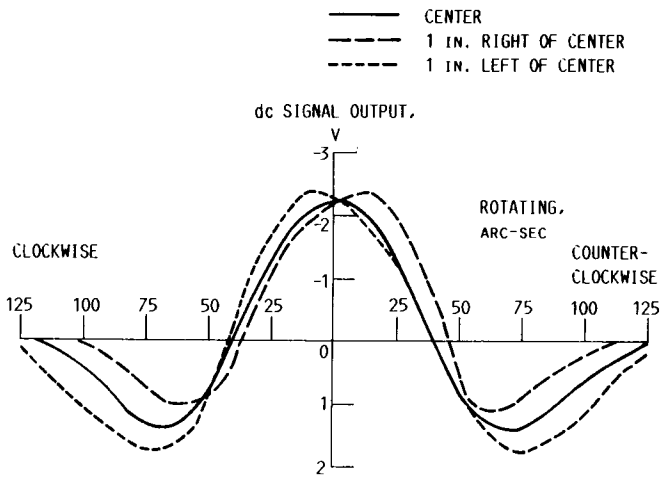


FIGURE 11. - ROTATION OF INERTIAL GUIDANCE PLATFORM; ACQUISITION CHANNEL MEASURED 345 FT FROM PORRO PRISM BY SPECIAL ACQUISITION GAIN CONTROL (AQGC) DETECTOR.

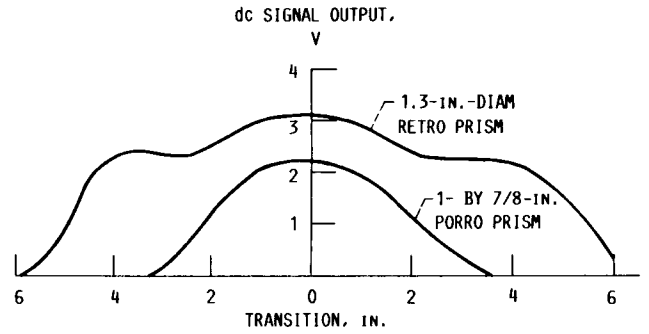


FIGURE 12. - TRANSITION OF INERTIAL GUIDANCE PLATFORM; ACQUISITION CHANNEL MEASURED 345 FT FROM PORRO PRISM BY SPECIAL ACQUISITION GAIN CONTROL (AQGC) DETECTOR. (NOTE: DEMODULATION OUT - SEE PAGE 79 OF APPENDIX D.)

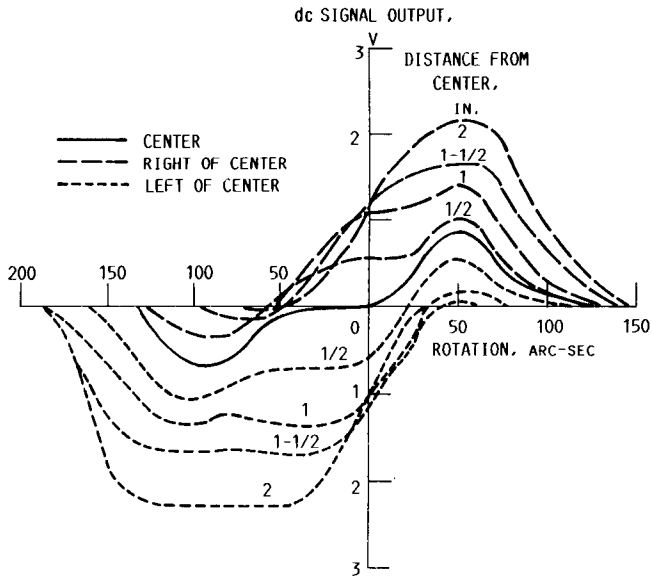


FIGURE 13. - ROTATION OF INERTIAL GUIDANCE PLATFORM; SWAY CHANNEL MEASURED 345 FT FROM PORRO PRISM.

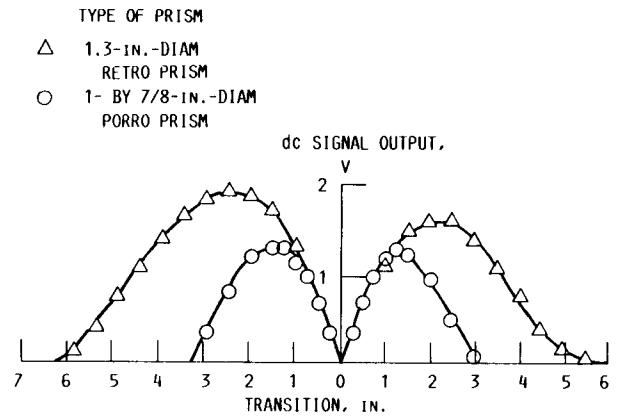


FIGURE 14. - TRANSLATION OF INERTIAL GUIDANCE PLATFORM; SWAY CHANNEL MEASURED 345 FT FROM PORRO PRISM. (NOTE: DEMODULATION OUT.)

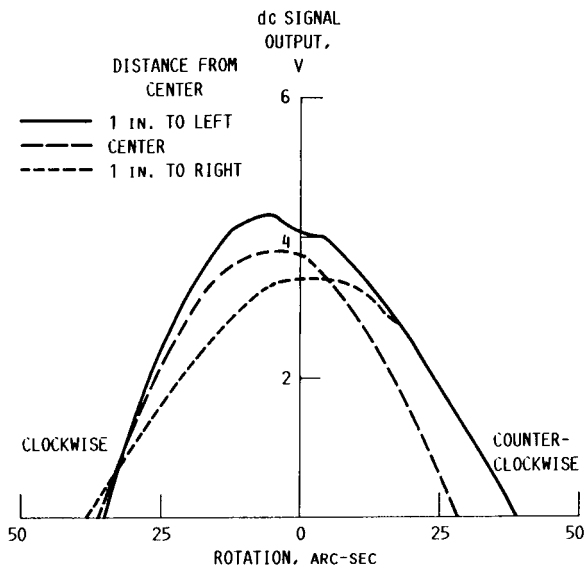


FIGURE 15. - ROTATION OF INERTIAL GUIDANCE PLATFORM; ACQUISITION GAIN CONTROL (AGGC) CHANNEL MEASURED 345 FT FROM PORRO PRISM BY NOMINAL AGGC DETECTOR.

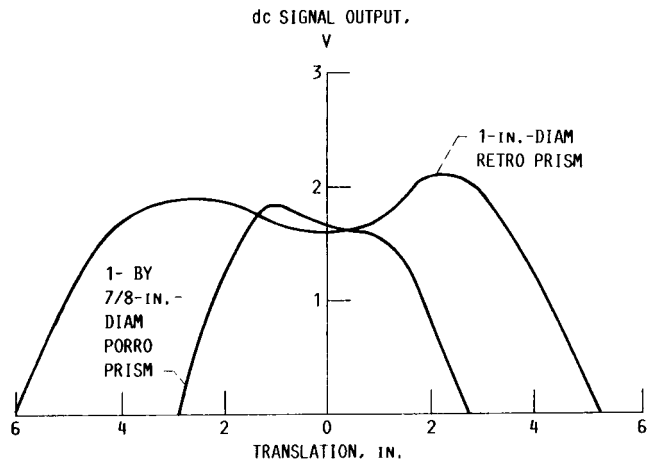


FIGURE 16. - TRANSLATION OF INERTIAL GUIDANCE PLATFORM; ACQUISITION GAIN CONTROL (AGGC) CHANNEL MEASURED 345 FT FROM PORRO PRISM (dc AMPLIFIER OUTPUT).

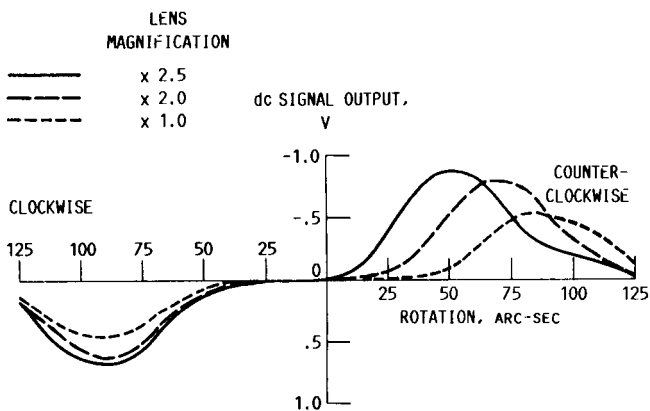


FIGURE 17. - ROTATION OF INERTIAL GUIDANCE PLATFORM; SWAY CHANNEL MEASURED 345 FT FROM PORRO PRISM WITH VARIOUS LENS CONFIGURATIONS (PENTA MIRROR AT CENTER POSITION).

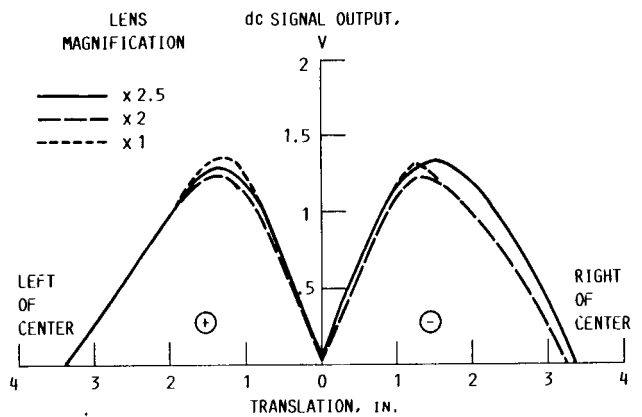


FIGURE 18. - TRANSLATION OF INERTIAL GUIDANCE PLATFORM; SWAY CHANNEL MEASURED 345 FT FROM PORRO PRISM WITH VARIOUS RELAY LENS CONFIGURATIONS.

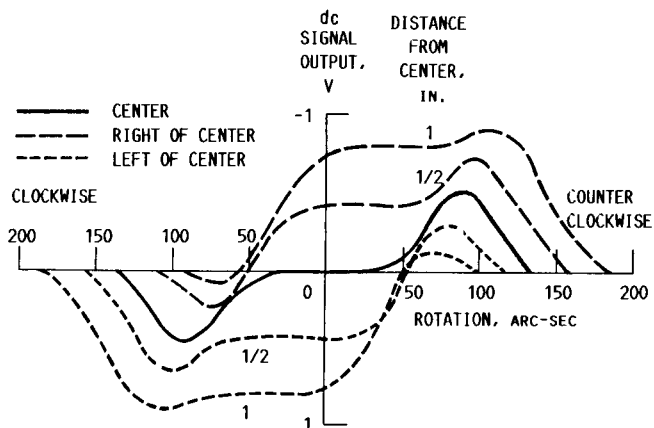


FIGURE 19. - ROTATION OF INERTIAL GUIDANCE PLATFORM; SWAY CHANNEL MEASURED 345 FT FROM PORRO PRISM RELOCATED TO GIVE A 1:1 IMAGE.

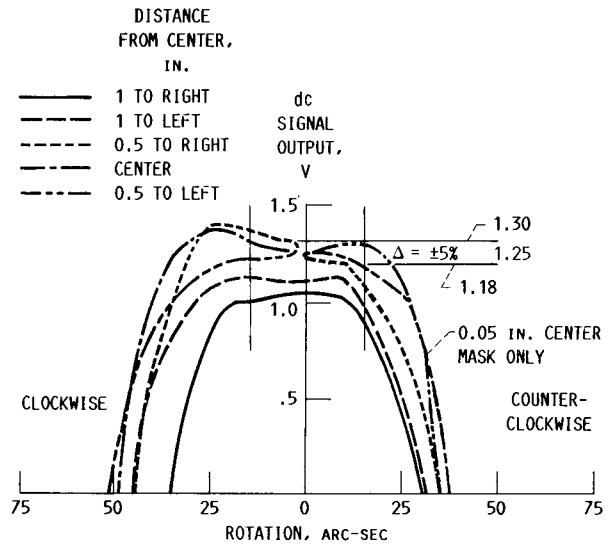


FIGURE 20. - ROTATION OF INERTIAL GUIDANCE PLATFORM, ACQUISITION GAIN CONTROL (AGGC) CHANNEL ( $\times 2.5$ ); AGGC DETECTOR IN ACQUIRE POSITION WITH MAXIMUM PORRO PRISM OUTPUT.

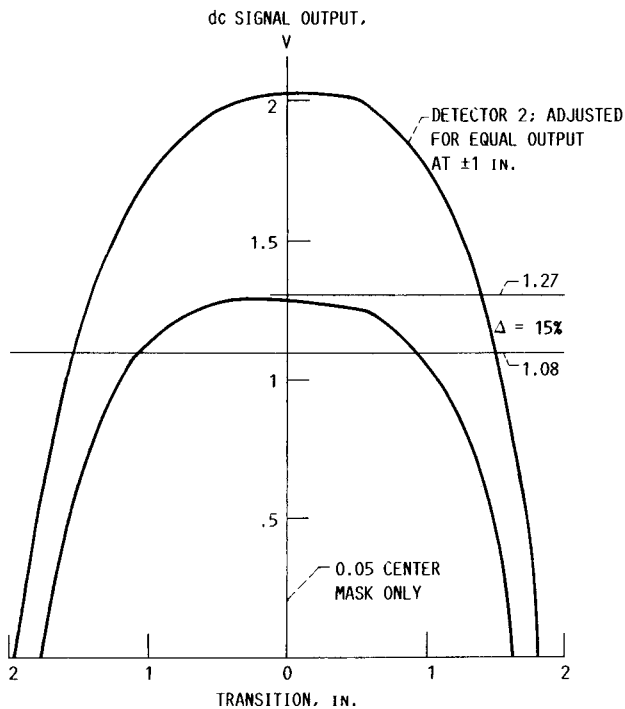


FIGURE 21. - TRANSLATION OF INERTIAL GUIDANCE PLATFORM, ACQUISITION GAIN CONTROL (AGGC) CHANNEL ( $\times 2.5$ ); AGGC DETECTOR IN ACQUIRE POSITION WITH MAXIMUM PORRO PRISM OUTPUT.

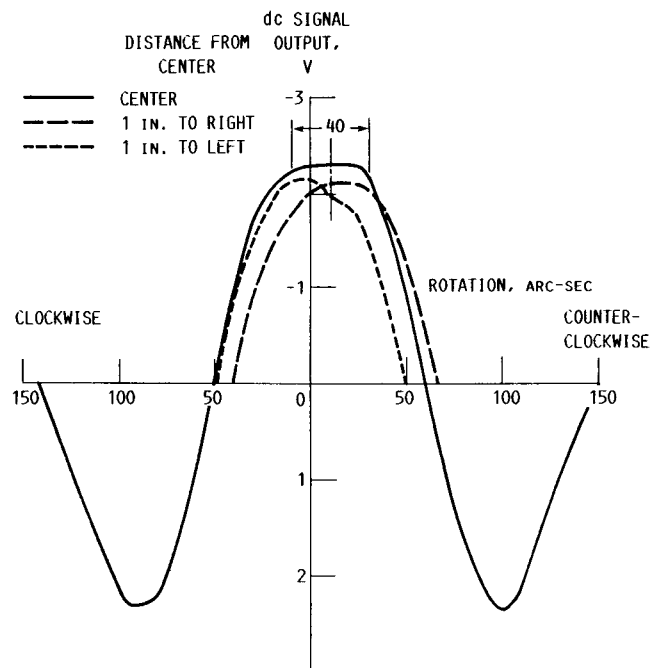


FIGURE 22. - ROTATION OF INERTIAL GUIDANCE PLATFORM; ACQUISITION CHANNEL MEASURED BY ACQUISITION GAIN CONTROL (AGGC) DETECTOR WITH 0.05-IN. MASK IN CENTER.

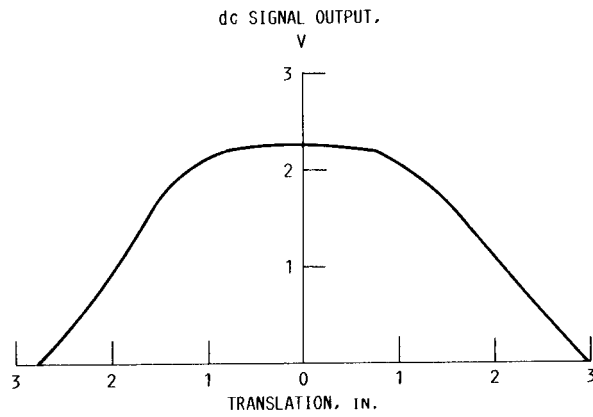


FIGURE 23. - TRANSLATION OF INERTIAL GUIDANCE PLATFORM: ACQUISITION CHANNEL MEASURED BY ACQUISITION GAIN CONTROL DETECTOR WITH 0.05 IN. CENTER MASK.

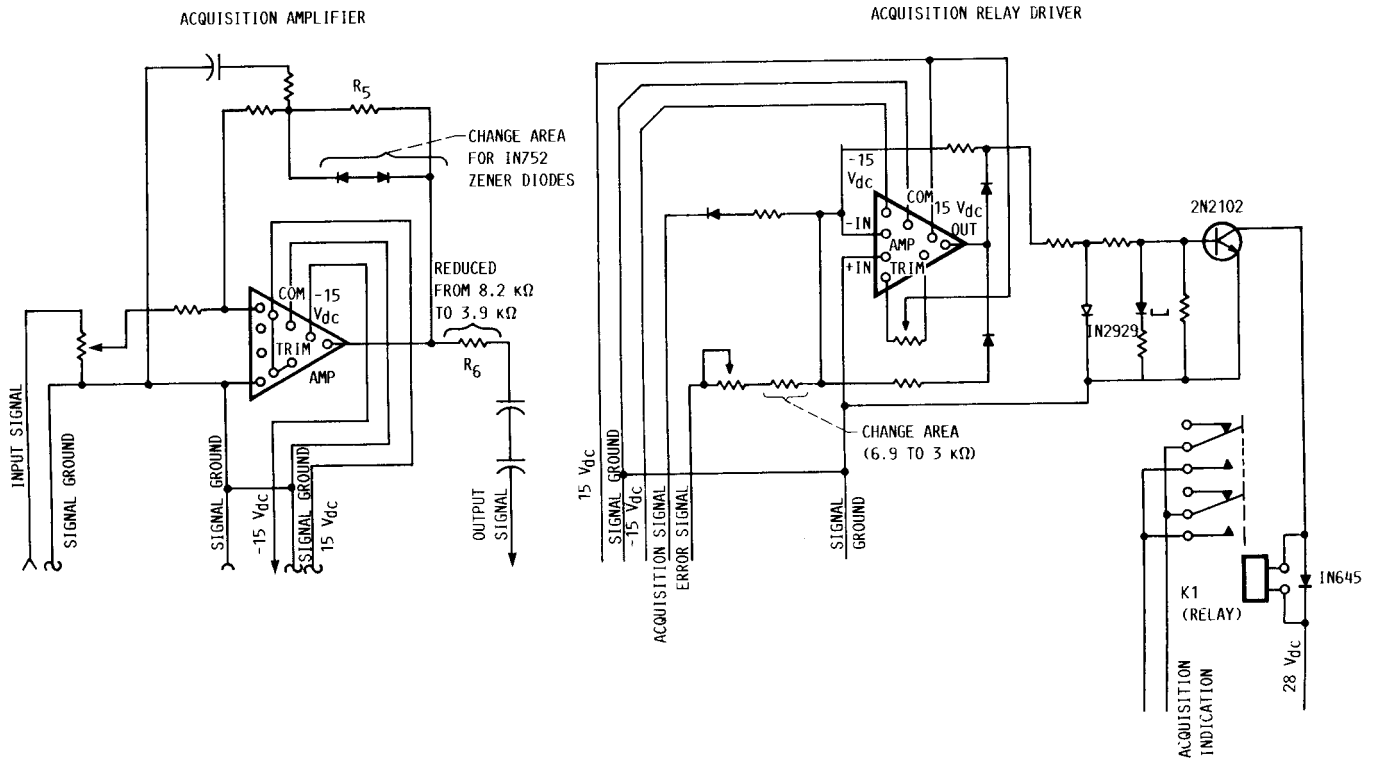


FIGURE 24. - SCHEMATIC OF ACQUISITION AMPLIFIER AND ACQUISITION RELAY DRIVER.

ORIGINAL PAGE IS  
OF POOR QUALITY.

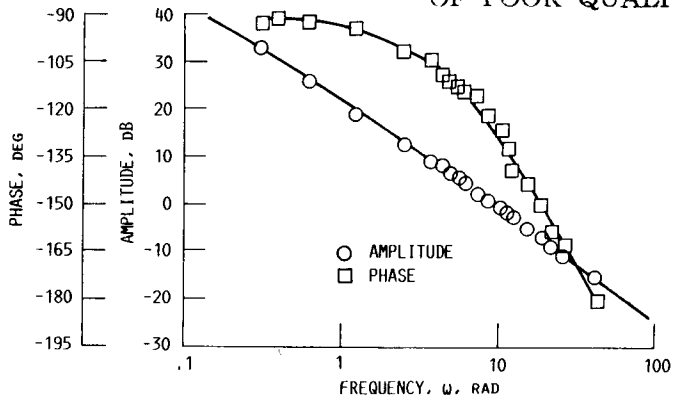


FIGURE 25. - AMPLITUDE AS FUNCTION OF FREQUENCY FOR PENTA OPEN LOOP (AVERAGE OF TWO RUNS).

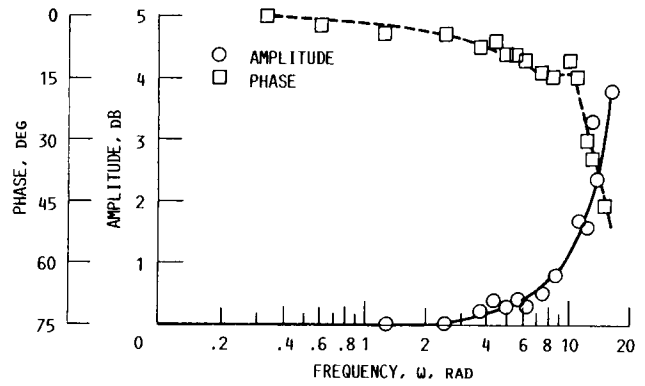
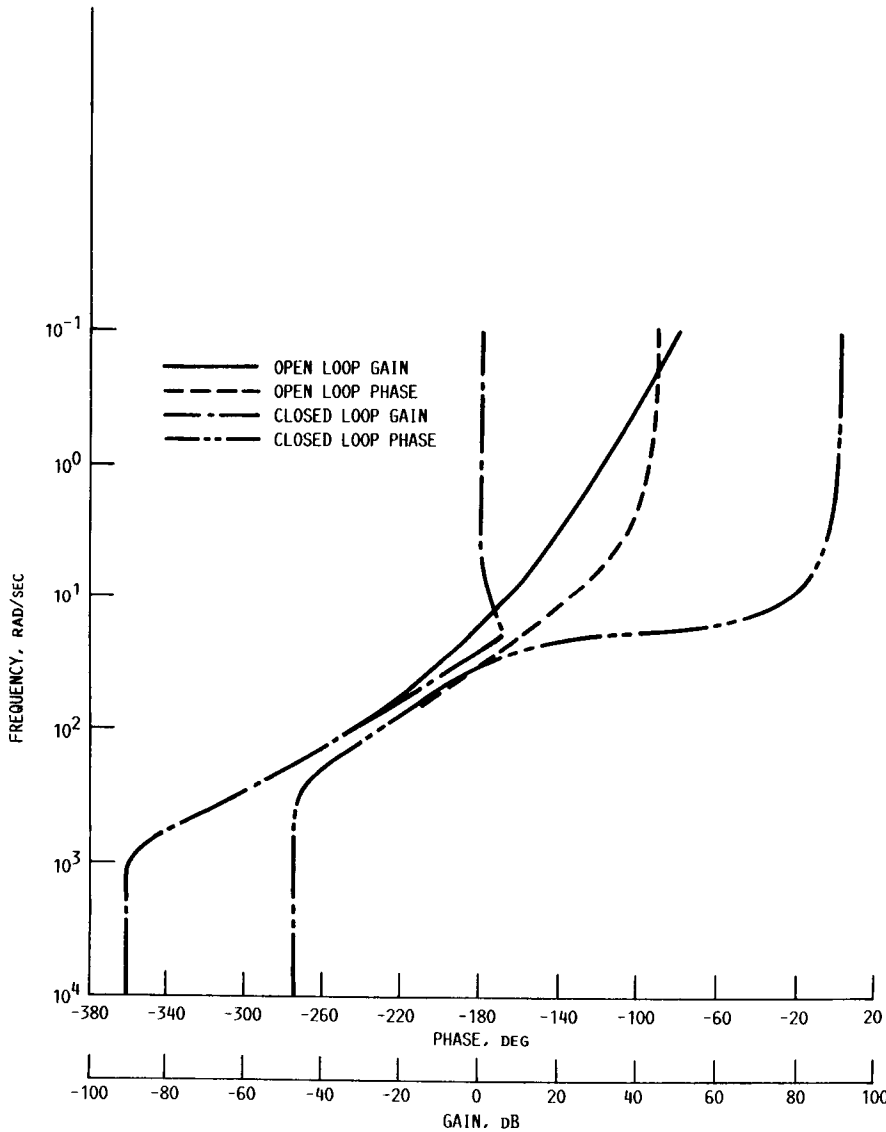


FIGURE 26. - FREQUENCY AS FUNCTION OF AMPLITUDE FOR PENTA CLOSED-LOOP WITH 2-1/2-IN. DISPLACEMENT.



FREQUENCY, RAD/SEC	OPEN LOOP GAIN, dB	OPEN LOOP PHASE, DEG	CLOSED LOOP GAIN, dB	CLOSED LOOP PHASE, DEG
.100	49.2	-90.5	0.0	-2
.126	47.2	-90.7	0.0	-2
.158	45.2	-90.9	0.0	-3
.200	43.2	-91.1	0.0	-4
.251	41.2	-91.4	0.0	-5
.316	39.2	-91.7	0.0	-6
.398	37.2	-92.2	0.0	-8
.501	35.2	-92.7	0.0	-1.0
.631	33.2	-93.4	0.0	-1.2
.794	31.2	-94.3	0.0	-1.6
1.00	29.2	-95.4	0.0	-2.0
1.26	27.2	-96.8	0.0	-2.5
1.58	25.2	-98.6	.1	-3.1
2.00	23.1	-100.8	.1	-4.0
2.51	21.1	-103.5	.1	-5.0
3.16	19.0	-106.9	.2	-6.4
3.98	16.8	-111.0	.4	-8.1
5.01	14.5	-116.1	.6	-10.4
6.31	12.2	-122.0	1.0	-13.5
7.94	9.7	-128.9	1.6	-17.9
10.0	6.9	-136.6	2.6	-24.7
12.6	4.0	-145.0	4.4	-37.0
15.8	0.8	-153.7	7.1	-66.1
20.0	-2.7	-162.6	6.0	-126.2
25.1	-6.3	-171.6	-8	-163.8
31.6	-10.2	-180.6	-6.9	-180.9
39.8	-14.2	-189.8	-12.4	-192.2
50.1	-18.5	-199.4	-17.4	-201.9
63.1	-22.9	-209.3	-22.4	-211.5
79.4	-27.6	-219.7	-27.4	-221.3
100	-32.7	-230.3	-32.6	-231.4
126	-38.1	-240.9	-38.0	-241.5
158	-43.8	-250.8	-43.8	-251.1
200	-49.9	-259.6	-49.9	-259.7
251	-56.2	-266.7	-56.2	-266.8
316	-62.7	-272.0	-62.7	-272.0
398	-69.3	-275.3	-69.3	-275.4
501	-75.9	-277.0	-75.9	-277.0
631	-82.4	-277.5	-82.4	-277.5
794	-88.8	-277.1	-88.8	-277.1
1000	-95.1	-276.3	-95.1	-276.3
1260	-101.3	-275.4	-101.3	-275.4
1580	-107.4	-274.5	-107.4	-274.5
2000	-113.5	-273.7	-113.5	-273.7
2500	-119.6	-273.0	-119.6	-273.0
3160	-125.6	-272.4	-125.6	-272.4
3980	-131.6	-271.9	-131.6	-271.9
5010	-137.6	-271.5	-137.6	-271.5
6310	-143.7	-271.2	-143.7	-271.2
7940	-149.7	-271.0	-149.7	-271.0

FIGURE 27. - BODE PLOT; CONTINUOUS SYSTEM MODELING PROGRAM III (TSS/360). EQUIVALENT NOISE BANDWIDTH, 67.021 RAD/SEC. (DATA FROM PERKIN-ELMER.)

C-2

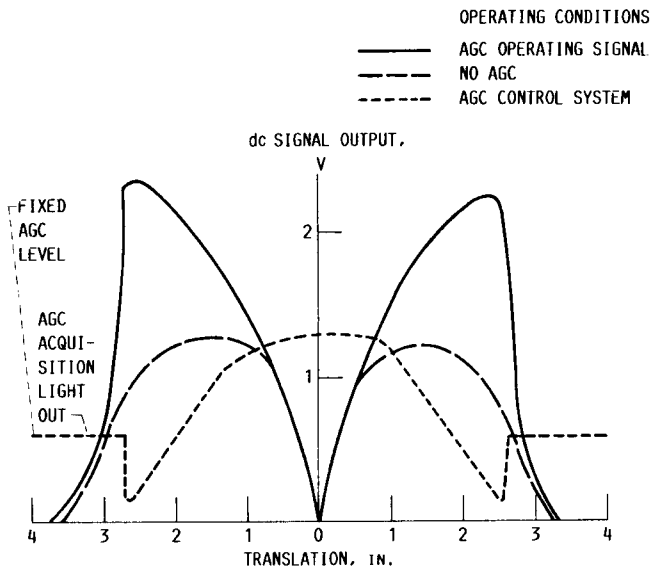


FIGURE 28. - TRANSLATION OF INERTIAL GUIDANCE PLATFORM; SWAY CHANNEL MEASURED 345 FT FROM PORRO PRISM; AUTOMATIC GAIN CONTROL (AGC) OPERATIONAL.

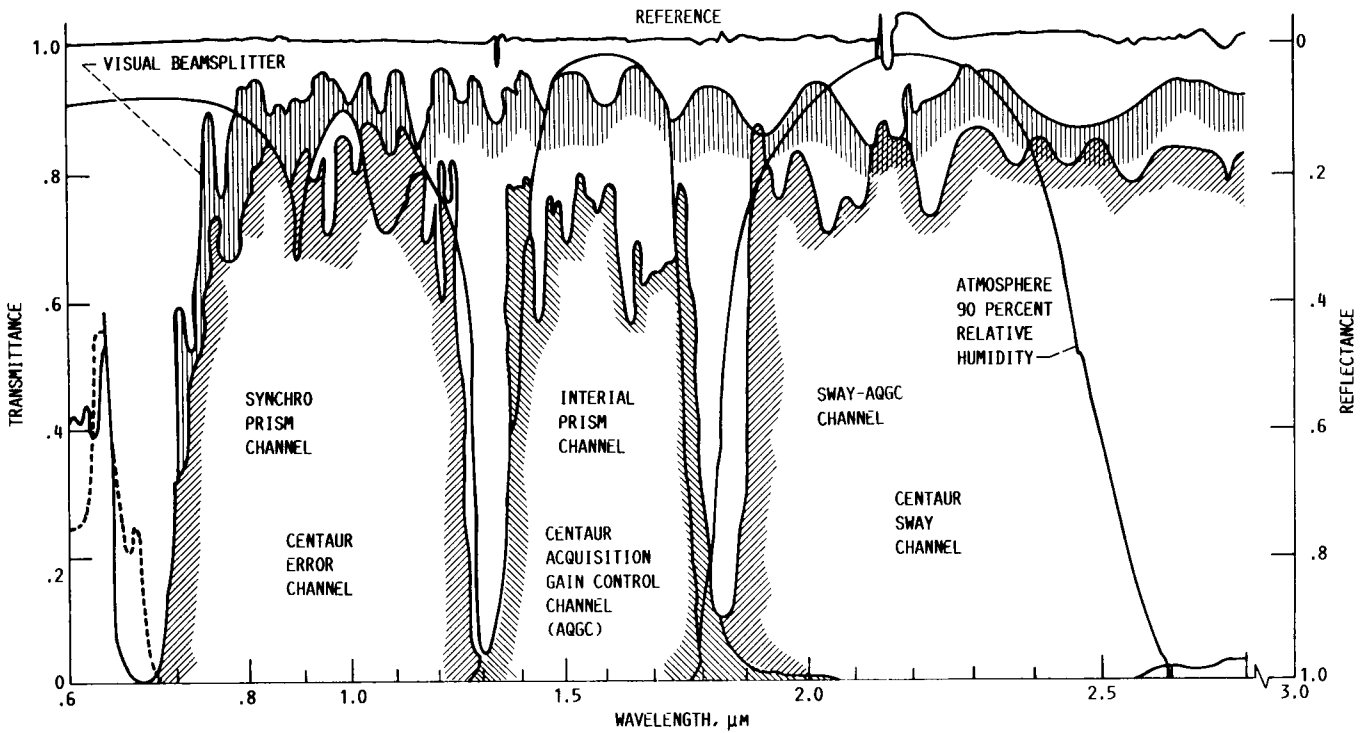


FIGURE 29. - AUTOCOLLIMATOR SPECTRAL SEPARATION CHART.

ORIGINAL PAGE IS  
OF POOR QUALITY

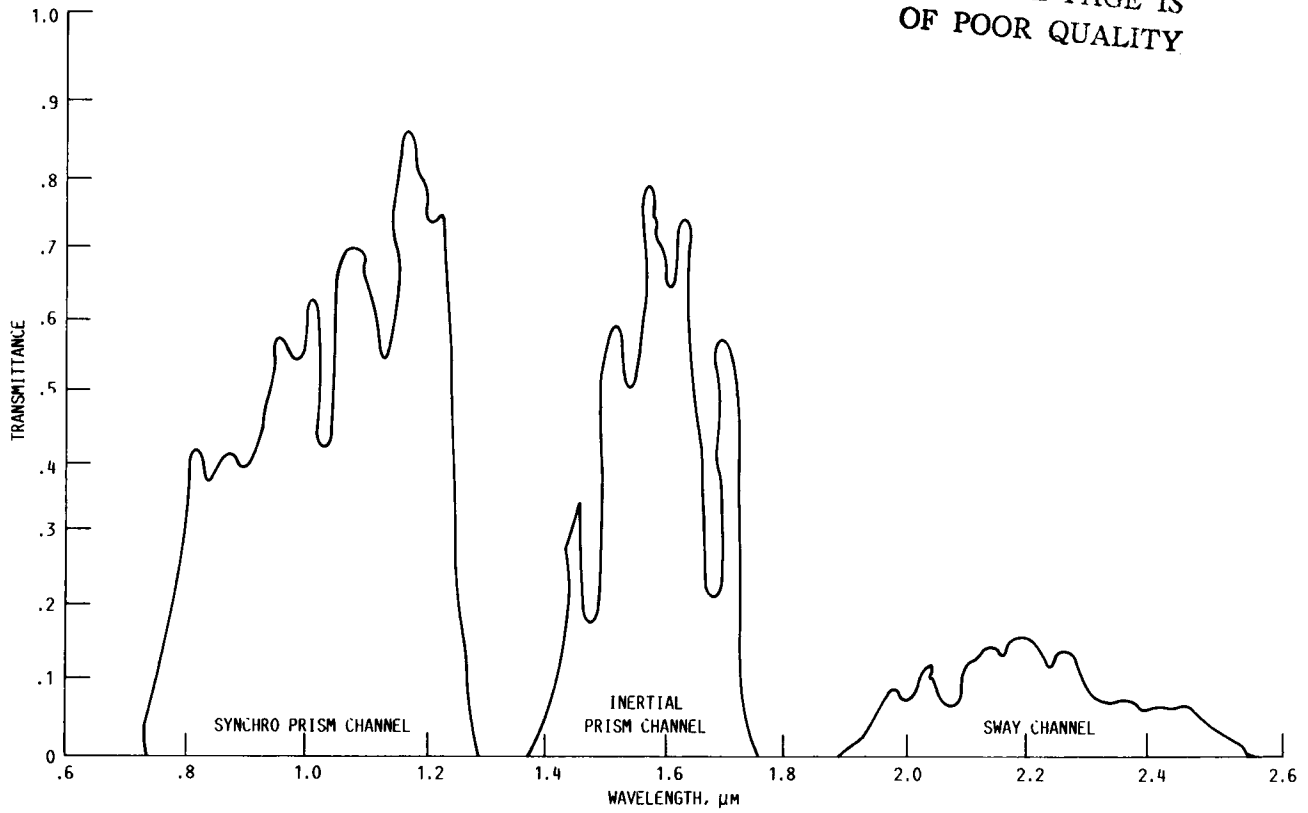


FIGURE 30. - SYNCHRO, INERTIAL, AND SWAY CHANNEL TRANSMITTANCE AT 450 FT OPERATING DISTANCE; 2400 K LAMP COLOR TEMPERATURE.

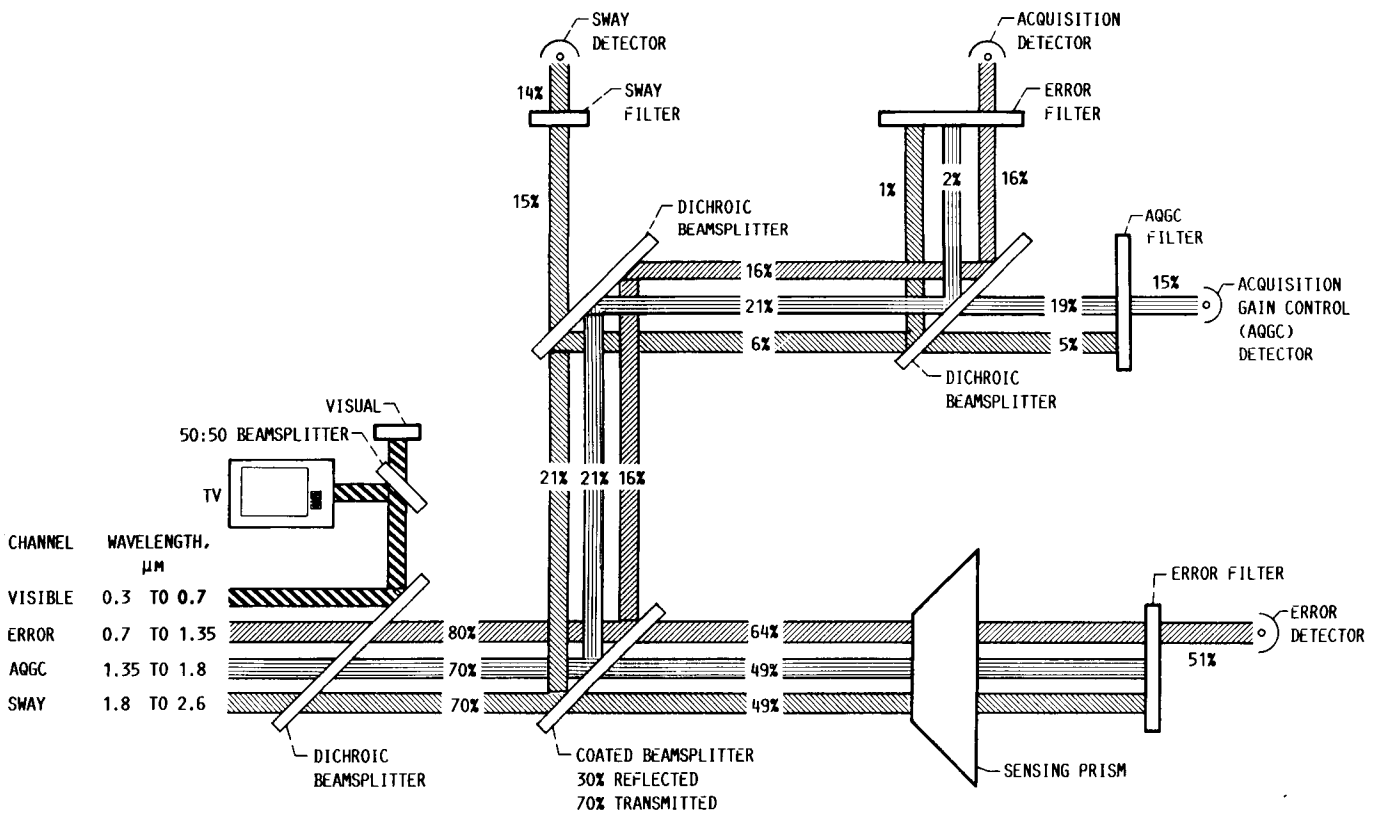


FIGURE 31. - CENTAUR AUTOCOLLIMATOR SPECTRAL SEPARATION SCHEMATIC.

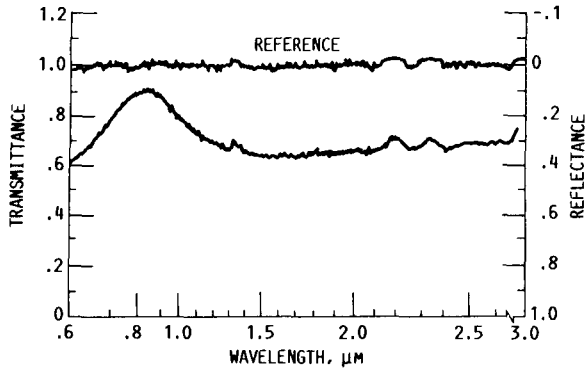


FIGURE 32. - DICHOIC BEAMSPLITTER.

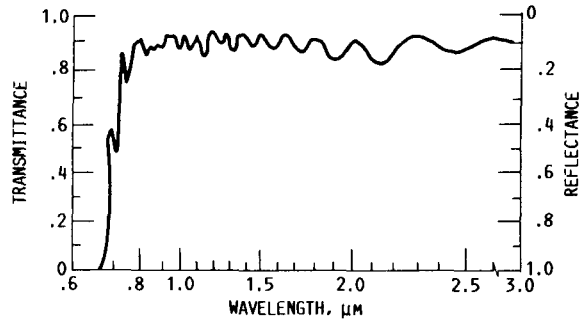


FIGURE 33. - VISUAL BEAMSPLITTER; 90° INCIDENT ANGLE.

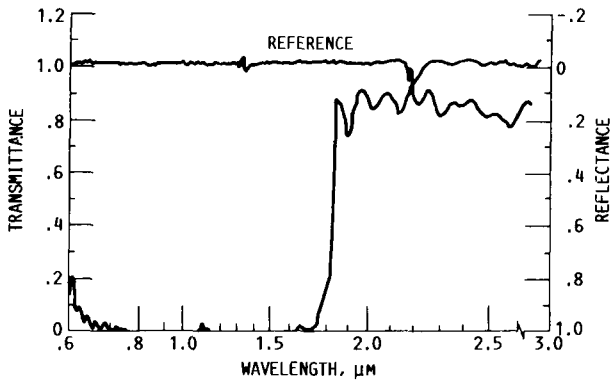


FIGURE 34. - SWAY CHANNEL FILTER; 90° INCIDENT ANGLE.

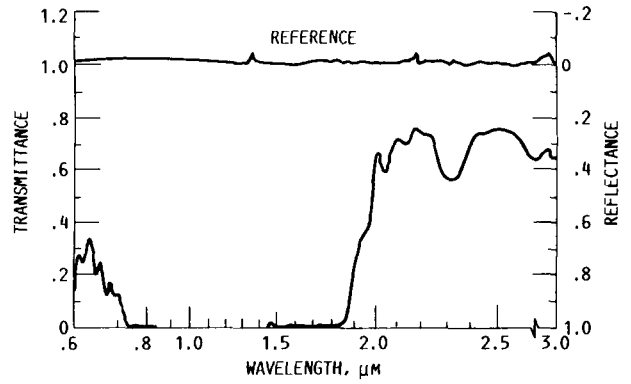


FIGURE 35. - SWAY CHANNEL BEAMSPLITTER; 45° INCIDENT ANGLE.

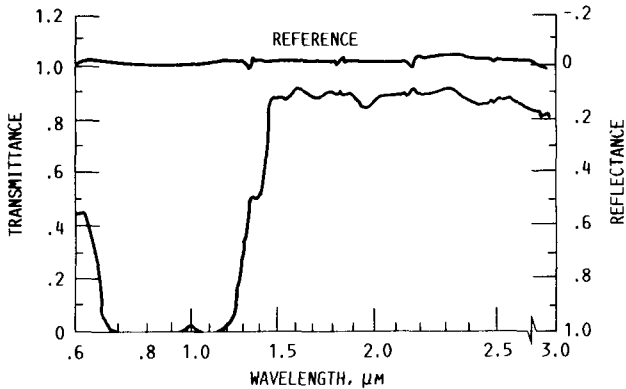


FIGURE 36. - ACQUISITION BEAMSPLITTER, 45° INCIDENT ANGLE.

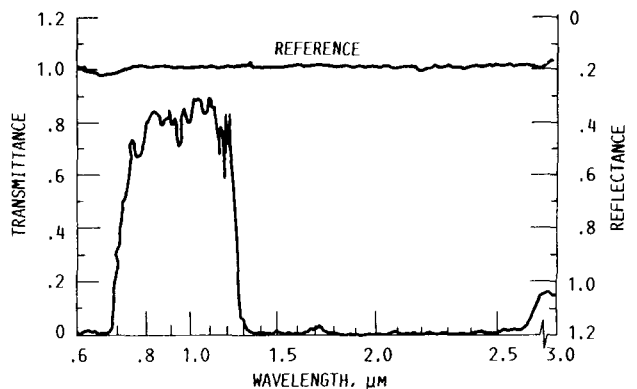


FIGURE 37. - ERROR FILTER; 90° INCIDENT ANGLE.

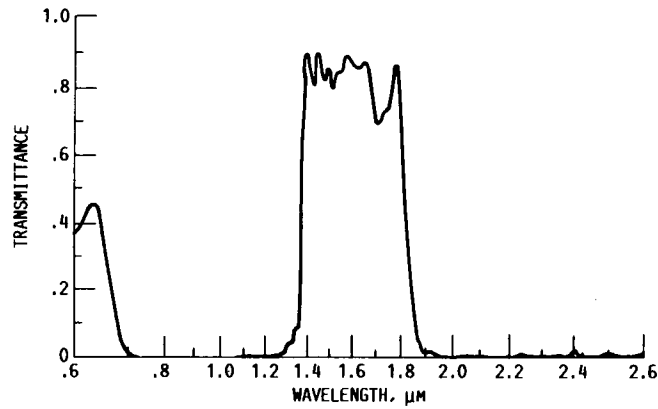


FIGURE 38. - ACQUISITION GAIN CONTROL (AGC) CHANNEL FILTER.

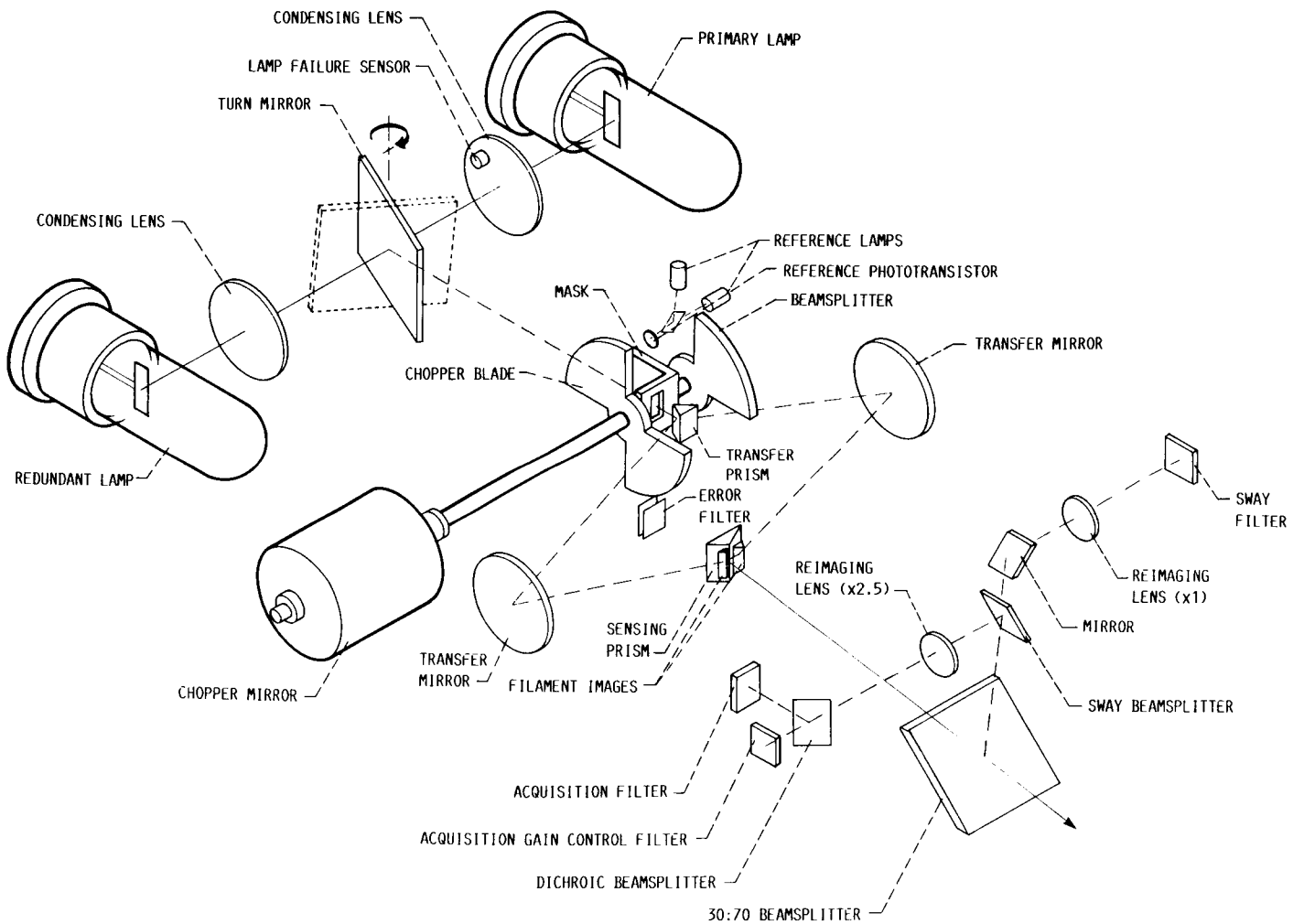


FIGURE 39. - CENTAUR SOURCE AND DETECTOR ASSEMBLY - SIMPLIFIED OPTICAL SCHEMATIC.

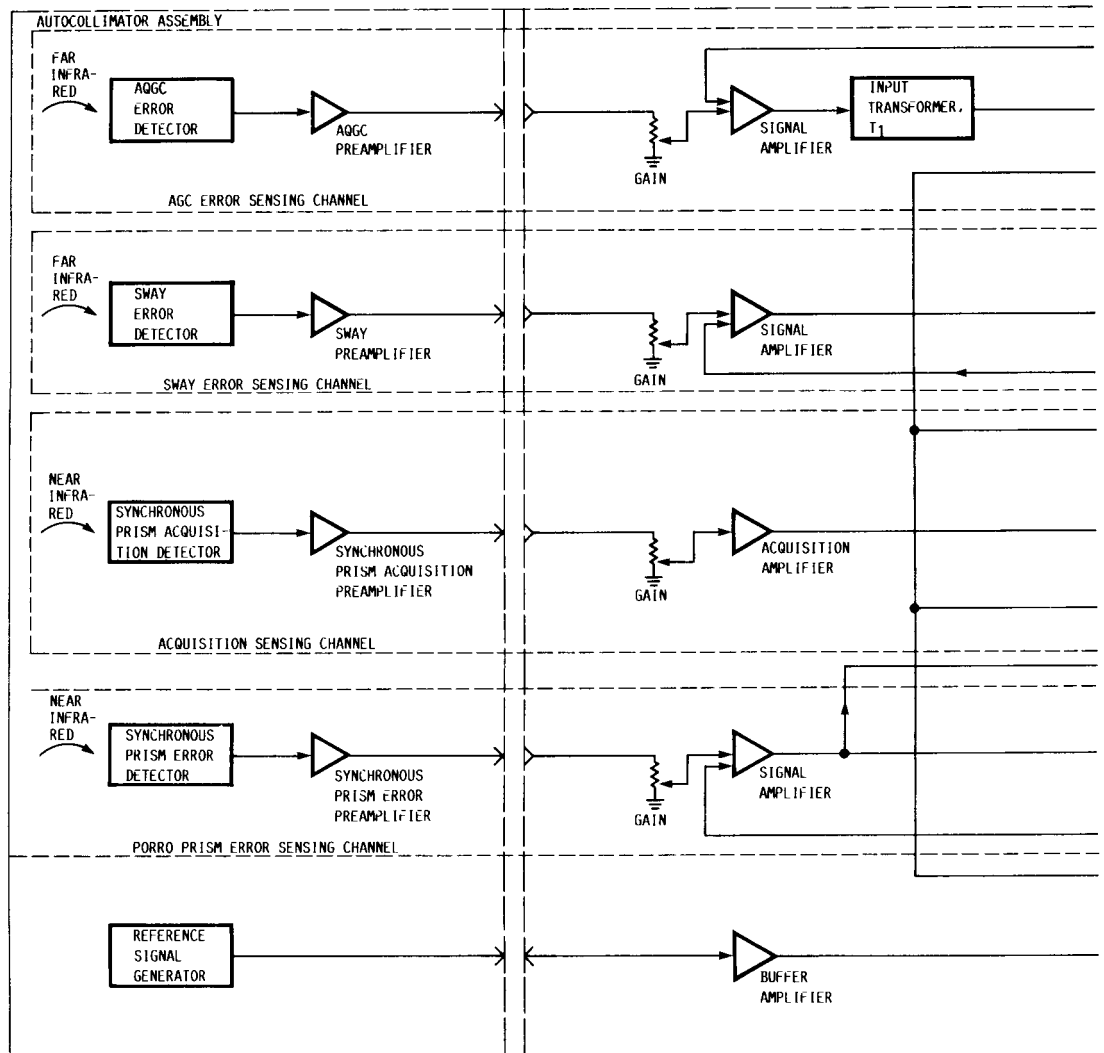


FIGURE 40. - CENTAUR AUTOHEODOLITE ELECTRONIC BLOCK DIAGRAM.

ORIGINAL PAGE IS  
OF POOR QUALITY

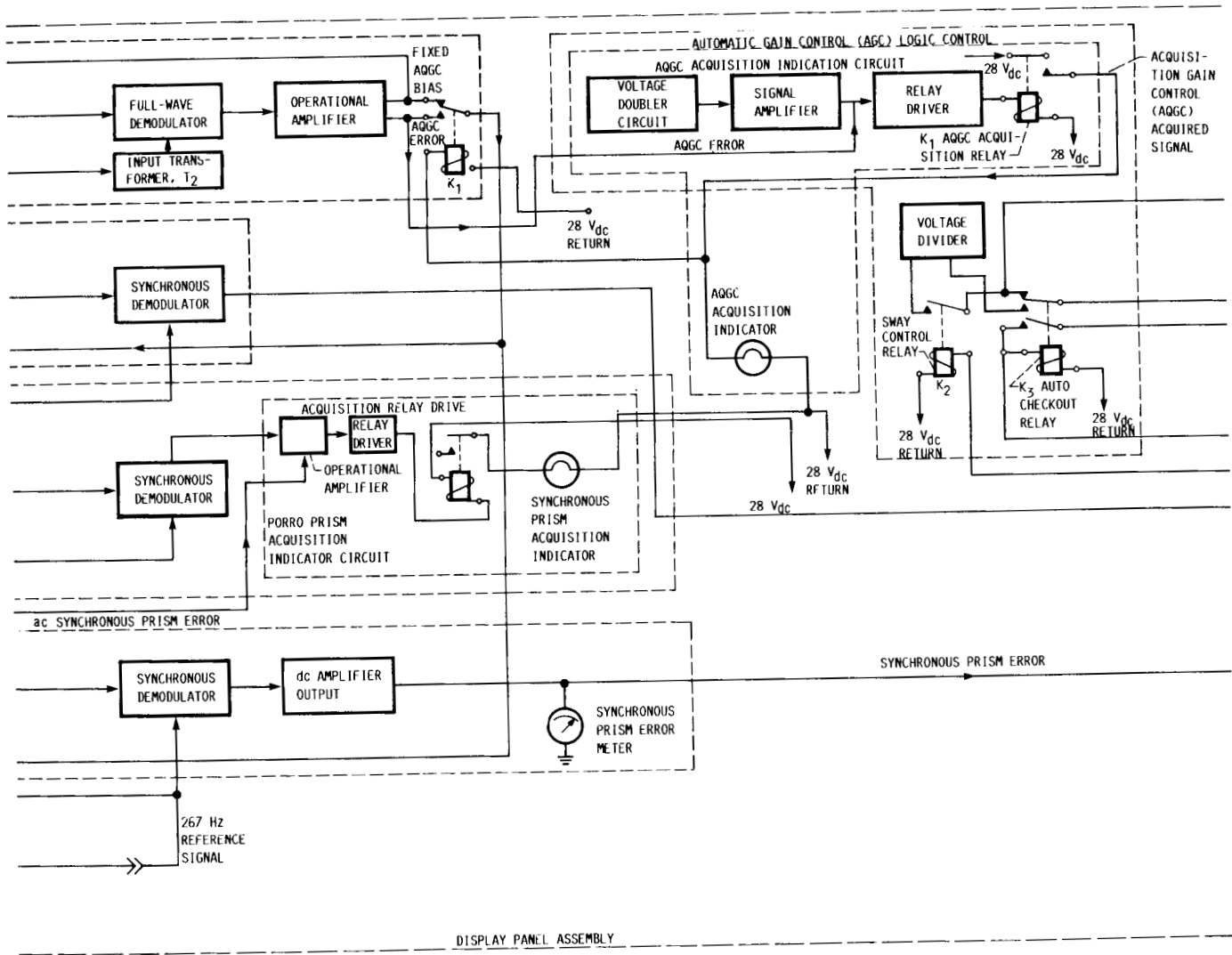


FIGURE 40. - CONTINUED.

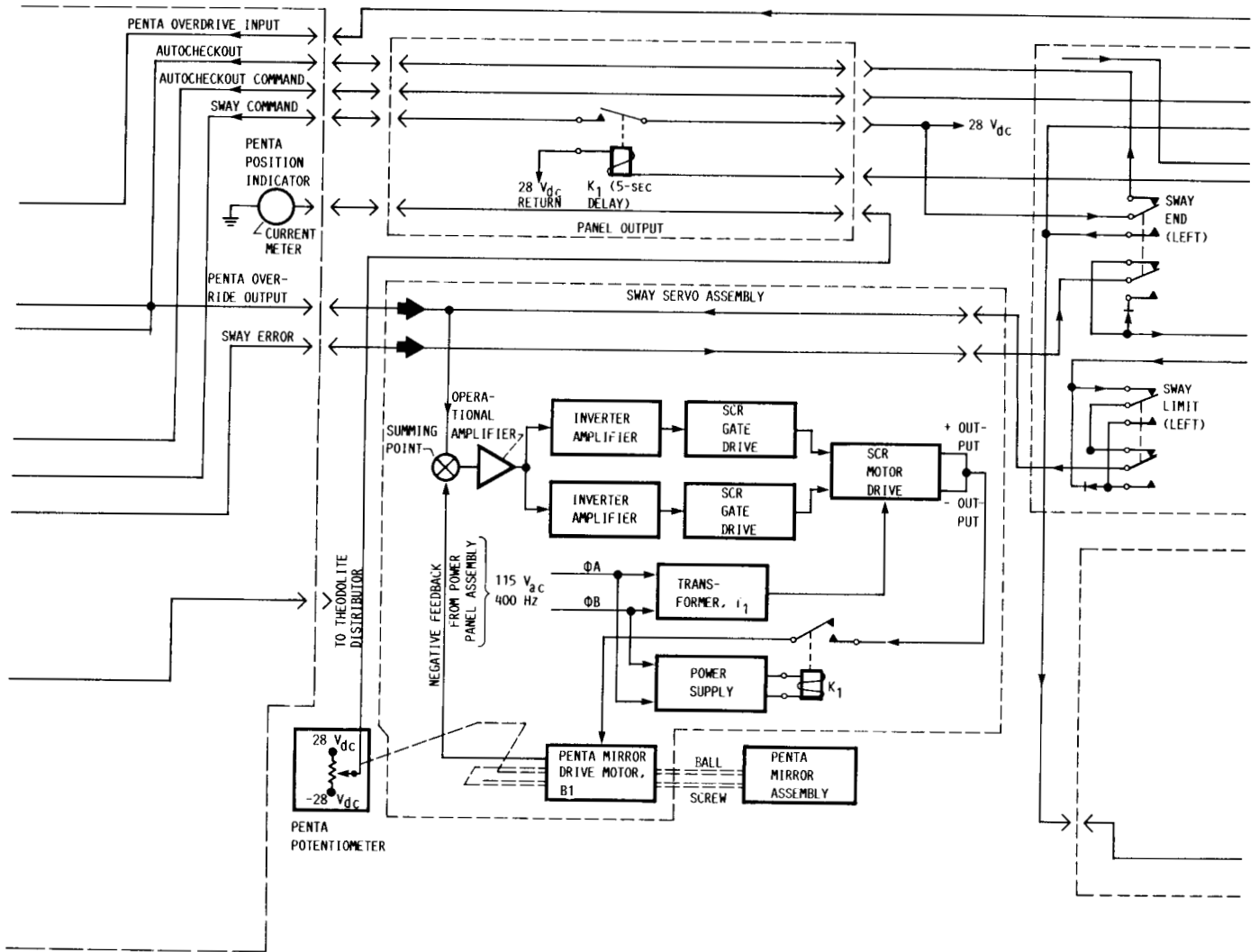


FIGURE 40. - CONTINUED.

ORIGINAL PAGE IS  
OF POOR QUALITY

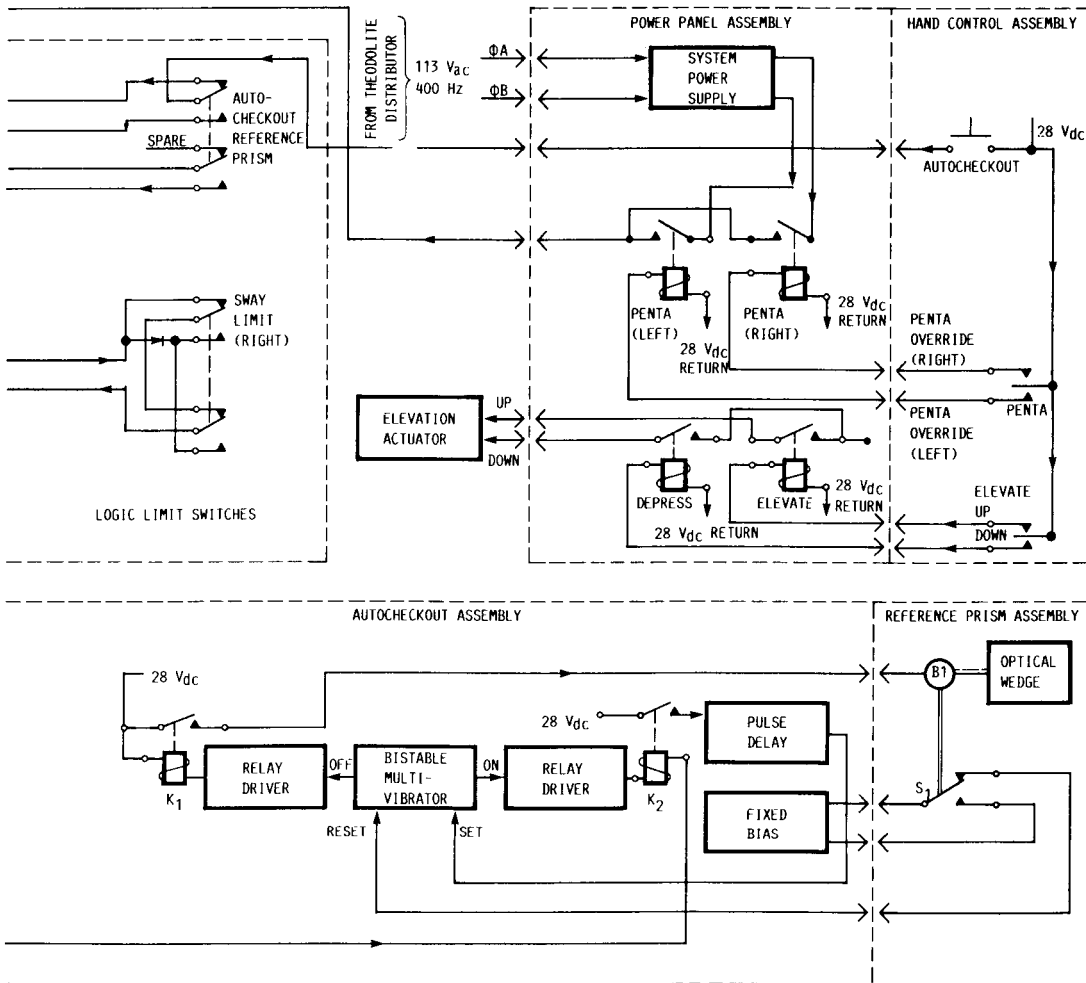


FIGURE 40. - CONCLUDED.



National Aeronautics and  
Space Administration

## Report Documentation Page

1. Report No. <b>NASA TM-88844</b>		2. Government Accession No.		3. Recipient's Catalog No.	
4. Title and Subtitle <b>Optical Alignment of Centaur's Inertial Guidance System</b>				5. Report Date <b>December 1987</b>	
				6. Performing Organization Code	
7. Author(s) <b>Andrew L. Gordan</b>				8. Performing Organization Report No. <b>E-3226</b>	
				10. Work Unit No. <b>917-60-00</b>	
9. Performing Organization Name and Address <b>National Aeronautics and Space Administration Lewis Research Center Cleveland, Ohio 44135-3191</b>				11. Contract or Grant No.	
				13. Type of Report and Period Covered <b>Technical Memorandum</b>	
12. Sponsoring Agency Name and Address <b>National Aeronautics and Space Administration Washington, D.C. 20546-0001</b>				14. Sponsoring Agency Code	
15. Supplementary Notes					
16. Abstract During Centaur launch operations the launch azimuth of the inertial platform's U-accelerometer input axis must be accurately established and maintained. This is accomplished by using an optically closed loop system with a long-range auto-theodolite whose line of sight has been established by a first-order survey. A collimated light beam from the autotheodolite intercepts a reflecting Porro prism mounted on the platform azimuth gimbal. Thus, any deviation of the Porro prism from its predetermined heading is optically detected by the autotheodolite. The error signal produced is used to torque the azimuth gimbal back to its required launch azimuth. The heading of the U-accelerometer input axis is therefore maintained automatically. Previously, the autotheodolite system could not distinguish between vehicle sway (translatory motion) and rotational motion of the inertial platform unless at least three prisms were used. One prism was mounted on the inertial platform to maintain azimuth alignment, and two prisms were mounted externally on the vehicle to track sway. For example, the automatic azimuth-laying theodolite (AALT-SV-M2) on the Saturn vehicle used three prisms. This report documents and describes the results of testing and modifying the AALT-SV-M2 autotheodolite to simultaneously monitor and maintain alignment of the inertial platform and track the sway of the vehicle from a single Porro prism.					
17. Key Words (Suggested by Author(s)) <b>Optical theodolite systems</b>			18. Distribution Statement <b>Unclassified - Unlimited Subject Category 14</b>		
19. Security Classif. (of this report) <b>Unclassified</b>		20. Security Classif. (of this page) <b>Unclassified</b>		21. No of pages <b>106</b>	22. Price* <b>A06</b>